Cardiac L-type calcium channels and expression of RGK proteins in mouse models associated with type 2 diabetes

Dissertation
zur
Erlangung des Doktorgrades (Dr. rer. nat.)
der
Mathematisch-Naturwissenschaftlichen Fakultät
der
Rheinischen Friedrich-Wilhelms-Universität Bonn

vorgelegt von
Jessica Köth
aus
Hachenburg

Bonn, 02.03.2017

Angefertigt mit Genehmigung der
Mathematisch-Naturwissenschaftlichen Fakultät
der Rheinischen Friedrich-Wilhelms-Universität Bonn

1. Gutachter: Priv.-Doz. Dr. J. Matthes
2. Gutachter: Univ.-Prof. Dr. K. Mohr
Tag der Promotion: 11.09.2017
Erscheinungsjahr: 2017

Für meine Familie

Table of contents

Abbreviations

AP	action potential
approx.	approximately
bp	base pairs
CaM	calmodulin
$Ca_v1.2$	alpha 1 C pore-forming subunit of the L-type calcium channel
$Ca_vß$	auxiliary beta-subunit of the L-type calcium channel
cDNA	complementary deoxyribonucleic acid
CAD	coronary artery disease
CDI	calcium-dependent inactivation
CICR	calcium-induced calcium-release
CoIP	co-immunoprecipitation
Ct	threshold cycle
CVD	cardiovascular disease
DCM	diabetic cardiomyopathy
DM	diabetes mellitus
dNTP	deoxynucleoside triphosphate
ER	endoplasmatic reticulum
f	female
F	forward primer
GAPDH	glyceraldehyde 3-phosphate dehydrogenase
gDNA	genomic deoxyribonucleic acid
h	hours
HF	heart failure
hz	heterozygous
HPRT	hypoxanthine-guanine phosphoribosyltransferase
I	current
IR	insulin receptor
IRS 2	insulin receptor substrate 2
I/V	current-voltage relationship
JAK	janus kinase
kbp	kilo base pairs
k.o.	knockout
LTCC	L-type calcium channel
m	male
ms	milliseconds
min	minutes
MP	milk powder
NC	nitrocellulose
mRNA	messenger ribonucleic acid

n	number of patched cells / number of blots
N	number of mice / number of ventricles
No.	number
PAGE	polyacrylamide gel electrophoresis
PCR	polymerase chain reaction
PKA	protein kinase A
PKB	protein kinase B
PI3K	phosphatidylinositol 3-kinase
PLN	phospholamban
PVDF	polyvinylidene fluoride
qRT-PCR	quantitative real-time PCR
R	reverse primer
RAAS	renin-angiotensin-aldosterone system
Rad	ras-related associated with diabetes
REST	relative expression software tool
rpm	revolutions per minute
rRNA	ribosomal ribonucleic acid
RyR	ryanodine receptor
S29	ribosomal protein S29
sec	second
SEM	standard error of the mean
SERCA 2	sarcoplasmic/endoplasmic reticulum calcium ATPase 2
STAT	signal transducer and activator of transcription
SR	sarcoplasmatic reticulum
$V_{0.5(in)act}$	potential of half maximal (in)activation
VDI	voltage-dependent inactivation
T1DM	type 1 diabetes mellitus
T2DM	type 2 diabetes mellitus
VDCC	voltage-dependent calcium channel
vs.	versus
wt	wildtype

I. List of figures

II. List of tables

1 Introduction

1.1 Diabetes mellitus & diabetic cardiomyopathy

Diabetes mellitus (DM) is a metabolic disorder that is characterized by a chronic increase of blood glucose concentrations due to defects in insulin signaling. Details of insulin signaling defects are further described in chapter 1.8.1. DM can be classified into the following general categories: type 1 diabetes mellitus (T1DM) and type 2 diabetes mellitus (T2DM). T1DM occurs due to destruction of the insulin secreting β-cells, usually leading to an insulin deficiency. T2DM develops because of insulin resistance and a defect in compensatory insulin secretion (Craig et al., 2014, American Diabetes, 2015).
In 2014 approx. 422 million adults worldwide have suffered from DM compared to 108 million in 1980. During this period, the global prevalence of diabetes in age-standardized adults raised from 4.7 to 8.5 % (WHO, 2016). The rising prevalence of DM is mainly attributed to the increase in T2DM and its main risk factors such as overweight and obesity (Chatzigeorgiou et al., 2009, Wang et al., 2014). DM can lead to clinical complications such as cardiovascular disease (CVD), stroke, nephropathy, leg amputation, retinopathy and neuropathy (WHO, 2016). For example, the risk for diabetic patients to suffer from heart failure (HF) is increased by the factor of two to five compared to non-diabetic patients (de Simone et al., 2010, Nichols et al., 2004, Kannel et al., 1974, Dandamudi et al., 2014). Approx. half of the mortality of diabetic patients is related to CVD (Authors/Task Force et al., 2013, Paneni, 2014, Park and Peters, 2014). In 1972, Rubler and colleagues published post-mortem data from diabetic patients with HF but lacking evidence for the most common causal factors hypertension, myocardial ischemia or congenital or vascular heart disease, respectively (Rubler et al., 1972). Nowadays this is described by the term “diabetic cardiomyopathy” (DCM) and characterized by any abnormality of myocardial diastolic and/or systolic function in diabetic subjects without hypertension or coronary artery disease (CAD). The prevalence of DCM is rising in parallel with the increasing incidence of obesity and T2DM (Jia et al., 2016). So far, the pathophysiology of DCM is not fully elucidated. Several molecular mechanisms are described that contribute to its development, e.g. altered insulin signaling, impaired calcium (Ca^{2+}) handling, increased fatty acid (FA) utilization and oxidative stress (figure 1.1; Bugger and Bode, 2015, Yilmaz et al., 2015, Bugger and Abel, 2014). To date, intense research is focusing on the mechanisms of DCM to develop therapeutic strategies for the treatment of DCM. Diabetic mouse

models are important research tools to elucidate the mechanisms of DCM. One advantage is that diabetic mice do not manifest severe atherosclerosis, a main cause for CAD (Back and Hansson, 2015, Pjanic et al., 2016, Vikramadithyan et al., 2005). Thus, heart failure development is not “contaminated” by CAD.

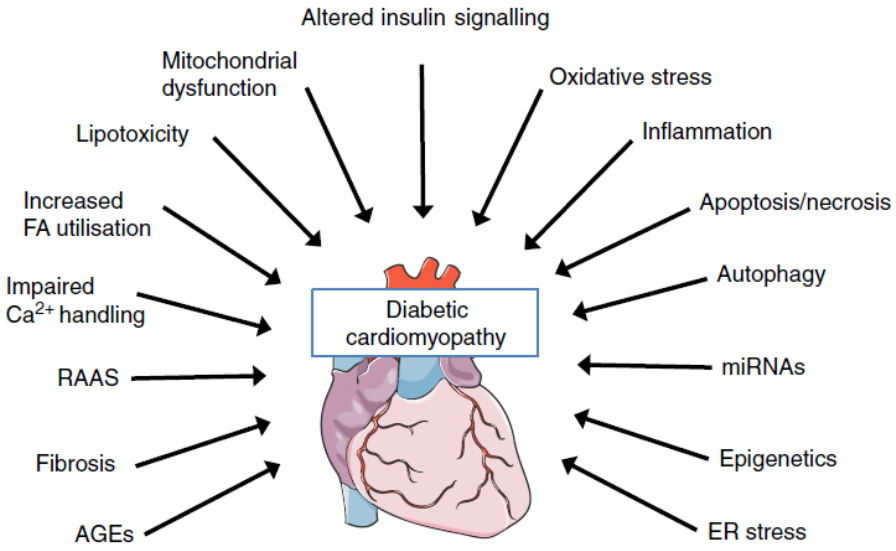

Figure 1.1 **The pathophysiology of diabetic cardiomyopathy (DCM)**: several molecular mechanisms are described that contribute to the development of DCM, e.g. altered insulin signaling, impaired calcium (Ca^{2+}) handling and oxidative stress (AGEs = advanced glycation endproducts, RAAS = renin–angiotensin–aldosterone system, FA = fatty acid, miRNAs = micro ribonucleic acids, ER = endoplasmatic reticulum; Bugger and Abel, 2014).

1.2 Principles of cardiac function - calcium & excitation-contraction coupling

Intracellular Ca^{2+} is an essential signaling molecule that controls important cellular processes. It is important in regulating action potentials (APs), excitation-contraction coupling, mitochondrial energy production, Ca^{2+}/calmodulin-dependent protein kinase II activity and nuclear gene expression (Winslow et al., 2016). Cardiac excitation-contraction coupling is defined as the process of sarcolemmal depolarization leading to an increase of the cytosolic Ca^{2+} concentration that initiates contraction of the heart (Winslow et al., 2016). In detail, depolarization of the cardiac myocyte membrane activates L-type Ca^{2+} channels (LTCCs) that lead to an initial Ca^{2+} influx. As illustrated in figure 1.2, the Ca^{2+} influx induces the release of further Ca^{2+} from the sarcoplasmic reticulum (SR) via the ryanodine receptor (RyR), a process called calcium-induced calcium-release (CICR). This increase of intracellular Ca^{2+} enables muscle contraction

by binding of Ca^{2+} to the myofilament protein troponin C. For myocyte relaxation the intracellular Ca^{2+} concentration has to decline so that Ca^{2+} dissociates from troponin C (Bers, 2002). Sarcoplasmic/endoplasmic reticulum calcium ATPase 2 (SERCA2) and its endogenous inhibitor phospholamban (PLN) are important for mediating the SR Ca^{2+} uptake from the cytosol (Feijoo-Bandin et al., 2015). Lowering of intracellular Ca^{2+} can also be achieved via the sarcolemmal Ca^{2+}-ATPase, the sarcolemmal Na^{+}/Ca^{2+}-exchanger or mitochondrial Ca^{2+} uniport (Bers, 2002). Since Ca^{2+} plays such an important role in heart function, impaired Ca^{2+} handling is associated with various forms of cardiac diseases (Winslow et al., 2016).

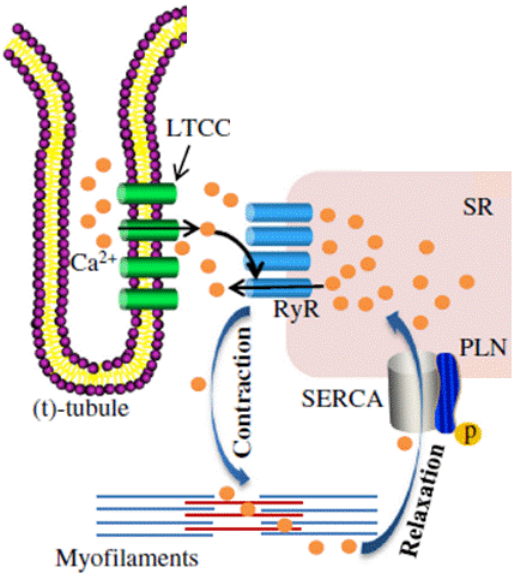

Figure 1.2 **Calcium signaling in cardiomyocytes and excitation-contraction coupling.** Upon depolarization of the cardiomyocyte membrane L-type Ca^{2+} channels (LTCCs) generate a Ca^{2+} influx. The increasing Ca^{2+} concentration induces the release of further Ca^{2+} from the sarcoplasmic reticulum (SR) via the ryanodine receptor (RyR) and finally induces muscle contraction. Myocyte relaxation is mediated via mechanisms that decline the Ca^{2+} concentration, e.g. sarcoplasmic/endoplasmic reticulum calcium ATPase2 (SERCA2) activation and phospholamban (PLN) phosphorylation (modified from Feijoo-Bandin et al., 2015).

1.3 Voltage-dependent calcium channels

Voltage-dependent calcium channels (VDCCs) are involved in several physiological processes such as muscle contraction, glandular secretion, neurotransmission and gene expression (Catterall et al., 2003). The molecular composition of VDCCs is characterized by a heteromeric polypeptide complex that consists of a transmembrane pore-forming α1-subunit and accessory ß- and α2-δ-subunits as well as an accessory γ-subunit in several calcium channel subtypes (figure 1.3, Campiglio and Flucher, 2015). γ-subunits are unlikely to play a role as part of the cardiac VDCC complex, although they are able to modulate cardiac calcium channel functions in recombinant expression systems (Yang et al., 2011).

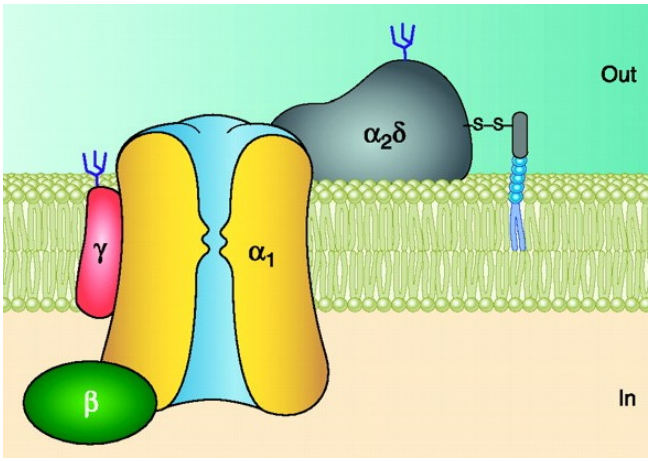

Figure 1.3 **Molecular subunit composition of VDCCs:** the heteromeric proteins consist of a pore-forming α1-subunit, accessory ß- as well as α2-δ-subunits and possibly a γ-subunit (Buraei and Yang, 2010).

Each type of VDCC subunit is encoded by several genes, reflecting the diversity of Ca^{2+} channel structure and function (Zamponi et al., 2015, Catterall, 2011). Based on structural relationships among the different α1-subunit isoforms, VDCCs are classified in three α1-subunit gene subfamilies, i.e. Ca_v1, Ca_v2 and Ca_v3. Each subfamily contains several isoforms, such as $Ca_v1.1$, $Ca_v1.2$, $Ca_v1.3$ and $Ca_v1.4$ in case of the Ca_v1 subfamily. $Ca_v1.2$ is the predominant cardiac α1-subunit isoform (encoded by the cacna1c gene) and mainly responsible for the Ca^{2+} influx during excitation-contraction coupling (Ertel et al., 2000, Zamponi et al., 2015).

VDCCs can be further distinguished by their (electro-)physiological and pharmacological properties leading to a differentiation in L-, P/Q-, N-, R- and T-type Ca^{2+} currents (Catterall et al., 2005). L-Type Ca^{2+} currents are named according to their long-lasting currents if barium is the charge carrier and are mediated by L-Type calcium channels

(LTCCs). LTCCs show a slow voltage-dependent inactivation and a large single-channel conductance. These channels start to activate at membrane potentials above -40 mV and therefore belong to the so-called high-voltage activated channels. LTCCs can be blocked by several ligands such as dihydropyridines, phenylalkylamines and benzothiazepines (Neumaier et al., 2015, Catterall, 2011).

LTCCs exist in three different conformations: closed (C), open (O) and inactive (I) state, as demonstrated in figure 1.4. At the resting membrane potential of about -80 mV, LTCCs are in the closed conformation. Upon depolarization, voltage-gated LTCCs open (conducting state) and Ca^{2+} ions enter the cell. Subsequently, open channels change to either the closed or the inactivated (non-conducting) state. The inactivated conformation is provoked by time- or rather Ca^{2+}-dependent inactivation (CDI) and/or by voltage-dependent inactivation (VDI). Repolarization is necessary for recovery from inactivation after that channels can be activated again. If a depolarizing pulse arrives prior to complete recovery, less or even no Ca^{2+} ions enter the cell. Taken together, the Ca^{2+} entry is regulated by the membrane potential, the LTCC kinetics of opening, the kinetics of inactivation (CDI, VDI) and the kinetics of recovery from inactivation (Hering et al., 2000). CDI and VDI are regulated by the interaction of the $Ca_v1.2$ α1-subunit with the Ca_vß-subunit and/or the calcium sensor calmodulin (CaM) (Neumaier et al., 2015, Van Petegem and Minor, 2006).

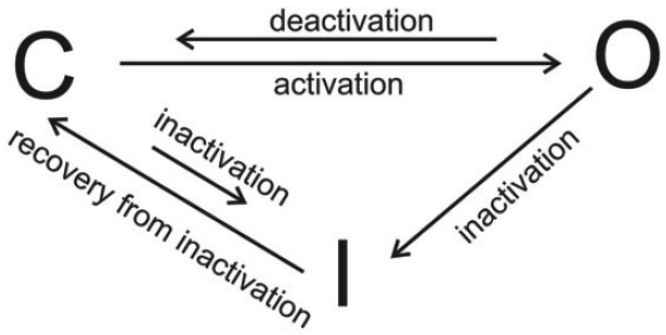

Figure 1.4 **LTCC conformations:** LTCCs can exist in a closed (C), open (O) and inactive (I) state (Karmazinova and Lacinova, 2010).

Since this study focused on cardiac LTCCs, their properties are explained in more detail here.

1.3.1 The pore-forming $Ca_v1.2$ α1-subunit

The pore-forming $Ca_v1.2$ α1-subunit is responsible for ion trafficking and represents the largest LTCC subunit of approx. 210-240 kDa. Varying band sizes in Western Blots are mainly attributed to truncations of the proteins' C-terminus due to the expression system or experimental conditions (De Jongh et al., 1996, Weiss et al., 2013, Shaw and Colecraft, 2013). As demonstrated in figure 1.5, the $Ca_v1.2$ subunit consists out of four homologous domains (I–IV). Each domain is composed of six membrane-spanning segments that include the voltage-sensing domain (VSD) and the pore domain (PD) with the Ca^{2+} selectivity filter. The $Ca_v1.2$ α1-subunit further contains the Ca_vβ-subunit binding site (referred to as α1-interaction domain/AID) as well as structural domains responsible for CDI, VDI and ligand binding (Neely and Hidalgo, 2014, Hofmann et al., 2014).

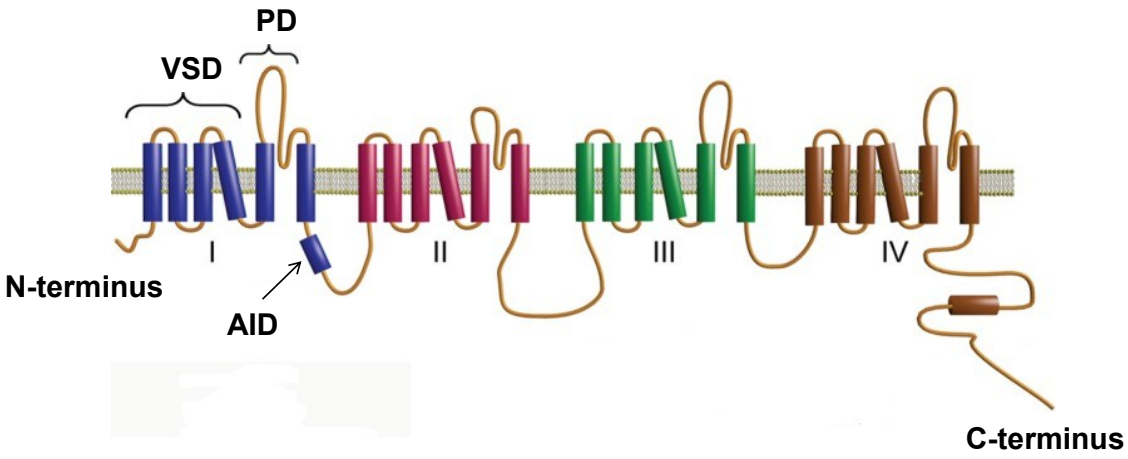

Figure 1.5 **Structure of the $Ca_v1.2$ α1-subunit:** The pore-forming protein mediates most of the LTCC functions and consists of four homologous domains (I–IV). The subunit contains the β-subunit binding site (referred to as α1-interaction domain/AID), the voltage-sensing domain (VSD), the pore domain (PD) including the selectivity filter and binding sites for ligands (modified from Neely and Hidalgo, 2014).

1.3.2 The Ca_vß-subunit

The auxiliary Ca_vβ-subunit (approx. 55 kDa) modulates LTCC gating properties and consists of a Src homology 3 domain (SH3) and a guanylate kinase (GK) domain. Both domains are linked by the so-called HOOK region and flanked by N- and C-termini (NT and CT), as shown in figure 1.6 (A) (Buraei and Yang, 2010). The GK domain contains the α1-binding pocket which interacts with the AID of the Ca_vα1-subunit (figure 1.5 (B); Chen et al., 2004, Almagor et al., 2012, Van Petegem et al., 2004).

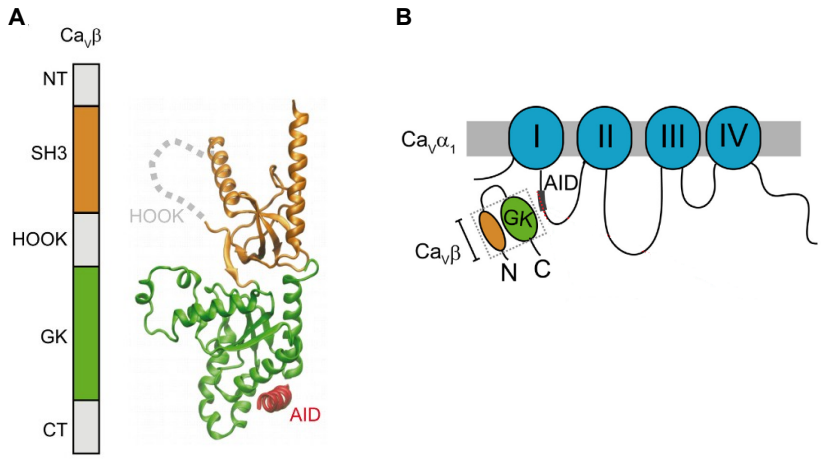

Figure 1.6 **Structure of the Ca$_V$ß-subunit:** figure (A) illustrates the domain organization and three-dimensional structure. The subunit consists of a core region flanked by N- and C-termini (NT and CT). The core region is built by the Src homology 3 (SH3) and the guanylate kinase (GK) domains connected via the so-called HOOK region. The GK domain interacts with the AID of the α1-subunit (B) (modified from Neely and Hidalgo, 2014).

Up to now, four Ca$_V$ß-subunit isoforms (Ca$_V$β1-Ca$_V$β4) have been identified. Ca$_V$β1, Ca$_V$β2 and Ca$_V$β3 are expressed in the heart, while Ca$_V$β4 was only found in young rat atrial myocytes, so far (Buraei and Yang, 2010, Chu et al., 2004).

Ca$_V$ß-subunits increase LTCC activity, regulate LTCC membrane expression and possess binding sites for several proteins such as RGK proteins. These characteristics are pronounced differentially among the several subtypes. E.g. Ca$_V$β2, the predominant cardiac isoform, increases LTCC activity most (Colecraft et al., 2002, Hullin et al., 2003, Hullin et al., 2007, Buraei and Yang, 2013).

1.3.1 The Ca$_V$α2-δ-subunit

The auxiliary Ca$_V$α2-δ-subunit (approx. 170 kDa) consists of a large, extracellular α2-subunit and a small transmembranic δ-subunit which has a short intracellular region. Both subunits are linked through a disulfide bridge. The Ca$_V$α2-δ-subunit is encoded by a single gene and post-translationally cleaved into the α2 and the δ polypeptides. So far, at least 4 mammalian isoforms (Ca$_V$α2-δ-1 - Ca$_V$α2-δ-4), encoded by different genes, have been identified (Bodi et al., 2005, Catterall, 2011). All isoforms were reported to be present in the cardiovascular system. However, functional differences on LTCC regulation are not known so far (Hofmann et al., 2014). Indeed, the functional role of the Ca$_V$α2-δ-subunit is poorly understood. In heterologous expression systems it increases the channel expression and enhances its function, but to a lesser extent and in a more channel-specific way compared to Ca$_V$ß-subunits (Catterall, 2011).

1.4 RGK proteins

The RGK proteins belong to the RAS GTPase superfamily and are represented by four related proteins: Rad, Gem/Kir, Rem 1 and Rem 2. The monomeric G proteins have low molecular masses ranging from 20 to 40 kDa (Neely and Hidalgo, 2014). All RGK proteins share a common structure including (I) a variable N-terminal segment, (II) a G-domain, involved in guanine nucleotide binding, and (III) a C-terminal segment, that contains a CaM binding site and the poly-basic membrane targeting sequence (Sasson et al., 2011). Although RGK proteins are structurally related they show different tissue expressions (Flynn and Zamponi, 2010):

- Rad and Rem 1 are mainly expressed in cardiac, skeletal and smooth muscle cells (Chang and Colecraft, 2015).
- Rem 2 is abundantly expressed in the nervous system, in kidney and liver, but is barely detectable in heart (Finlin et al., 2000, Liput et al., 2016).
- Gem/Kir is found in diverse tissues, including heart, thymus, spleen, kidney, lung (Maguire et al., 1994, Murata et al., 2004).

1.4.1 RGK-VDCC interaction

One main function of RGK proteins is the inhibition of VDCCs (Correll et al., 2008). Up to now, three different mechanisms of inhibition are suggested:

1. RGK proteins inhibit the channel trafficking to the cell surface and decrease its surface expression (Yada et al., 2007, Jhun et al., 2012, Yang et al., 2010, Sasaki et al., 2005, Yang et al., 2012, Beguin et al., 2006, Beguin et al., 2001).
2. RGK proteins suppress membrane-resident VDCCs via immobilization of the voltage sensor (Yang et al., 2010, Yang et al., 2012, Meza et al., 2013, Magyar et al., 2012).
3. RGK proteins suppress membrane-resident VDCCs via reduction of the open probability (Yang et al., 2012, Xu et al., 2010, Yang et al., 2010).

As illustrated in figure 1.7, it has been suggested that the Ca_vß-subunit binds to the AID of the Ca_vα1-subunit and induces a conformational change (ß primes α1) (Fan et al., 2010). Then, VDCC inhibition can be induced by either RGK-Ca_vα1 binding (A), by a tripartite complex (B) or by RGK-Ca_vß binding (C) (Fan et al., 2010, Correll et al., 2008, Béguin et al., 2007, Finlin et al., 2006, Yang et al., 2007, Buraei and Yang, 2015).

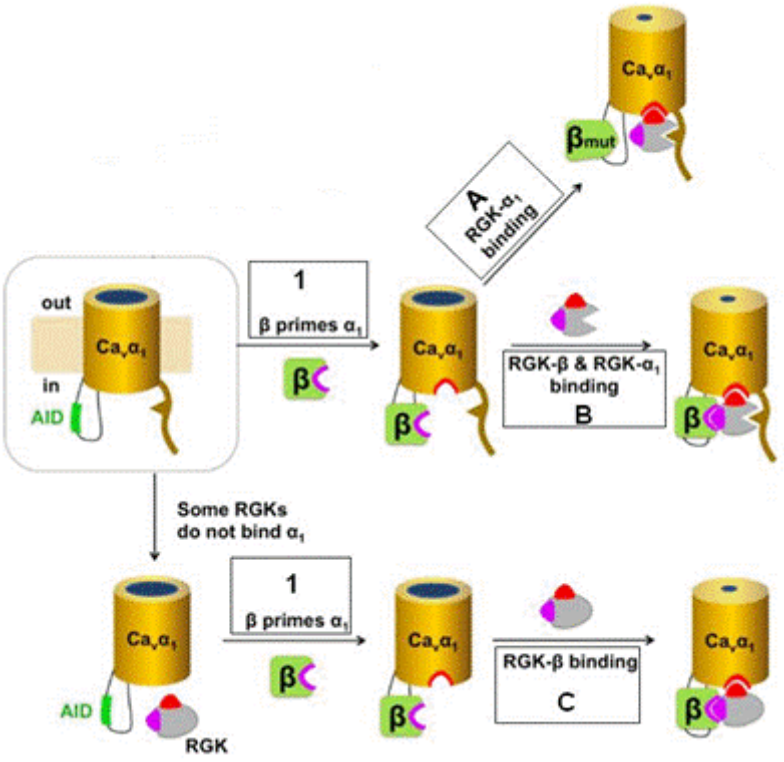

Figure 1.7 **Mechanisms of VDCC inhibition by RGK proteins**: the interaction of the Ca_vß-subunit with the AID of the Ca_vα1-subunit induces a conformational change in Ca_vα1 (ß primes α1). Then, VDCC inhibition can be induced by either RGK-Ca_vα1 binding (A), by a tripartite complex (B) or by RGK-Ca_vß binding (C) (modified from Buraei and Yang, 2015).

1.5 LTCCs in heart failure

Heart failure (HF) is a clinical syndrome that occurs due to structural and/or functional cardiac abnormalities which impair the ventricle to pump blood with normal efficiency. This leads to a reduced cardiac output and/or elevated intracardiac blood pressures (Ponikowski et al., 2016). Cardiac LTCCs are important for proper excitation-contraction coupling (Rougier and Abriel, 2016). Therefore, alterations in LTCC expression and function are of high interest to elucidate the pathophysiology of HF. It was consistently found that LTCC whole-cell Ca^{2+} current density in cardiomyocytes from failing human ventricles or animal models of HF was (almost) unchanged compared with non-failing

ventricles (Mukherjee and Spinale, 1998, Richard et al., 1998). Interestingly, a significantly increased single-channel activity was shown in ventricular myocytes from human end-stage failing hearts (Schroeder et al., 1998). The finding of an increased single-channel activity might result from an enhanced ß-adrenergic stimulation, that is known to be increased in case of developing HF (Madamanchi, 2007). This is consistent with findings of a blunted response to β-adrenergic receptor agonists in human failing hearts (Chen et al., 2002). Another reason for the increased single-channel activity might be the cardiac upregulation of the Ca_vß2-subunits in human failing hearts (Hullin et al., 2007). In a mouse model of cardiac Ca_vß2-subunit overexpression observed LTCC properties were similar to LTCC function in chronic human HF (Beetz et al., 2009). Hong and colleagues determined the total amount of transmembrane $Ca_v1.2$ channels in failing human hearts; the amount of the protein expression was unchanged but the channels were less abundant in the T-tubuli (Hong et al., 2012). These findings fit earlier radioligand binding studies (Takahashi et al., 1992, Gruver et al., 1994). Taken together, a more active state of present channels accompanied by less surface channels was suggested to occur in failing ventricles (Schroeder et al., 1998).

1.6 RGK-LTCC interaction in the context of DCM

In human HF LTCC density was unchanged, while the activity of single LTCCs was increased (described in the previous chapter). Candidates that might be involved in modulation of expression and function of LTCCs are RGK proteins, such as Rad. Rad expression was found to be reduced in human HF (Chang et al., 2007) and in Rad-knockout (k.o.) mice whole-cell Ca^{2+} current densities were increased (Manning et al., 2013). The effect of Rad on LTCC function and expression in a diabetic context is still unclear. Rad was initially identified and named as “RAS-related protein associated with diabetes” because its expression was upregulated in skeletal muscle of humans with T2DM (Reynet and Kahn, 1993). Since insulin infusion induced a significant increase in the mRNA level in percutaneous biopsies of human vastus lateralis muscles (Laville et al., 1996), the Rad gene is suggested to be insulin-regulated. Therefore, Rad might be an important candidate for LTCC modulation in DCM. Studies to investigate this issue were initially conducted by our group, as outlined in figure 1.8 (Fabisch, 2010, unpublished data). Protein analysis of Rad and $Ca_v1.2$ α1-subunit expression (henceforward only referred to $Ca_v1.2$) in ventricular tissue of mice with diabetes-associated metabolic disturbances were positively correlated suggesting a rather

compensatory role of Rad, e.g. to prevent Ca^{2+} overload. Of note, there have been differences in the extent and/or direction of altered $Ca_v1.2$ and Rad expression compared to wildtype (wt) littermates (figure 1.8; Fabisch, 2010, unpublished data). In a mouse model associated with DCM (the so-called db/db mice with leptin receptor deficiency) our group detected a reduced whole-cell Ca^{2+} current density with unchanged single-channel activity (Pereira, 2006). The reduced whole-cell Ca^{2+} current density was attributed to a reduced expression of the LTCC pore $Ca_v1.2$ (Pereira, 2006). These results are in contrast to the findings in human HF. Therefore, putative differential effects of Rad on modulating LTCCs might exist depending on the diabetic or non-diabetic context.

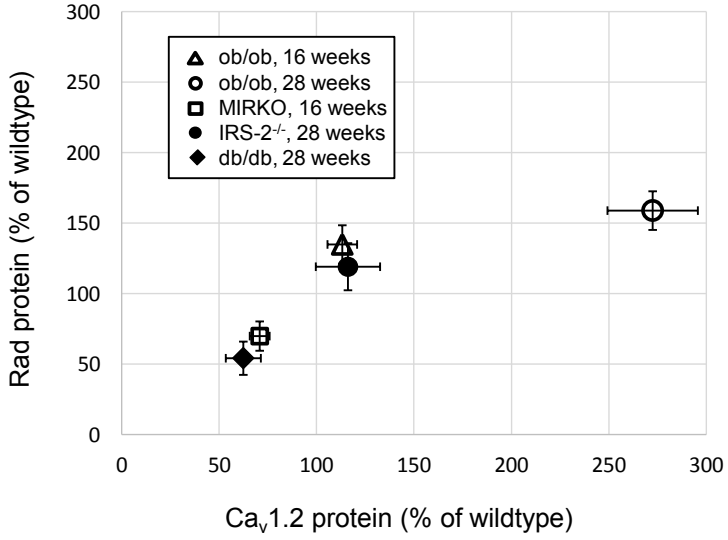

Figure 1.8 **Rad and $Ca_v1.2$ protein expression** in ventricular tissues of mice with diabetes-associated metabolic disturbances. The expression of Rad and $Ca_v1.2$ protein was found to be positively correlated (ob/ob mice = mice that are deficient for leptin, MIRKO mice = muscle-specific insulin receptor knockout mice, IRS-$2^{-/-}$ = mice lacking the insulin receptor substrate 2, db/db mice = mice with leptin receptor deficiency; Fabisch, 2010, unpublished data).

1.7 Animal models of DCM

As mentioned in chapter 1.6, Rad and $Ca_v1.2$ protein expression seem to be positively correlated in ventricular tissues of mice with diabetes-associated metabolic disturbances. We chose two of the previously screened mouse models differing mainly by body weight and amount of blood glucose enhancement for further analysis, i.e. mice that are deficient for leptin (ob/ob) and mice lacking the insulin receptor substrate 2 (IRS 2). Mice of different ages (16 and 28 weeks) were chosen for experiments to take time-dependent onset of obesity and disease progression of T2DM into account. Age-

matched wildtype (wt) mice were used as controls. So far, other studies solely focused on a complete (and thus artificial) k.o. of RGK proteins, while this study focused on a differential rather “secondary” change of RGK protein expression. Rad-k.o. mice served as internal control mice and should reveal the maximum effect of a loss of Rad protein on LTCC expression and function. Furthermore, ob/ob x Rad-k.o. mice were generated in order to check whether the role of Rad differs depending on the murine background.

1.7.1 ob/ob mice

Ob/ob mice are globally deficient for leptin due to a spontaneously occurred mutation in the gene Lep^{ob} of the mouse strain V/Le in The Jackson Laboratory, Bar Harbor, USA in 1949 (Ingalls et al., 1950). After backcrossing for more than 45 generations mice have been available on a C57BL/6J background (Mouse Genome Database, 2017). The autosomal recessive, single gene mutation is located on chromosome six of leptin and based on the nonsense mutation in codon 105. In detail, a stop codon occurs because of an amino acid change and these mice release a truncated version of the adipocyte peptide hormone leptin. In ob/ob mice leptin mRNA levels are highly increased by the factor 20 compared to wt mice. However, this mRNA is mutated and resulting proteins are not functional (Zhang et al., 1994, Moon and Friedman, 1997, Wang et al., 2014). Leptin is known as a negative regulator of food intake; its lack results in an increased availability of the potent appetite-stimulant neuropeptide Y (Lee and Cox, 2011). Therefore, ob/ob mice possess an obese phenotype (Chatzigeorgiou et al., 2009), exhibit early-onset hyperglycemia, hyperinsulinemia and insulin resistance already four to six weeks after birth (Lindstrom, 2007, Mazumder et al., 2004, Haluzik et al., 2004, Buchanan et al., 2005).

1.7.2 IRS 2-knockout mice

Mice lacking the insulin receptor substrate 2 (IRS 2-k.o. mice) were first described in the late 20th century (Withers et al., 1998, Kubota et al., 2000). IRS 2-k.o. mice exhibit early-onset hyperglycemia, hyperinsulinemia and insulin resistance at an age of approx. six weeks. This mouse line shows no or only mild obesity (Sesti et al., 2001, Burks et al., 2000, Withers et al., 1998, Kubota et al., 2000).
IRS 2 is an ubiquitously expressed cytoplasmic protein that regulates biological

processes such as glucose metabolism, protein synthesis and cell survival. It is an important molecule in insulin signaling (Oliveira et al., 2014, Mardilovich et al., 2009). To date, four closely related insulin receptor substrates (IRS 1- 4) have been identified that differ in tissue distribution, subcellular localization, developmental expression, binding to the insulin receptor and interaction with SH2 domain containing proteins (Sesti et al., 2001). Both, IRS 1 and IRS 2 are the predominant family members expressed in the heart (Riehle and Abel, 2016).

1.8 Leptin and insulin

1.8.1 Insulin function and signaling pathway

Insulin is a key metabolic peptide hormone involved in carbohydrate, lipid and protein metabolism (Newsholme and Dimitriadis, 2001). It is synthesized by β-cells of the pancreas and secreted in response to enhanced concentrations of blood glucose. Although insulin mainly acts in liver, adipose tissue and skeletal muscle, insulin receptors (IRs) are widely expressed in the mammalian body (Belfiore et al., 2009). Binding of insulin to the IR leads to an autophosphorylation and IR activation (figure 1.9). Following IR activation two canonical signaling pathways are possible:

1. The phosphatidylinositol 3-kinase (PI3K)/Akt pathway is responsible for metabolic effects. In the PI3K/Akt pathway the IR phosphorylates tyrosine residues of IRS1/IRS2, which act as docking platforms for the Src homology 2 domain of PI3K. This finally promotes an activation of protein kinase B (PKB) or Akt (Baumgard et al., 2016). In the heart signaling via PI3K/Akt mediates metabolic effects such as an increase in glucose uptake, coronary vasodilation, substrate flexibility and energy homeostasis (Jia et al., 2016).

2. The Ras/mitogen-activated protein kinase pathway is accountable for effects on cell growth and proliferation (Jia et al., 2016).

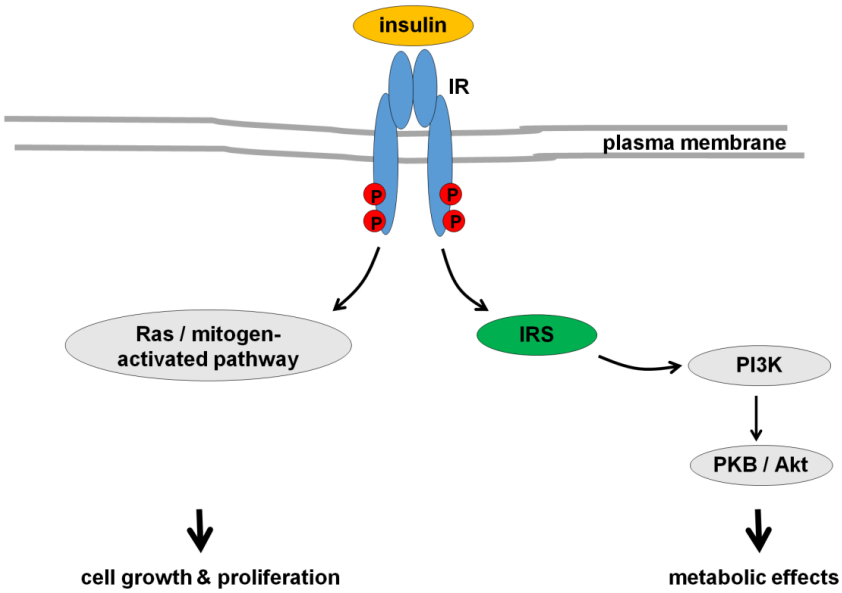

Figure 1.9 **Insulin signaling pathway:** binding of insulin to the insulin receptor (IR) can activate two canonical signaling pathways: the phosphatidylinositol 3-kinase (PI3K)/Akt pathway, responsible for metabolic effects, and the Ras/mitogen-activated protein kinase pathway, accountable for effects on cell growth and proliferation.

The impairment of key insulin signaling molecules such as IRS, PI3K or Akt might be involved in the development of insulin resistance (Yang et al., 2016). Insulin resistance as a key feature of type 2 diabetes is caused by various factors, e.g. by obesity, hyperglycemia, hyperlipidemia, hyperinsulinemia and/or activation of the RAAS/the sympathetic nervous system. These factors are suggested to contribute to an increased activation of enzymes that phosphorylate IRS proteins. A serine phosphorylation of IRS proteins attenuates IRS tyrosine phosphorylation. Other molecular mechanisms leading to a diminished strength of the PI3K/Akt pathway are proteasomal degradation of IRS proteins and decreased activation of downstream signaling molecules such as Akt (Aroor et al., 2012, Ye, 2013, Kim et al., 2008). Therefore insulin resistant tissues exhibit an imbalance in the metabolic and growth effects of insulin signaling, with the actions of the Ras/mitogen-activated protein kinase pathway dominating (Jia et al., 2016, Wang et al., 2004). In the prediabetic state insulin resistant individuals compensate the disturbed PI3K/Akt signaling by secreting more insulin (Hardie, 2012). The compensatory mechanism also includes an increase in glucose oxidation, in fatty acid oxidation and in glycerolipid-free fatty acid cycling (Wortham and Sander, 2016). Such an adaption mechanism may predispose ß-cells to lipotoxicity. This term describes a process that results in down-regulation of insulin, ß-cell dysfunction and apoptosis (Fu et al., 2013). Upon exhaustion of ß-cells this failure in compensation mechanism may lead to T2DM (Hardie, 2012). Generalized insulin resistance is also

associated with HF (Velez et al., 2014) and insulin resistance of the heart might directly contribute to cardiac dysfunction (Aroor et al., 2012).

1.8.2 Leptin function and signaling pathway

Leptin is a known negative regulator of food intake and regulates a variety of other functions such as neuroendocrine functions, fertility, angiogenesis and long-term energy balance (Chan and Leung, 2015). Leptin is primarily produced in the adipose tissue (Fernandez-Formoso et al., 2015). The hormone is secreted into the bloodstream by adipocytes (Zhou and Rui, 2013) and mediates its effects through leptin receptors. Leptin receptors are widely expressed in the mammalian body, e.g. in liver, heart, kidneys, lungs, pancreas and adipose tissue (Margetic et al., 2002). Among the known six leptin receptor isoforms, the Lepr-b receptor, which is highly expressed in the hypothalamus, is known to mediate its main effects via the JAK (janus kinase)/STAT (signal transducer and activator of transcription) pathway, as outlined in figure 1.10 (Fernandez-Formoso et al., 2015).

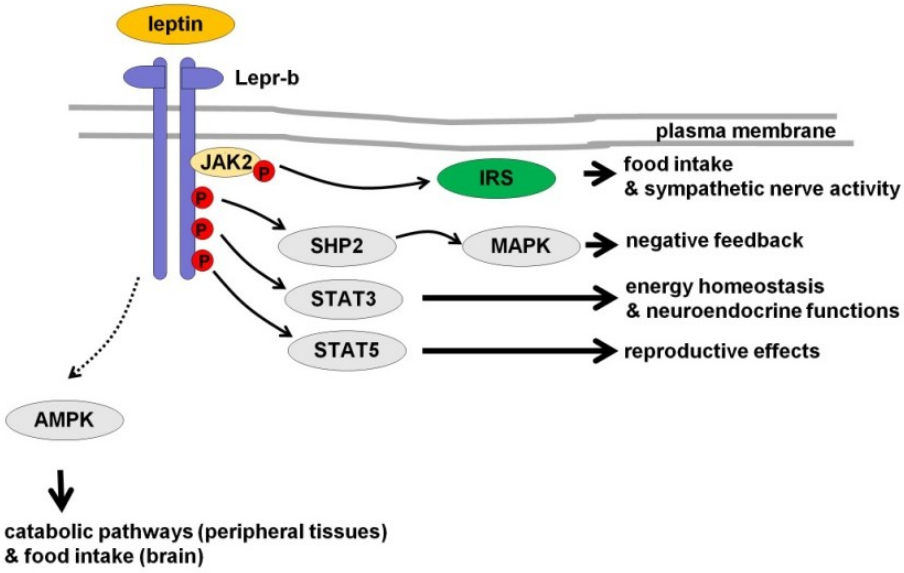

Figure 1.10 **Leptin signaling pathway:** binding of leptin to the leptin receptor (Lepr-b) activates JAK2, which phosphorylates JAK2 itself and three tyrosine residues on Lepr-b. Each of these phosphorylation sites triggers a specific signaling pathway. A phosphorylated JAK2 leads to a phosphorylation of IRS molecules and activation of PI3K.

In brief, leptin binding to Lepr-b activates JAK2 which phosphorylates itself and three tyrosine residues on Lepr-b. Each of these phosphorylation sites triggers a specific signaling pathway, as demonstrated in figure 1.10. A phosphorylated JAK2 leads to a

phosphorylation of IRS molecules and activation of PI3K, a pathway necessary for leptin's effects on food intake and sympathetic nerve activity (Munzberg and Morrison, 2015). Similar to the manifestation of insulin resistance and compensatory hyperinsulinemia, leptin resistance and hyperleptinemia can develop, especially in obese patients and rodents (Konner and Bruning, 2012).

1.8.3 Link between insulin and leptin

Insulin and leptin receptors are widely expressed in mammalian tissues. Co-expression in the same tissue might enable an interaction of both receptors. Insulin and leptin mediate some of their physiological effects via IRS signaling. An interaction between both pathways is possible via IRS 2, but also via other downstream elements such as PI3K or STAT (Szanto and Kahn, 2000, Carvalheira et al., 2003, Carvalheira et al., 2001). Especially in obese mammals insulin and leptin signaling may be altered. Both hormones are of major importance for cardiac contractility, growth and metabolism (Westermeier et al., 2016, Feijoo-Bandin et al., 2015). Leptin and insulin signaling might be involved in the regulation of LTCCs (Ballou et al., 2015, Viard et al., 2004).

1.9 Aim of the study

Cardiovascular disease (CVD) is a leading cause of death for diabetic patients (Sowers and Lester, 1999, Balakumar et al., 2016). Diabetic cardiomyopathy (DCM) is characterized by an abnormality of myocardial diastolic and/or systolic function in diabetic subjects without the major heart failure risk factors hypertension and/or (overt) coronary artery disease (Jia et al., 2016). Since cardiac L-Type calcium channels (LTCCs) are known to be involved in proper excitation-contraction coupling, they are of high interest in the research of CVD, such as DCM and resulting heart failure (HF). In human (non-diabetic) HF whole-cell Ca^{2+} current density of ventricular LTCCs was unchanged compared to non-pathophysiological conditions, while single-channel activity was significantly increased (Mukherjee and Spinale, 1998, Schroeder et al., 1998). These findings suggest changes in both, expression and function of LTCCs. In contrast to humans, whole-cell Ca^{2+} current density was reduced in a mouse model associated with DCM (the so-called db/db mice with leptin receptor deficiency), while single-channel activity was unchanged (Pereira, 2006).

It has been shown that RGK proteins, like the diabetes-associated Rad, might be involved in LTCC regulation, both regarding its function and expression. Rad expression is reduced in human heart failure (Chang et al., 2007) and whole-cell Ca^{2+} current densities are increased in cardiomyocytes of Rad-k.o. mice (Manning et al., 2013). So far, the effect of Rad on cardiac LTCCs even in a diabetic context is unclear. Previous data suggest that the ventricular expression levels of Rad and $Ca_v1.2$ proteins are positively correlated in several mouse models with diabetes-associated metabolic disturbances (Fabisch, 2010). Differences in the extent and/or direction of altered $Ca_v1.2$ and Rad protein expression might be due to a differential regulation depending on e.g. the genotype, age and/or the onset and severity of metabolic disturbances. For a more detailed analysis two diabetic mouse models were investigated in the present study: leptin-deficient obese ob/ob mice and mice lacking insulin receptor substrate 2 (IRS 2), respectively. Though experiments with Rad-k.o. and Rem 1-k.o. mice suggest an impressive inhibitory effect of RGK proteins on native cardiac LTCCs (Magyar et al., 2012, Manning et al., 2013), it remains unclear whether differential expression of RGK proteins might be compensatory, causative or both regarding LTCC regulation. Thus, the present study aims at the role of an in vivo regulation of Rad expression on ventricular LTCCs in two established diabetes mouse models (ob/ob and IRS 2-knockout mice). Therefore, ventricular whole-cell L-type calcium current densities were obtained by patch-clamp recordings and compared to those of wildtype littermates in the context of ventricular expression levels of Rad and $Ca_v1.2$ mRNA and protein. In order to further evaluate the role of Rad in ob/ob mice, we generated and analyzed ob/ob mice lacking Rad. In summary, it should be elucidated whether there is an unifying effect of Rad on LTCCs in diabetic hearts that might suggest a mechanism underlying diabetic cardiomyopathy.

2 Materials and methods

2.1 Materials

2.1.1 Chemicals

Description	Order No.	Supplier/manufacturer
Acetic acid	3738.2	Roth
Magnesium-adenosine 5′-triphosphate (Mg-ATP)	A9187-1G	Sigma-Aldrich
Agarose powder	2267.4	Roth
Amberlite®	K306.1	Roth
Ammonium peroxodisulfate (APS)	9592.3	Roth
Boric acid	3678542	Merck
Bovine serum albumin (BSA)	A6003-25G	Sigma-Aldrich
Bromphenol blue	8122	Merck
Caesium chloride (CsCl)	8627.3	Roth
Calcium chloride dihydrate ($CaCl_2$*$2H_2O$)	T885.2	Roth
Coomassie	3862.1	Roth
Diethylpyrocarbonate (DEPC)	K028.1	Roth
DNA-ExitusPlus™BC	A7089,0500	AppliChem
DNA Gel Loading Dye (10 x)	R0611	Thermo Fisher Scientific
Dulbecco's Modified Eagle's Medium	31966-021	Gibco Thermo Scientific
Ethanol	2246.2500	Th.Geyer
Ethidium bromide	2218.3	Roth
Ethylenediaminetetraacetic acid (EDTA)	8043	Roth
Ethylene glycol-bis(2-aminoethylether)-N,N,N′,N′-tetraacetic acid (EGTA)	E-4378	Sigma-Aldrich
Fetal calf serum (FCS)	S0115	Biochrom
D(+)-Glucose monohydrate	X997.2	Roth
Glycerol	3783.1	Roth
Glycin	G7126-1KG	Sigma-Aldrich
Glyoxal	50649-25ml	Sigma-Aldrich
Heparin	H3393.100KU	Sigma-Aldrich
Iodoacetic acid sodium salt	I2512	Sigma-Aldrich

Description	Order No.	Supplier/manufacturer
Magnesium chloride hexahydrate ($MgCl_2*6H_2O$)	1.05833.0250	Merck
Magnesium sulfate heptahydrate ($MgSO_4*7H_2O$)	1.05886	Merck
2-mercaptoethanol	M6250-100ml	Sigma-Aldrich
Methanol (MeOH)	4627.5	Roth
Milk powder	T145.1	Roth
N,N-bis(2-hydroxyethyl)-2-aminoethanesulfonic acid (BES)	9134.3	Roth
Nonidet®P40 BioChemica	A16940250	Applichem
Orange G 6x Loading Dye	845-ST-4010003	Analytik Jena AG
Penicillin/Streptomycin (100 x)	P11-010	PAA Laboratories GmbH
Percoll	17-0891-01	GE Healthcare Life Sciences
Phosphate-Buffered Saline (PBS)	14190-094	Gibco Thermo Scientific
Pierce®Protein A/G Magnetic Beads	88802 /88803	Thermo Fisher Scientific
4-(2-hydroxyethyl)-1-piperazineethanesulfonic acid (HEPES)	H3375-500G	Sigma-Aldrich
Polysorbate 20 (Tween 20)	A4974,0250	AppliChem
Ponceau S	P3504	Sigma-Aldrich
Potassium chloride (KCl)	6781.1	Roth
Rotiphorese®Gel 40 (19:1)	3030.1	Roth
Saline 0.9 %	6340501	AlleMan Pharma GmbH
Sodium dodecyl sulfate (SDS)	2326.1	Roth
Sodium azide	8223350100	Merck
Sodium chloride (NaCl)	3957.2	Merck
Sodium dihydrogen phosphate monohydrate ($NaH_2PO_4*1H_2O$)	6346	Merck
Sodium hydroxide (NaOH)	C238798	Merck
Sucrose	S-0389	Sigma-Aldrich
Tetramethylethylenediamine (TEMED)	T9281-50ml	Sigma-Aldrich
Tris(hydroxymethyl)aminomethane (Tris)	4855.2	Roth
Triton®X-100	12298	Merck

2.1.2 Enzymes / antibodies / plasmids / kits / ladder

Description	Order No.	Supplier/manufacturer
Anti-Calcium Channel	C1603	Sigma-Aldrich
Anti-HA High Affinity	11 867 423 001	Roche
Anti-RRAD antibody produced in goat	SAB2502049	Sigma-Aldrich
Collagenase type 1, 41.6 U/ml	-	Worthington Biochemical Corporation
Collagenase type 2, 47.4 U/ml	-	Worthington Biochemical Corporation
Donkey anti-goat IgG-HRP	sc-2020	SantaCruz
Gene Ruler™ 100 bp DNA ladder	SM0241	Thermo Fisher Scientific
HindIII 10 U/µl	ER0501	Thermo Fisher Scientific
KAPA Mouse Genotyping Hot Start Kit	KK7302	PEQLAB Biotechnologie GmbH
NucleoBond® Xtra Maxi Kit	740414.10	Macherey-Nagel
Polyclonal Swine Anti-Rabbit Immunoglobulins/HRP	P0399	Dako
QuantiTect® Reverse Transcription Kit	205311	Qiagen
QuantiTect SYBR® Green PCR Kit	204243	Qiagen
Rad cDNA clone (mouse, pCMv-6-Entry vector, Rrad-Myc-DDK-tagged)	MR204351	Origene Technologies Inc
RNeasy® Fibrous Tissue Mini Kit	74704	Qiagen
RNA ladder 0.5-10 kbp	15623-200	Life Technologies GmbH
SigmaFAST™ Protease Inhibitor Cocktail Tablet, EDTA-Free	S8830	Sigma-Aldrich
Spectra Multicolor Broad Range Protein Ladder	26634	Life Technologies GmbH
Super Signal West Pico Chemiluminescent Substrate	34087	Thermo Fisher Scientific
Trypsin	25300-054	Gibco Thermo Scientific

2.1.3 Consumables

Description	Supplier/manufacturer
Accu-Chek® Aviva Test Strips	Roche Diagnostics Deutschland GmbH
BD Discardit™ II syringes (2, 5, 10, 20, 50 ml; sterile)	Braun
BD Microlance™ 3 injection needles (27G)	Becton Dickinson
BD Plastipak™ 1ml, sterile	Becton Dickinson
Biosphere® filter tips 10, 20, 100 µl	Sarstedt
Borosilicate glass capillaries (1.7 mm OD; 1.133 mm ID, 0.283 mm wall thickness)	Hilgenberg
BRANDplates®pureGrade™, 96-well	BRANDTECH
Buffer solution pH 4, pH 7, pH 9	Roth
Disposable transfer pipettes 3 ml	VWR
Falcon® tissue culture dishes, polystyrene, sterile 35 x 10 mm)	Corning
Falcon tubes (15 and 50 ml)	Sarstedt
GE Healthcare Amersham™ Protran™ Premium NC 200 mm x 4 m (0.45 µm)	Ge Healthcare Biosciences
Immun-Blot® PVDF-Membrane 20 x 20 cm (0.2 µm)	Bio-Rad
Microcentrifuge tubes, 1.7 ml	VWR
Perfusor®-Line	Braun
PCR tubes 0.2 ml	VWR
Roche Light Cycler ® capillaries	Roche
Scalpel No. 22	Pfm medical AG
Serological pipettes (1, 2, 5, 10, 25, 50 ml; sterile)	Sarstedt
Silver wire AG-15W	Science Products GmbH
Sterifix injection filter 0.2 µm	Braun
THOMAPOR® mesh filter, polyamide 250 µm (948362)	THOMAPOR
Ultracentrifuge tubes, 1.5 ml	BECKMAN
Whatman™ 3MM Chromatography Paper 15 cm x 100 m	Ge Healthcare Biosciences

2.1.4 Equipments

Description	Supplier/manufacturer
Accu-Chek® Aviva Blood Glucose Meter System	Roche Diagnostics Deutschland GmbH
Axopatch 200B amplifier	Axon Instruments
BioTek™ Synergy™ 2 Multi-Mode Microplate Reader	Thermo Fisher Scientific
Centrifuge 5425 R	Eppendorf AG
CO_2-incubator HERAcell 150i	Thermo Fisher Scientific
CV 203BU headstage (5285012)	Axon Instruments
Digidata 1440A AC/DA-converter	Axon Instruments
Eppendorf Mastercycler	Eppendorf AG
F423 heated circulating bath	Haake
Faraday cage	Self supplied
Finn pipettes (2, 10, 20, 100, 200, 1000 µl)	Thermo Fisher Scientific
Fluorescence microscope Nikon Eclipse Ti-U	Nikon Instruments
Halogen sold light source KL 1500	Schott
Heating plate RET control IKAMAG	IKA
Heating plate IKA RH basic 2	IKA
Horizon®11-14 Horizontal Gel Electrophoresis System	Thermo Fisher Scientific
Hielscher UP50H Sonicator	Hielscher Ultrasonics GmbH
Langendorff column	Self supplied
Light Cycler®2.0 System	Roche Diagnostics Deutschland GmbH
Light Cycler Carousel Centrifuge	Roche Diagnostics Deutschland GmbH
Microcentrifuge Galaxy MiniStar VWR International	VWR
Micromanipulator MHW-103	Narishige International
Micropipette polisher: type MF-83	Narishige International
Micropump	Ismatec SA
Mini-PROTEAN Tetra Cell (SDS gel casting components and chamber)	Bio-Rad
Mini Trans-Blot® Cell	Bio-Rad
MultiImage® II system	Alpha Innotech

Description	Supplier/manufacturer
Nano Drop 2000c	Thermo Fisher Scientific
Optima™ TLX Ultracentrifuge; rotor: TLA 55	Beckman Coulter Deutschland
Pipetboy acu	Integra Biosciences
Pipette puller P-97	Sutter instruments
Polymax 1040	Heidolph
Potter S	Sartorius
PowerPac™ Universal Power Supply	Bio-Rad
Seven Easy pH-meter	Mettler Toledo
Sterile bench HS 12/2	Heraeus Instruments
Sterilizing oven	Heraeus Instruments
Thermomixer compact	Eppendorf AG
Thermo Shaker and Block	HLC
Tube Roller RS-TR05	Phoenix instruments
Ultra Turrax ®	IKA
Vibration-cushioned table	Self supplied
Vortex Genie2™	Scientific Industries

2.1.5 Computer software / programs

Description	Supplier/manufacturer
AlphaDigiDoc®Pro Imaging System	Alpha Innotech
Clampfit10.2	Axon Instruments
Gen5™ Data Analysis Software	BIOTEK
GraphPad Prism®6	GraphPad Software
ImageJ	National Institutes of Health
Microsoft®Office2007	Microsoft
pClamp10.2	Axon Instruments
Net Primer PREMIER Biosoft	Premier Biosoft
NCBI / Basic Local Alignment Search Tool	NCBI
Primer 3	Whitehead Institute for Biomedical Research
REST-2009©	Qiagen
Roche Assay Design Center	Roche Diagnostics

2.2 Animals

2.2.1 Origin of animals

First breeding animals of the ob/ob mice (leptin B6.Cg-Lep ob/J) were purchased from the Jackson Laboratory, Bar Harbor, USA. First breeding mice lacking the IRS 2 were kindly provided by Prof. Dr. J. Brüning, CECAD Coordinator, University Hospital of Cologne (former: Institute for Genetics, University of Cologne). First Rad-k.o. animals were kindly provided by D. A. Andres, Ph.D. Professor and Chair, Department of Molecular & Cellular Biochemistry, University of Kentucky, College of Medicine, Lexington, USA. This was in agreement with Prof. Dr. C. R. Kahn, Chief Academic Officer, Joslin Diabetes Center/Professor of Medicine, Harvard Medical School, Boston, USA. Furthermore a cross-breeding was established to raise ob/ob x Rad-k.o. mice. All mouse lines had a C57BL/6J background. Age-matched wt mice (homozygous C57BL/6J mice of all breedings) were used as controls.

2.2.2 Breeding and maintenance

Animals were raised and maintained in an in-house animal facility of the Center of Pharmacology, Institute II, University Hospital of Cologne. Rad-k.o. mice were also raised in the Center for Molecular Medicine Cologne (CMMC), University Hospital of Cologne. All mice were kept in ventilated cages with food and water ad libitum, maintained in a 12h/12h dark/light cycle. All animals were fed with ssniff® complete diets (mouse maintenance: V1534-703, mouse breeding: V1124-703, ssniff Spezialitäten GmbH, Soest, Germany). Heterozygous (hz) ob/+ animals were necessary to breed ob/ob mice, whereas IRS 2-k.o. and Rad-k.o. mice could also be generated using homozygous knockouts. Animal breeding, maintenance and experiments were approved by the responsible federal state authority (Landesamt fuer Natur-, Umwelt- und Verbraucherschutz North Rhine-Westphalia; reference: 84-02.05.20.12.294/84-02.05.20.13.060). All animal experiments were in accordance with the guidelines from directive 2010/63/EU of the European Parliament on the protection of animals used for scientific purposes.

2.2.3 Determination of blood glucose, body weights and ventricle weights

Body weights were determined immediately before killing the mice. Blood glucose concentration was measured shortly after cervical dislocation using a blood glucose meter (Accu-Check® Aviva, Roche Diagnostics Deutschland GmbH, Mannheim, Germany) with a drop of blood leaking from the excised tail (approx. 2 mm). For determination of ventricular heart weight hearts were excised immediately, atria and aorta were dissected and intraventricular blood removed. An increased ventricle-to-body weight ratio is a common indicator for cardiac hypertrophy.

2.2.4 Sample preparation

After cervical dislocation murine hearts were dissected in ice-cold PBS. For Western Blot and quantitative real-time PCR (qRT-PCR) ventricles were quick-frozen in liquid nitrogen and stored at -80°C until further processing.

2.3 Genotyping

For genotyping tail-tips (approx. 4 mm) from three week old mice were cut and stored at -20°C until further processing. Genotyping PCRs were kindly performed by S. Kirchmann-Hecht at the Center of Pharmacology, Institute II, University Hospital of Cologne.

2.3.1 Genomic deoxyribonucleic acid (gDNA) purification

For gDNA purification KAPA Express Extract system, included in the KAPA Mouse Genotyping Hot Start Kit (PEQLAB Biotechnologie GmbH, Erlangen, Germany), was used according to the manufacturer's protocol. gDNA extracts were stored at -20°C.

2.3.2 Polymerase chain reaction (PCR)

Polymerase chain reaction allows amplification of DNA fragments of specific gDNA regions in order to analyze and identify these regions. gDNA was amplified with the KAPA2G Fast Hot Start Genotyping Mix with dye, the second KAPA Mouse Genotyping Hot Start Kit component. KAPA2G Fast Hot Start Genotyping Mix (2 x) is a ready-to-use master mix and contains a Hot Start DNA polymerase, a buffer, dNTPs (0.2 mM each at 1 x), $MgCl_2$ (1.5 mM at 1 x), stabilizers and two inert dyes, which allow a direct PCR analysis of reaction products without use of an additional loading solution. Only primers and templates had to be added. Reaction setup, cycling parameters and primers can be found in table 2.1 - 2.3.

Table 2.1 DNA amplification protocol for genotyping: reaction setup

Components	**IRS2-k.o.**	**ob/ob**	**Rad-k.o.**	**Final concentration**
PCR grade H_2O	7.75 µl	8 µl	9.5 µl	
KAPA2G Fast Hot Start Genotyping Mix 2 x	12.5 µl	12.5 µl	12.5 µl	1 x
Primer	1.25 µl / primer	1.25 µl / primer	0.5 µl / primer	0.5 µM
Template gDNA	1 µl	2 µl	1 µl	

Table 2.2 DNA amplification protocol for genotyping: cycling parameters

Cycling step	**Target temperature / incubation time**			**No. of cycles**
	IRS2-k.o.	**ob/ob**	**Rad-k.o.**	
Initial denaturation	95°C / 3 min	95°C / 3 min	94°C / 3 min	1
Denaturation	95°C / 15 sec	95°C / 15 sec	94°C / 30 sec	35
Annealing	61°C / 15 sec	60°C / 15 sec	57°C / 30 sec	
Elongation	72°C / 20 sec	72°C / 20 sec	72°C / 40 sec	
Final elongation	72°C / 5 min	72°C / 10 min	72°C / 5 min	1

Table 2.3 Primer pairs for genotyping (Sigma-Aldrich, St. Louis, MO, USA). Rad and IRS primers were described previously (Chang et al., 2007, Kido et al., 2000). Ob/ob primers were designed using the freeware Primer 3 (Whitehead Institute for Biomedical Research, Cambridge, MA, USA).

Primer name	Sequence (5'-3')
IRS 2 forward (F) primer 10 µM	GAA GAC AGT GCG TAC ATG CGA ATG
IRS 2 reverse (R) primer 10 µM	CCT CAT GGA GGA AAG CAC TGC TG
IRS 2 neosense primer 10 µM	TTC TAT CGC CTT CTT GAC GAG TTC
Ob/ob F primer 10 µM	TGT CCA AGA TGG ACC AGA CTC
Ob/ob R primer 10 µM	ATC CAG GCT CTC TGG DTT CT
Rad F mutant primer 25 µM	GAG CAC GTA CTC GGA TGG AAG C
Rad R mutant primer 25 µM	GCG ATA GAA GGC GAT GCG CTG C
Rad F wildtype primer 25 µM	AGT CTG AAC AGG GGT CTA CGA GTG
Rad R wildtype primer 25 µM	TCT GGC CCT GTG TCC GAG TTC

2.3.3 Restriction enzyme digestion / gel electrophoresis

Ob/ob mice genotyping products were subjected to a restriction enzyme digestion with HindIII (10 U/µL, ER0501, Thermo Fisher Scientific) for 1 h at 37°C (table 2.4), followed by 20 min at 60°C, before loading on a 3% agarose gel placed into a gel electrophoresis chamber containing TBE buffer (table 2.5).

Table 2.4 Restriction enzyme digestion of ob/ob PCR products

Components	Final volume
PCR grade H_2O	7 µl
10 x BufferR (supplied with HindIII)	2 µl
HindIII (10 U/µL)	1 µl
PCR product	10 µl

Table 2.5 Electrophoresis buffer for PCR products

TBE buffer	Final concentration
Tris	89 mM
Boric acid	89 mM
EDTA	2 mM
pH 7.6	

PCR products generated for genotyping of IRS 2-k.o. and Rad-k.o. mice were directly loaded on a 2% agarose gel. During electrophoresis for 1 h at 100 mA PCR products migrated towards the anode, small fragments showing slower migration rates than bigger fragments. To facilitate detection the double-stranded DNA intercalating dye ethidium bromide was added. For visualization AlphaDigiDoc®Pro Imaging System (Alpha Innotech, Santa Clara, CA, USA) and a 100 bp or 1 kbp DNA ladder (GeneRuler 100 bp DNA Ladder, SM0241 / GeneRuler 1 kbp DNA Ladder, SM0311, Thermo Fisher Scientific) were used. Table 2.6 shows the expected band sizes of PCR products.

Table 2.6 Expected band sizes of PCR products

Expected band size	Wildtype	Mutant
IRS 2	300 bp	400 bp
Ob/ob	180 bp	83 bp and 99 bp
Rad	507 bp	347 bp

2.4 Cardiac myocytes isolation assay

The isolated perfused mammalian heart preparation, widely known as the Langendorff perfused heart, was established in the late 19th century by Oscar Langendorff. The method was developed on the basis of the isolated perfused frog heart and originally used for the study of heart physiology (Langendorff, 1895, Taegtmeyer, 1995, Zimmer, 1998). The animal's heart is removed from its body and retrograde perfused via the aorta in order to keep it alive for several hours. This preparation method has been subjected to various modifications. For instance, the method has been modified in order to isolate cardiac myocytes. The aorta is cannulated as well, but retrograde perfused with an enzyme solution to digest the heart into individual cells.

In this study single ventricular myocytes were isolated by using a modification of a method described previously (Heubach et al., 1999, Foerster et al., 2003). Isolated cells were subjected to patch-clamp analysis and cardiac myocytes purification assays. In detail, solution A (table 2.7) was prepared as stock solution in tenfold concentration and stored at 4°C until use. On each experimental day glucose was added freshly to solution A and diluted 1:10 with aqua destillata. The pH was adjusted to 7.4 with NaOH. To obtain solution B (table 2.7), 500 mg BSA was added to 500 ml of solution A. The perfusion column and organ bath (figure 2.1) were filled with solution B, preheated to

37°C using a water bath and perfused with oxygen 100%. The length of the column defined the perfusion pressure. Circa 30 minutes prior to cervical dislocation mice were treated with heparin (7.5 IU/g, intra peritoneal) to prevent post-mortem thrombus formation. Preparation and cannulation of the aorta followed immediately after cervical dislocation in ice-cold solution A. The aorta was placed over the tip of a blunt injection needle and tied with a binder yarn before being connected to the column (figure 2.1). Then the whole heart was perfused with solution B for 5 min in order to remove the blood from the coronary arteries. Afterwards the heart was perfused under constant pressure with an enzyme solution prepared in solution B (solution C, table 2.7). Duration of digestion depended on the amount of solution passing the coronary arteries estimated by the drop rate. After 5 min of digestion drop rate was determined first and subsequently in an one-minute distance. End point of digestion was reached when drop rate was doubled or after a maximum perfusion time of 15 min or when the outward appearance of the heart (e.g. paleness, slightly edematous tissue) indicated sufficient perfusion. To obtain numerous healthy cardiomyocytes the heart had to be light-colored, soft and flaccid when palpated after perfusion. The digested heart was taken quickly from the cannula, aorta and atria were removed and ventricles were cut into small pieces in solution B. The tissue pieces were gently triturated with a cut-off plastic transfer pipette for about 5 min to gain individual cells. Cells were filtered through a 250 µm mesh cell collector into a falcon tube and left for 20 min at room temperature to settle. Ca^{2+} concentration was increased (from 0 µM to 100 µM to 200 µM to 400 µM) every 20 min to select Ca^{2+} tolerant cells which were rod-shaped and quiescent. Cells were maintained at room temperature and taken for patch-clamp analysis for up to 6 h.

Table 2.7 Solutions for cardiac myocytes isolation

Solution A	**Final concentration**
NaCl	133 mM
KCl	4 mM
NaH_2PO_4 * 1 H_2O	1.2 mM
$MgSO_4$ * 7 H_2O	1.2 mM
HEPES	10 mM
Glucose	12.1 mM
In H_2O, pH 7.4 with NaOH	

Solution B	**Final concentration**
BSA	1 mg/ml
In solution A	

Solution C	**Final concentration**
Collagenase type 1	41.6 U/ml
Collagenase type 2	47.4 U/ml
$CaCl_2$-solution 0.1 M	25 µM
In solution B	

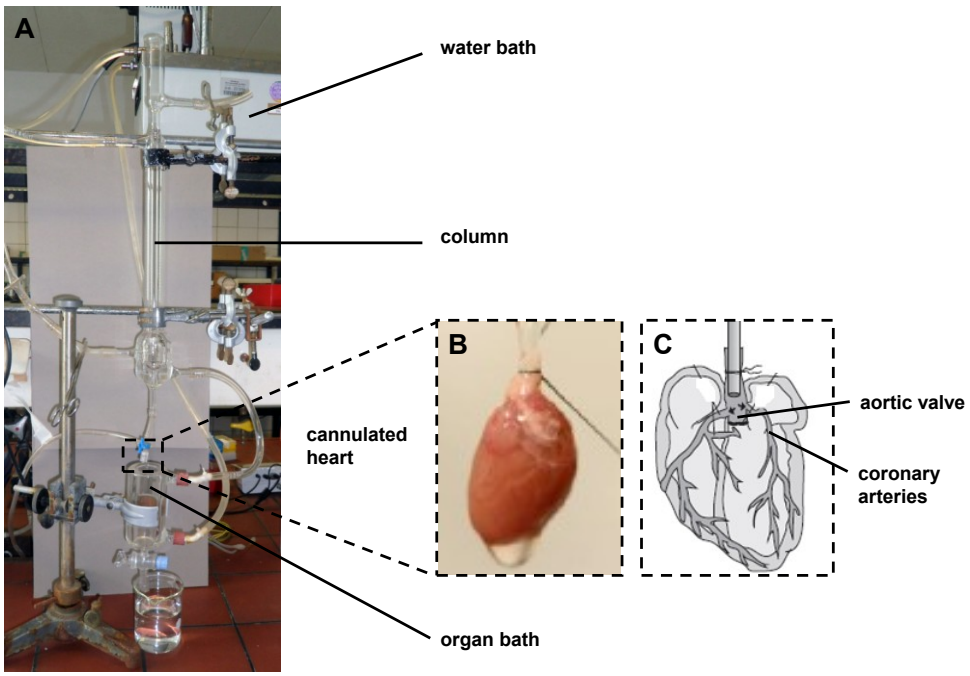

Figure 2.1 **Cardiac myocytes isolation system:** (A) setup; (B) exemplary cannulated heart; (C) visualization of a proper cannulated heart (heart figures modified from Louch et al., 2011).

2.5 Cardiac myocytes purification assay / Percoll density gradient centrifugation

Equilibrium density gradient centrifugation is used for purifying cell fractions (Lodish et al., 2007). In this study it was planned to separate the enzymatically isolated cardiomyocytes prior to perform quantitative real-time PCR (qRT-PCR) experiments.
Percoll (GE Healthcare, Solingen, Germany) is a commercially available medium for that purpose. It is composed of colloidal silica coated with nondialyzable polyvinylpyrrolidone. The density range of Percoll medium/gradient encompasses all densities of the sample particles. Each particle sediments to its isopycnic position where its density is equal to the surrounding gradient density. Particle size is not relevant given that the density of the particles is always smaller than medium density. Thus sample particles are separated only on the basis of differences in density. The gentle centrifugation conditions allow separation of cells without loss of viability and morphological integrity.
For Percoll density centrifugation a Percoll stock solution was prepared by adding 40.5 ml of Percoll to 4.5 ml ADS buffer 10 x (table 2.8). Out of this stock solution two Percoll solutions with different densities were diluted in ADS buffer 1 x. In a 15 ml falcon tube a layer consisting of a 4 ml 40.5% Percoll solution was layered over a 3 ml 58.5% Percoll layer. For better visualization phenol red was added to the bottom layer. After Langendorff isolation of cardiac myocytes cell suspension obtained was centrifuged at 330 g for 3 min. The pellet was resuspended in 2 ml ADS buffer 1 x. Subsequently, the cell suspension was added to the gradient and centrifuged at 1850 g for 30 min (room temperature). Four fractions of cells were obtained: cells on the top of 40.5% Percoll (fraction 1), cells within the 40.5% Percoll (fraction 2), a layer of cells at the interface of the two layers of Percoll (fraction 3) and cells within the 58.5% Percoll layer (fraction 4). Purified cardiac myocytes, which should concentrate at fraction 3, could be objected to further experiments, e.g. qRT-PCR.

Table 2.8 Solutions for Percoll density gravity centrifugation

ADS buffer (10 x)	**Final concentration**
NaCl	129 mM
HEPES	22 mM
NaH_2PO_4 * 1 H_2O	1 mM
Glucose	6.2 mM
KCl	6 mM
$MgSO_4$ * 7 H_2O	0.45 mM
In H_2O, pH 7.4 with NaOH, sterile filtered	

2.6 Messenger ribonucleic acid (mRNA) analysis of murine ventricle samples

For gene analysis on transcriptional level mRNA was isolated from murine ventricles, reverse transcribed into cDNA and quantified via qRT-PCR. In a qRT-PCR the amplification of cDNA via PCR and the detection of amplification products occur simultaneously.

2.6.1 Primer design and efficiency tests

Specific primer pairs for the Ca_vα1-subunit of the L-type calcium channel Ca_v1.2 (gene ID: Cacna1c), the auxiliary beta-subunits Ca_vß1, Ca_vß2, Ca_vß3 (gene ID: Cacnb1-Cacnb3) and the housekeeping genes S 29 (ribosomal protein S 29, gene ID: Rps 29), HPRT (Hypoxanthine-guanine phosphoribosyltransferase) and GAPDH (Glyceraldehyde 3-phosphate dehydrogenase) were described previously in other publications or in the following dissertations of our own group: Böhnke, 2012; Dizayee, 2011; Fabisch, 2010. Primers for the RGK proteins Rad (gene ID: Rrad), Gem, Rem 1, Rem 2 were designed using the software tool Roche Assay Design Center (Roche Diagnostics), the freeware Primer 3 (Whitehead Institute for Biomedical Research, Cambridge, MA, USA) or taken from earlier publications, as well (table 2.9). To avoid detecting genomic DNA, primers were designed intron-spanning or intron-flanking. Primers were validated for specificity, hairpins and dimers utilizing the freeware NCBI/Basic Local Alignment Search Tool (NCBI, Bethesda, Maryland, USA) and NetPrimer PREMIER Biosoft (PREMIER Biosoft, Palo Alto, California).
Before starting the experiments, primers (Sigma-Aldrich, table 2.9) were tested for

amplification efficiencies, as well. Efficiencies of two genes were compared by preparing a dilution series for both genes from a murine ventricle cDNA sample. The threshold cycle (Ct) values obtained by qRT-PCR were blotted against the log template amount. Resulting slopes were taken to calculate PCR efficiency:

$$\text{Efficiency [\%]} = 10^{(-1/\text{slope})} - 1 \times 100$$

If efficiencies are comparable, the blotted curves of both genes go in parallel (Bustin et al., 2009). The differences in Ct values of the target and the reference gene will be constant independent of template amount (figure 2.2).

Table 2.9 qRT-PCR primers (100 µM). Primers were diluted 1:10 before pipetting to the master mix. Final concentration used: 0.75 µM. Forward and reverse primers are marked with F and R.

Primer	**Sequence (5'-3')**	**Source**
S29 (F)	ATG GGT CAC CAG CAG CTCT A	(Böhnke, 2012, Fabisch, 2010)
S29 (R)	AGC CTA TGT CCT TCG CGT ACT	
HPRT (F)	TGA CAC TGG CAA AAC AAT GCA	(Fabisch, 2010)
HPRT (R)	GGT CCT TTT CAC CAG CAA GCT	
GAPDH (F)	CAT GGC CTT CCG TGT TCC TA	(Bai et al., 2013)
GAPDH (R)	CCT GCT TCA CCA CCT TCT TGA T	
$Ca_v1.2$ (F)	TCC GAA CAT TAC AAC CAG CCT	(Fabisch, 2010, Böhnke, 2012, Dizayee, 2011)
$Ca_v1.2$ (R)	GCT GTA CAT CTT CAG GAG CA	
Rad (F)	AAG ACG GAC CTG AAG CAG AA	Roche Assay design center
Rad (R)	CAT CCT GTT CCC AAA TGT CA	
Rem 1 (F)	AAAC AAG ACC GAG ACC CTC A	Roche Assay design center
Rem 1 (R)	CAC TGA CAG CGT TCT CTC GT	
Rem 2 (F)	AGC ACT TTG TTC TTC CAG CA	Primer 3
Rem 2 (R)	CAG TTT CTC TGG CTT CTG TTT C	
Gem (F)	GAC AGC ATG GAC AGC GAC T	Roche Assay design center
Gem (R)	ACG ACC AGG GTA CGC TCA TA	
$Ca_vß1$ (F)	TGG ACA GCC TTC GTC TGC T	(Dizayee, 2011)
$Ca_vß1$ (R)	TGG AAC TGG AGT TGT CAC CT	

Primer	Sequence (5'-3')	Source
Ca_vß2 (F)	GGG AGG CAG TAC GTA GAG AAG CT	(Böhnke, 2012, Dizayee, 2011)
Ca_vß2 (R)	TGC AAA TGC AAC AGG TTT TGT C	
Ca_vß3 (F)	TGG AGT CAA CTT TGA GGC CA	(Dizayee, 2011, Böhnke, 2012)
Ca_vß3 (R)	TCC CGA TCC ACC AGT CAT TG	

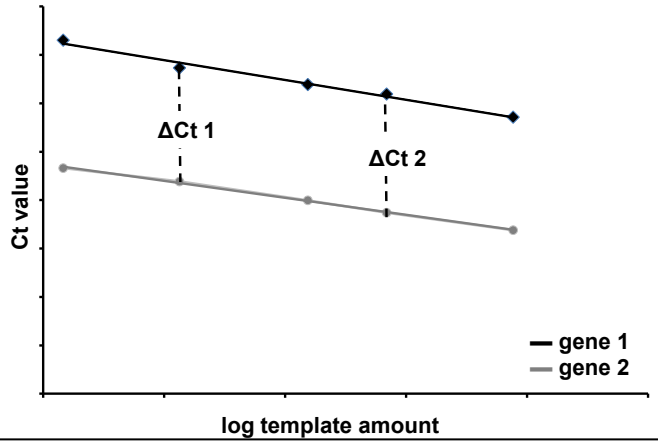

Figure 2.2 **Determination of primer efficiencies:** if efficiencies of two genes are comparable, the blotted curves of both genes go in parallel and the differences in Ct values (ΔCt) will be constant independent of template amount (ΔCt1 = ΔCt2). Resulting slopes of the blotted dilution series are necessary to calculate PCR efficiencies.

2.6.2 Isolation of mRNA

Isolation of mRNA from murine ventricle was performed with the RNeasy® Fibrous Tissue Mini Kit (QIAGEN, Hilden, Germany) according to the manufacturer's protocol with the following modifications: approx. 30 mg of frozen cardiac apex was homogenized with an Ultra Turrax ® (IKA, Staufen, Germany) in 300 µl buffer RLT. On-column DNase digestion was skipped due to the following gDNA elimination step during reverse transcription. Each step of the protocol was performed at room temperature. The RNA was eluted in a volume of 60 µl RNase-free water and stored at -80°C.

2.6.3 Determination of mRNA quality

Quality and quantity of the purified mRNA were controlled using the Nano Drop 2000c UV-Vis Spectrophotometer (Thermo Fisher Scientific).

An additional quality check followed via agarose gel electrophoresis. Ribosomal RNA (rRNA) was separated into 18 S rRNA (~ 1.9 kbp) and 28 S rRNA (~ 4.7 kbp). RNA quality was marked by two sharp bands of which the 28 S rRNA band was twice as intense as the 18 S rRNA band (Taylor et al., 2010).

Check of RNA integrity was performed as described earlier (Gründemann and Koepsell, 1994). For short, RNA samples and RNA ladder were mixed with three sample volumes of 4/3 DLG denaturating solution (table 2.10) and incubated for 1 h at 50°C. Main components of the 4/3 DLG are DMSO and deionized glyoxal. Glyoxal reacts with the base guanin and prevents base-pairing with cytosin. Consequently, the so-called glyoxilation of the single-stranded RNA avoids formation of secondary structures. After incubation 1 µl Orange G loading dye was added to 4 µl of denaturated sample solution and RNA ladder, respectively. Subsequently, samples were loaded on a 1% agarose gel (0.5 mM iodoacetic acid sodium salt included) in BES buffer, that was run at 90 mV. Iodoacetic acid sodium salt, an alkylating agent, was used to protect the RNA against RNases. BES buffer is a low-ionic strength buffer, which also prevents base pairing. After approx. five minutes the buffer was circulated constantly using a mini pump to avoid the development of a pH gradient. For visualization ethidium bromide staining and detection via AlphaDigiDoc®Pro Imaging System (Alpha Innotech) were used. Ethidium bromide staining of RNA was reported to react with glyoxal, resulting in a loss of fluorescence (Gründemann and Koepsell, 1994). Therefore the dye was always added freshly to the 4/3 DLG denaturating solution.

Table 2.10 Solutions for RNA integrity check

BES buffer (1 x)	**Final concentration**
BES	10 mM
EDTA	0.1 mM
pH 6.7; treated with DEPC-H_2O	

4/3 DLG	**Final concentration**
DMSO	50 % (v/v)
Deionized glyoxal (40 %)	1 M
In BES buffer (1 x)	

4/3 DLG denaturating solution	**Final volume**
4/3 DLG	50 µl
Ethidium bromide solution (0.25 %)	1 µl

RNA ladder	**Final volume**
RNA ladder 1 µg/µl; 0.5-10 kb	10 µl
DEPC-H_2O	10 µl
4/3 DLG denaturating solution	60 µl

Orange G loading dye	**Final concentration**
Glycerol	50 % (v/v)
DEPC-H_2O	50 % (v/v)
Orange G	2.5 mg/ml

2.6.4 Reverse transcription into complementary DNA (cDNA)

The reverse transcription step was carried out in duplicate with the QuantiTect® Reverse Transcription Kit (Qiagen), as outlined in the manufacturer's protocol. In brief, 400 ng total RNA was used in a final volume of 20 µl. Samples were prepared on ice. Reverse transcription was performed in a mastercycler (Eppendorf AG, Hamburg, Germany) using following conditions:

5 min at 42°C for genomic DNA elimination
19 min at 42°C for reverse transcription
3 min at 95°C to inactivate reverse transcriptase

cDNA was stored at -20°C.

2.6.5 Quantitative real-time PCR (qRT-PCR)

qRT-PCR was performed to quantify mRNA. This method possesses high sensibility for the detection of low target amounts (Bustin, 2000) and facilitates detection in the early exponential phase of PCR “in real time” during each PCR cycle. Real-time PCR reactions were carried out in a thermo cycler that permits fluorescence-based detection technologies. In this study the dye SYBR Green that fluoresces upon binding to double-stranded DNA was used for quantifying.

In qRT-PCR a starting amount of cDNA is amplified in a distinct number of cycles, consisting of denaturation, primer annealing and template elongation. Proportional to the amount of PCR product generated in each extension cycle, the fluorescence increases. In early cycles, there is no detectable fluorescence increase due to PCR products; this nonspecific signal is defined as background. The so-called threshold level is set above background and within the detectable log-linear phase of the reaction. Once there is a significant increase in fluorescence, so that the amplification plot crosses the threshold, the corresponding cycle is registered as the so-called threshold cycle (Ct) value. Respectively, the intensity of fluorescence generated at a given cycle is indicative of the template amount (figure 2.3).

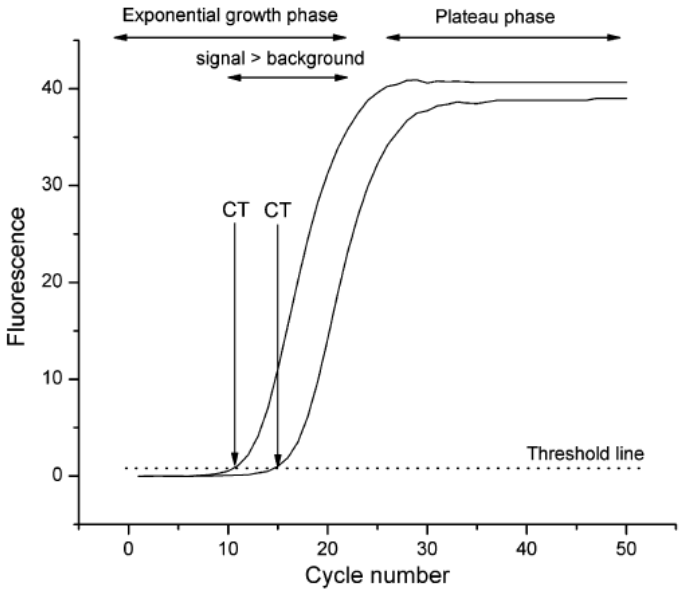

Figure 2.3 **A typical qRT-PCR amplification plot:** the increase in fluorescence is blotted versus the cycle number. A threshold level is set sufficiently above background within the exponential growth phase and the number of cycles required to reach threshold, Ct, is registered (modified from Kubista et al., 2006).

qRT-PCR was carried out in the Light Cycler®2.0 System (Roche Diagnostics Deutschland GmbH). Experiments were performed in triplicates using the QuantiTect SYBR® Green PCR Kit (Qiagen). Master mix solution (table 2.11) and primer pair dilutions (1:10 each) were prepared on ice. After pipetting the master mix into a Light Cycler® glass capillary, 1.5 µl per forward and reverse primer (0.75 µM final concentration per primer) were added. Before starting the thermo cycler (Light Cycler®2.0 System, Roche Diagnostics Deutschland GmbH), glass capillaries were spun down using the LightCycler® carousel centrifuge.

After preincubation and 45 cycles of amplification (each consisting of denaturation, annealing and elongation), melting curve analysis was performed to check for product purity and to exclude primer dimers (table 2.12). Each experiment contained a control reaction in which no reverse transcriptase was added (detection of DNA contamination) and a further control with missing template (detection of general contamination).

Table 2.11 Composition of reaction mix

Master mix solution (per target / primer pair)	**Volume**
QuantiTect SYBR® Green PCR Master mix (2 x)	10 µl
cDNA template	1 µl
RNase-free water	6 µl

Table 2.12 qRT-PCR protocol

Cycling step	**Target temperature**	**Incubation time**	**Temperature transition rate**	**No. of cycles**
Preincubation	95°C	15 min	20°C / sec	1
Denaturation	94°C	15 sec	20°C / sec	45
Annealing	58°C	25 sec	20°C / sec	
Elongation	72°C	10 sec	20°C / sec	
Melting curve analysis	64°C	1 min	20°C / sec	1
Inactivation of polymerase	95°C			1

After qRT-PCR random samples were checked for correct cDNA amplification on a 1.3% agarose gel (electrophoresis in TAE buffer 1 x at 100 V and detection via ethidium bromide; table 2.13).

Table 2.13 Electrophoresis buffer for qRT-PCR products

TAE buffer	Final concentration
Tris pH 7.6	40 mM
Acetic acid	20 mM
EDTA	1 mM

2.6.6 qRT-PCR: data analysis

At the beginning of data analysis the expression of S 29, HPRT and GAPDH was compared in order to find appropriate housekeeping genes. In general, housekeeping genes should be stably expressed. Their mRNA amounts should correlate with the total amounts of mRNA present in the samples (Bustin et al., 2009).

The Pfaffl method (REST-2009©)

For relative quantification of mRNA expression levels the Pfaffl method was used, available as the relative expression software tool REST-2009© (Qiagen, Hilden, Germany; see also Pfaffl et al., 2002). This method was chosen because it takes into account different primer efficiencies as well as several reference genes in order to correct the quantification ratio. In the present study data were normalized to S29, GAPDH and HPRT simultaneously (see also appendix, chapter 8.5.4). The software tool compares two groups (e.g. wildtype vs. mutant) with up to 16 data points per group and calculates the relative expression ratio between them. REST-2009© subsequently tests the group differences for significance. The statistical test used is based on the Pair Wise Fixed Reallocation Randomization Test©. A randomization test makes no assumptions about distributions and is only based on the fact that samples are randomly allocated. The randomization test repeatedly and randomly reallocates (2000 times) the observed Ct values for the housekeeping and the target genes to the Ct values for control and mutant groups, and notes the apparent expression ratio each time. Because it is impractical to test for all possible allocations of data to the two

groups, only random samples are tested. If 2000 random reallocations are taken for analysis, the software tool gives a good estimate of the p-value < 0.05. REST-2009© analysis provides a 95% confidence interval for the expression levels as well as Whisker box plots for a visual representation of variation for each gene (Pfaffl et al., 2002).

In the current study data were also analyzed via $2^{-\Delta\Delta Ct}$ analysis in order to provide a commonly accepted visual representation of variation for each gene via bar graphs (inclusive error bars).

The $2^{-\Delta\Delta Ct}$ or comparative method

The $2^{-\Delta\Delta Ct}$ or comparative method can be also used for relative quantification of a single transcription difference between two groups (Livak and Schmittgen, 2001). This method is based on two assumptions: first, the reaction is occurring with 100% efficiency and second, DNA amplification is constant among the samples (VanGuilder et al., 2008). The $2^{-\Delta\Delta Ct}$ method only allows normalization against a single gene and primer efficiency cannot be included into analysis. In the present study S 29 was used as normalization gene (see also appendix, chapter 8.5.4).

For relative quantification, the difference between the Ct values of the target gene and the housekeeping gene was calculated first:

Δ Ct = Ct (target gene) - Ct (housekeeping gene)

Then, Δ Ct was used to compare gene expression in different samples, e.g. mutant vs. wildtype:

$\Delta\Delta$ Ct = Δ Ct (mutant) – Δ Ct (wildtype)

An altered gene expression in mutant mice compared to wildtype mice was calculated as follows: $2^{-\Delta\Delta Ct}$.

A $2^{-\Delta\Delta Ct}$ value of 1 means no expression change, 2 stands for a twofold upregulation and 0.5 for a twofold downregulation of expression. In the present study significant expression changes of the $2^{-\Delta\Delta Ct}$ analysis are supplemented in the appendix.

2.7 Protein analysis of murine ventricle samples

2.7.1 Positive controls for $Ca_v1.2$ protein and Rad protein

$Ca_v1.2$ protein

A positive control for $Ca_v1.2$ protein was generated via a calcium phosphate based transfection method in tsa201 cells (human embryonal kidney cells; kindly provided by A. Koschak, LFU Innsbruck, Austria), followed by cell lysis and Co-immunoprecipitation (Co-IP).

Calcium phosphate transfection: transfection was kindly performed by C. Fried at the Center of Pharmacology, Institute II, University Hospital of Cologne. Before being transfected the tsa201 cells were split in DMEM-high glucose medium (Gibco, Thermo Scientific), supplemented with 10% FCS (Biochrom, Berlin, Germany) and Penicillin/Streptomycin (50 U/ml / 50 µg/ml; PAA Laboratories GmbH, Cölbe, Germany). At the time of transfection attached cells were about 30-40% confluent. The desired plasmid DNA was first bound on the surface of a calcium phosphate precipitate. This precipitate was built up by mixing HBS buffer (table 2.14), containing phosphate ions, and a calcium chloride solution.

In brief, the ice-cold transfection mix contained 950 µl HBS buffer and approx. 20 µg of the following plasmid DNA sequences in a subunit molar ratio of 1:1:1 (inserted in pcDNA3 expression vectors): CACNA1c (rat), CACNA2D1 (human) and CACNB3 (human). The CACNA1c plasmid was kindly provided by E. Bourinet, Institute for Functional Genomics, Montpellier, France (GenBank^{TM} accession number M67515; (Altier et al., 2002)). Into the extracellular S5-H5 loop of domain II of the $Ca_v1.2$ construct a hemagglutinin epitope was inserted. The other plasmids were necessary to improve transfection efficiency. After preparation of the transfection mix 50 µl ice-cold $CaCl_2$ solution (2.5 M) was added dropwise and vortexed briefly. Subsequently, the CaP-DNA complex was able to built up in about 30 min of incubation at room temperature. Thereafter, the suspension was transferred dropwise to the cells to be transfected. Given that an excess of Ca^{2+} may be toxic for the cells, they were washed twice in PBS (37°C) after 5 hours of incubation at 37 °C and fresh medium was added. The next morning medium was changed again (Penicillin/Streptomycin included), but instead of 10% only 2% FCS were added. After cells reached 60-70% confluence, they were incubated at 28°C for 72 h for protein expression.

Table 2.14 Composition of HBS buffer

HBS buffer	**Final concentration**
HEPES	21 mM
NaCl	137 mM
KCl	49 mM
Dextrose / glucose	5.5 mM
$Na_2HPO_4*7H_2O$	0.75 mM
pH 6.95 - 7.1 with NaOH	

Cell lysis: transfected cell dishes were set back to 37°C incubation temperature for approx. 6 h in order to achieve a better cell attachment. 100% confluent cell dishes were put on ice for 15 min to prevent endocytosis and protein degradation. Following steps were performed on ice or at 4°C: cells were washed twice in 5 ml PBS. Afterwards medium was removed and 4 ml PBS added (including 10% SigmaFAST™ Protease Inhibitor Cocktail, EDTA-Free, Sigma-Aldrich). Cells were scraped off, transferred to microcentrifuge tubes and centrifuged at 3500 rpm for 3 min. Subsequently, the pellet was resuspended in 750 µl lysis buffer (table 2.15) and incubated at 700 rpm for 45 min. Samples were sonicated (60% pulse, 3 x 3 sec) in order to fragment DNA and to remove membrane components of the calcium channel, followed by another 30 min of incubation. To pellet non dissolved cell debris the tube was centrifuged at 13000 rpm for 15 min.

Table 2.15 Composition of cell lysis buffer

Cell lysis buffer	**Final concentration**
Tris	50 mM
NaCl	100 mM
Triton®X-100	0.2 % (v/v)
Nonidet®P40 BioChemica	0.2 % (v/v)
EDTA	10 mM
SigmaFAST™ Protease Inhibitor Cocktail, EDTA-Free	10 % (v/v)
pH 7.5	

CoIP: the supernatant obtained after cell lysis was objected to a CoIP in order to concentrate the antigen $Ca_v1.2$. In brief, 1.5 ml of the supernatant and 10 µl Anti-HA High Affinity antibody (Roche Diagnostics GmbH Deutschland) were incubated for 5 h at 4°C to form an immune complex. Pierce®Protein A/G Magnetic Beads (Thermo Fisher Scientific) were washed twice in 1000 µl lysis buffer. The beads contained a recombinant Protein A/G that combined the IgG binding domains of Protein A and Protein G. The immune complex was then added to 25 µl of the washed beads and incubated over night (4°C). Thereby the complex was immobilized to the beads. The next day supernatant was discarded, beads were collected with a magnet and washed twice in 1 ml ice-cold PBS-Triton 0.2% for about 5 min. Finally, beads were incubated in 40 µl 2 x Laemmli buffer (table 2.16) for 10 min at 50°C. After centrifugation at full speed for 1 min at 4°C eluted samples were shock frozen in liquid nitrogen and stored at -20°C. 5 µl of the solution were used for Western Blot.

Table 2.16 Composition of Laemmli buffer

Laemmli buffer (4 x)	**Final concentration**
Tris-HCl	200 mM
SDS	8 % [w/v]
Glycerol	40 % [v/v]
Bromphenol blue	0.1 % [w/v]
pH 6.8	

Rad protein

In order to obtain enough transfectable plasmid DNA, a mouse cDNA clone (pCMv-6-Entry vector, Rrad-Myc-DDK-tagged, MR204351, Origene Technologies Inc, Rockville, MD, USA) was purified by NucleoBond® Xtra Maxi Kit (Macherey Nagel, Dueren, Germany) according to the manufacturer's protocol and the sequence was verified via sanger sequencing.

Ca^{2+} phosphate transfection and cell lysis were performed as described above (transfection of $Ca_v1.2$) with following modifications: first, 20 µg of murine rRad (pCMv-6 vector) were added to 950 µl ice-cold HBS buffer. Secondly, instead of 750 µl lysis buffer 150 µl were added to the cell pellet. Without sonification cells were lysed for 1 h at 4°C and centrifuged at full speed for 1 min at 4°C. The supernatant obtained after centrifugation could be directly used for Western Blot. CoIP was not necessary.

2.7.2 Cardiac cell membrane protein preparation assay

The LTCC is an integral cell membrane protein complex (Hofmann et al., 2014). Therefore the transmembrane protein content was a particular research interest. Consequently, the protein preparation assay used was optimized to isolate mainly membrane proteins. The protocol was a modified protocol kindly provided by Prof. Dr. V. Flockerzi, Experimental and Clinical Pharmacology and Toxicology, Saarland University, Homburg, Germany (personal communication).

For short, a frozen heart was disrupted with an Ultra Turrax® in 1 ml homogenization buffer (table 2.17) and then frozen at -80°C for at least 20 min. The formation of crystals during the freezing step should break up tight cell structures. Following steps were performed on ice or at 4°C: in order to dissolve the membrane proteins, the thawed suspension was homogenized with a Potter S homogenizer (Sartorius, Goettingen, Germany) and sheared twice through an injection needle (0.7 mm / 22 G). Fractioning procedure was conducted with differential centrifugation at increasingly higher speeds (Lodish et al., 2007). In general, large heavy dense particles sediment faster than small low dense particles. The dense, nonionic substance sucrose was optimal to achieve a good separation. Thus, 0.5 ml of a 0.63 mM sucrose solution (10% protease inhibitor cocktail included) were added and several centrifugation steps to eliminate the nuclei and the cell debris followed: 2 min at 500 rpm, 2 min at 1000 rpm and 10 min at 3000 rpm. Subsequently, the supernatant, which contained the total protein fraction, was transferred to an ultracentrifuge tube and centrifuged at 48000 rpm for 45 min (Optima^{TM} TLX Ultracentrifuge, Beckman Coulter Deutschland, Krefeld, Germany; rotor: TLA 55). This time the supernatant was discarded and the pellet resuspended in 50-100 µl 0.25 mM sucrose buffer (table 2.17) using the potter homogenizer. Samples were frozen in liquid nitrogen and stored at -20°C or directly used for determination of protein content and Western Blot.

Table 2.17 Buffers for cardiac cell membrane preparation assay

Homogenization buffer	**Final concentration**
Tris-HCl	40 mM
$MgCl_2$	0.2 mM
SigmaFAST™ Protease Inhibitor Cocktail, EDTA-Free	10 % (v/v)
pH 8, 4°C	

Sucrose buffer	**Final concentration**
Tris-HCl	10 mM
Sucrose	0.25 mM
SigmaFAST™ Protease Inhibitor Cocktail, EDTA-Free	10 % (v/v)
pH 7.4, 4°C	

2.7.3 Determination of protein concentration

Cardiac cell membrane protein content of purified heart samples was determined via a Bradford assay. This colorimetric assay is based on an absorbance shift of the dye Coomassie Brilliant Blue G-250. Under acidic conditions the cationic unbound form of the dye has an absorption spectrum maximum at 465 nm. When binding to proteins the dye converts from red to blue and the absorption spectrum maximum shifts to 595 nm. This increase of absorbance at 595 nm is proportional to the amount of protein bound to the dye (Bradford, 1976).

The protein content of the samples was determined using a BSA standard curve. A dilution series of the standard protein bovine serum albumin (BSA) with the final concentrations 0, 25, 50, 75, 100, 125, 150, 175, 200 µg/ml was prepared in aqua dest. added with 0.1% sodium azide. Subsequently, 200 µl of Bradford reagent (table 2.18) was added to 20 µl of each BSA concentration. After incubation at 30°C for 2 min, extinction was measured at 595 nm with the high performance BioTek™Synergy™2Multi-Mode Microplate Reader (Biotek Germany, Bad Friedrichshall, Germany). Prior determination of the cardiac protein content, samples were diluted 1:50 in aqua dest. added with 0.1% sodium azide and treated same as the BSA dilution series. Experiments were performed in triplicates.

Table 2.18 Coomassie solution used for Bradford analysis

Bradford reagent	**Composition**
Coomassie Brilliant Blue G-250	20 mg
96 % ethanol	25 ml
85 % o-phosphoric acid	50 ml
Deionized H_2O	Ad 500 ml
Filtered, stored dark & cold	

2.7.4 Sodium dodecyl sulfate-polyacrylamide gel electrophoresis (SDS-PAGE)

SDS-PAGE describes a method to separate proteins in an electric field. Protein samples are prepared in a buffer containing the anionic detergent SDS, which denatures and linearizes them and imparts a negative charge to them. This sample preparation allows separation of proteins according to their size instead of charge. ß-mercaptoethanol is added to break disulfide bridges of the proteins. Prepared samples are subsequently transferred to an acryl amide gel and exposed to an electric field.
In general, SDS-PAGE mini gels are ideally prepared with 7% acryl amide for $Ca_V1.2$ protein separation and with 12.5% acryl amide for Rad protein separation. In the current study both proteins were separated in one gel by casting a 7% acryl amide gel on an already polymerized 10% acryl amide layer (table 2.19). By varying the acryl amide content the pore-size of the gel can be altered, thus the electrophoretic mobility. In general, smaller proteins migrate faster than larger proteins through the gel. Thus, small proteins have to be separated in a gel with high acryl amide content in order to obtain an adequate electrophoretic mobility, whereas large proteins migrate insufficient in such a gel. For polymerization of the gel TEMED as a catalyzer and APS as a radical initiator were necessary. The stacking gel (table 2.19) was casted above the separating gel in order to concentrate samples. In another preparation step protein samples were diluted 1:1 in Laemmli buffer (4x) containing 5% 2-mercaptoethanol, before being preheated at 60°C for 6 min. Thereafter an equal amount of 40 or 60 µg per sample was loaded into the gel pockets. As a protein standard Spectra Multicolor Broad Range Protein Ladder (Life Technologies) was used. The gel was run at 200 V in SDS running buffer (1x) in the Mini-PROTEAN Tetra Cell chamber (Bio-Rad Laboratories GmbH, Munich, Germany). After SDS-PAGE stacking gel was completely removed and separating gel equilibrated in Western Blot transfer buffer for 20 min.

Table 2.19 Composition of SDS-PAGE gels and running buffer

Separating gel	**Volume**	**Final concentration**
Rotiphorese®Gel 40 (37.5:1)	1.75 / 2.5 / 3.125 ml	7 / 10 / 12.5 %
Tris-HCl 3 M pH 8.8	2.5 ml	
SDS 20 % (w/v)	50 µl	
APS 10 % (w/v)	100 µl	
TEMED	10 µl	
H_2O	Ad 10 ml	

Stacking gel	**Volume**
Rotiphorese®Gel 40 (37.5:1)	670 µl
Tris-HCl 0.5 M pH 6.8	1.25 ml
SDS 20 % (w/v)	25 µl
APS 10 % (w/v)	50 µl
TEMED	5 µl
H_2O	3.075 ml

SDS running buffer (1 x)	**Final concentration**
Glycin	192 mM
Tris	25 mM
SDS	0.1 % (w/v)

2.7.5 Western Blot / blocking procedure

Western Blot is a method characterized by the transfer of proteins from a SDS gel onto a membrane, where they can be stained with antibodies specific to the target protein. Commonly the SDS gel is placed next to the membrane and an electric current is applied. Consequently, the proteins that are captured in the gel are forced to migrate towards the anode. At the time they reach the membrane, proteins are bound by hydrophobic interactions. The specific protein organization obtained after SDS-PAGE is maintained.

Experiments were conducted in the tank blotting system Mini Trans-Blot® Cell (Bio-Rad Laboratories GmbH). For blotting of $Ca_v1.2$ protein a nitrocellulose (NC) membrane (Amersham™Protran™ Premium NC, 0.45 µm, GE Healthcare) proved to be optimal. However, a polyvinylidene fluoride (PVDF) membrane (Immun-Blot® PVDF-Membrane, 0.2 µm, Bio-Rad Laboratories GmbH) was preferred (mainly due to the smaller pore size) in order to blot solely Rad protein or both proteins simultaneously. The PVDF membrane had to be activated by soaking it 1 min in 100% methanol. In addition, blotting papers (Whatman™ 3MM Chromatography Paper, GE Healthcare Life Sciences) were necessary to guarantee an equal current and to avoid drying of the pre-wetted membranes. To prepare the experiment, the NC or PVDF membranes as well as the blotting papers had to be equilibrated in transfer buffer (table 2.20). Thereafter the so-called blotting sandwich, which describes a distinct composition of SDS gel, membrane and blotting papers, was assembled as follows:

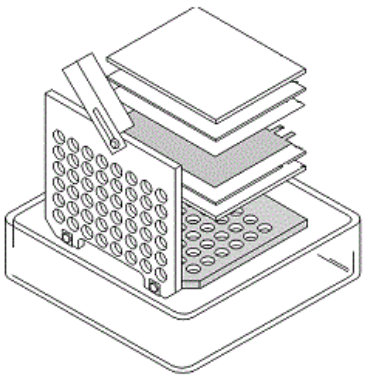

Figure 2.4 **Composition of the blotting sandwich** (adapted from Bio-Rad Mini Trans-Blot® Cell Instruction Manual).

The SDS-PAGE gel was blotted over night at 100 mA, 4°C. Quality of transfer was checked with Ponceau S staining solution. Proteins which might be retained in the gel were visualized via a Coomassie staining (table 2.21).

Table 2.20 Western Blot buffer composition

Transfer buffer	**Final concentration**
Boric acid	50 mM
Methanol	10 % (v/v)
pH 8.5, 4°C	

Table 2.21 Staining solutions

Ponceau S staining solution	**Final concentration**
Ponceau S	0.1 % (w/v)
Acetic acid	5 % (v/v)

Coomassie staining solution	**Final concentration**
Coomassie Brilliant Blue G-250	0.25 % (w/v)
Acetic acid	10 % (v/v)
MeOH	50 % (v/v)
H_2O	40 % (v/v)

After destaining of the membrane in tris buffered solution, containing 0.1% tween 20 (TBS-T 0.1 %; table 2.22), it was blocked in 5% milk powder (MP) in TBS (1 h at room temperature). This blocking solution reduced unspecific binding of antibodies and thus background signals.

Table 2.22 Composition of TBS and TBS-T

TBS	**Final concentration**
Tris-HCl	50 mM
NaCl	150 mM
pH 7.5	

TBS-T 0.1 %	Final concentration
TBS	99.9 % (v/v)
Tween	0.1 % (v/v)
pH 7.5	

2.7.6 Antibody incubation and protein detection

Proteins transferred onto a membrane can be detected with antibodies specific to the target protein and linked assays, e.g. a chemiluminescence reaction assay.
For short, the primary antibody (table 2.23) was applied to the blocked membrane and incubated over night at 4°C with constant agitating. Both proteins of interest were incubated separately with the corresponding antibodies. For this, membrane was cut horizontally at the level of the 100 kDa band of the protein standard. Following the first incubation, membrane piece was washed in TBS-T 0.1% (3 x 5 min) and exposed to the secondary antibody. Unbound secondary antibody was also washed off after 1.5 hours of incubation at room temperature. Subsequently, protein detection was possible because of a chemiluminescence reaction between the horseradish peroxidase (HRP) coupled to the secondary antibody and the substrate luminol, included in the detection kit SuperSignal™ West Pico Chemiluminescent Substrate (Thermo Scientific). Chemiluminescence was captured with the MultiImage® II system (Alpha Innotech) and manifested in visible bands with variable densities. Each membrane was detected in total, thus providing results for $Ca_v1.2$ and Rad in the same image recorded.

Table 2.23 Antibodies for specific protein detection

Antibody name	Host species	Clonality	Application
ANTI-RRAD (Sigma Aldrich; SAB2502049)	Goat	Polyclonal	1:500 in 2.5 % MP in TBS-T 0.05 % (+ 0.1 % sodium azide)
Anti-Calcium Channel (Sigma Aldrich; C1603)	Rabbit	Polyclonal	1:200 in 1 % MP in TBS-T 0.1 % (+ 0.1 % sodium azide)
Swine Anti-Rabbit Ig-HRP (Dako; P0399)	Donkey	Polyclonal	1:5000 in 5 % MP in TBS
Swine Anti-Rabbit Ig-HRP (Dako; P0399)	Swine	Polyclonal	1:2000 in 5 % MP in TBS

2.7.7 Western Blot: data analysis

Bradford measurements were analyzed with Gen5^{TM} Data Analysis Software (BIOTEK Deutschland, Berlin, Germany). Western Blot images were interpreted by quantitative comparing of the band densities using ImageJ software tool (National Institutes of Health, New York City, NY, USA).

2.8 Electrophysiology

2.8.1 Patch-clamp technique

The patch-clamp technique was first described by Erwin Neher and Bert Sakmann in 1976. They detected single-channel current activity in acetylcholine-activated channels of frog skeletal muscle membranes via the cell-attached method (Neher et al., 1978). A small part of the cell membrane is electrically isolated by attaching a glass electrode onto its surface via gentle suction, resulting in a high resistance gigaohm seal. Upon receipt of a gigaohm seal, several patch-clamp configurations are possible: cell-attached, inside-out, outside-in or whole-cell (Hamill et al., 1981). This study was focused on the whole-cell voltage-clamp configuration, discovered by Kenneth Cole and H. J. Curtis and further developed by Alan Hodgkin and Andrew Huxley (Hodgkin et al., 1952). The whole-cell voltage-clamp configuration enables detection of ion channel current density among the whole cell membrane (see also chapter 2.8.4).
A simplified scheme of the voltage-clamp method is depicted in figure 2.5. With obtainment of a stable gigaohm seal, the cell-attached configuration is achieved. Once the small part of the attached membrane is ruptured by further suction, the pipette contents equilibrate with the cell's cytoplasm and impose an artificial ionic potential across the membrane. In this way, the voltage across the entire cell membrane is patched (whole-cell mode) and the current density of all the channels expressed at the membrane surface can be monitored. Using the voltage-clamp mode, the membrane potential of the cell (the pipette voltage, V_p) can be set to a user-specific value, the so-called command potential (V_{com} or V_{clamp}). The current (I_{cell}) required to maintain the command voltage, is recorded through a voltage drop across the feedback resistor (R_F) of the amplifier. The resulting output voltage (V_{out}) is linearly proportional to the measured current. Hence, the measured current is proportional to the compensating

current. Detected currents are in a range of pA, therefore amplifiers are used for a better resolution.

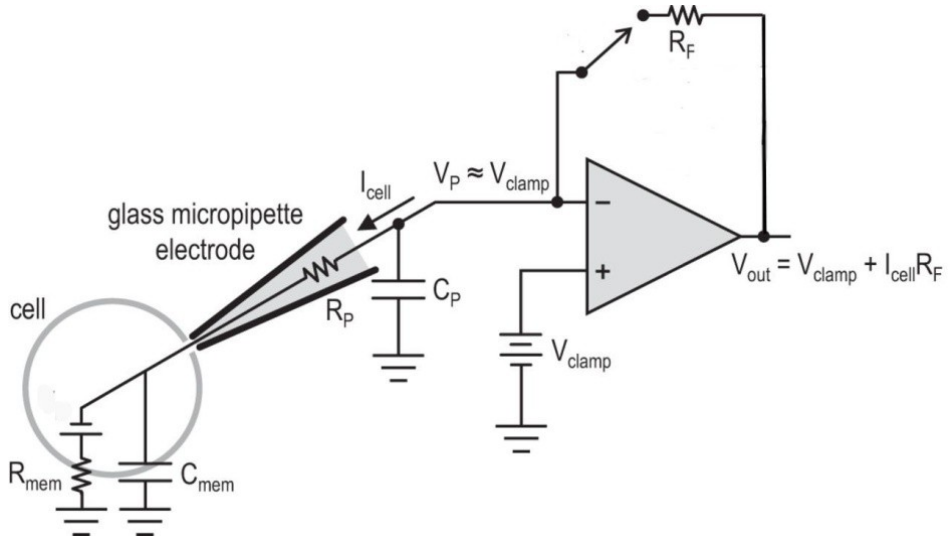

Figure 2.5 **Simplified schematic of a traditional patch-clamp amplifier in voltage-clamp mode**; R_{mem} = membrane resistance, C_{mem} = membrane capacity, R_p = pipette resistance, C_p = pipette capacity, I_{cell} = measured current, V_p = pipette voltage, V_{clamp} = command potential, R_F = feedback resistor, V_{out} = output voltage (modified from Harrison et al., 2015).

2.8.2 Patch-clamp setup

As outlined in figure 2.6 (A), electrophysiologic experiments are carried out in a faraday cage that insulates the setup from surrounding electrical fields. To reduce artefacts, the inverted microscope (Nikon Eclipse Ti-U, Nikon instruments, Japan) is placed on a vibration-cushioned table and all instruments are isolated and grounded. Furthermore, the setup possesses a hydraulic micromanipulator (MHW-103, Narishige International, Tokyo, Japan) to move the micropipette in the desired position. The headstage preamplifier (CV 203BU, Axon Instruments, Sunnyvale, CA, USA) has an integrated capacitor-feedback that is able to measure the current as the rate of voltage increase across the capacitor. The main amplifier (Axopatch 200B, Axon Instruments), the analog-digital converter (Digidata 1440A, Axon Instruments) and the computer are positioned outside the faraday cage (figure 2.6 (B)). The main amplifier fortifies the measured signals, enables ultra low-noise recordings and includes a control unit, that allows diverse regulation, e.g. cell capacitance compensation. The analog-digital converter receives the analog signals from the amplifier and transforms them into digital signals, that can be captured by pClamp10.2 software (Axon Instruments) installed on the computer. Recording electrode and bath electrode consist of silver wires coated with

AgCl (AG-15W, Science Products GmbH, Hofheim, Germany). Coating was performed by immersing the wire into a 3 M KCl solution; the applied voltage of 1 mA permits an oxidation reaction: $Ag + Cl^- \leftrightarrow AgCl + e^-$.

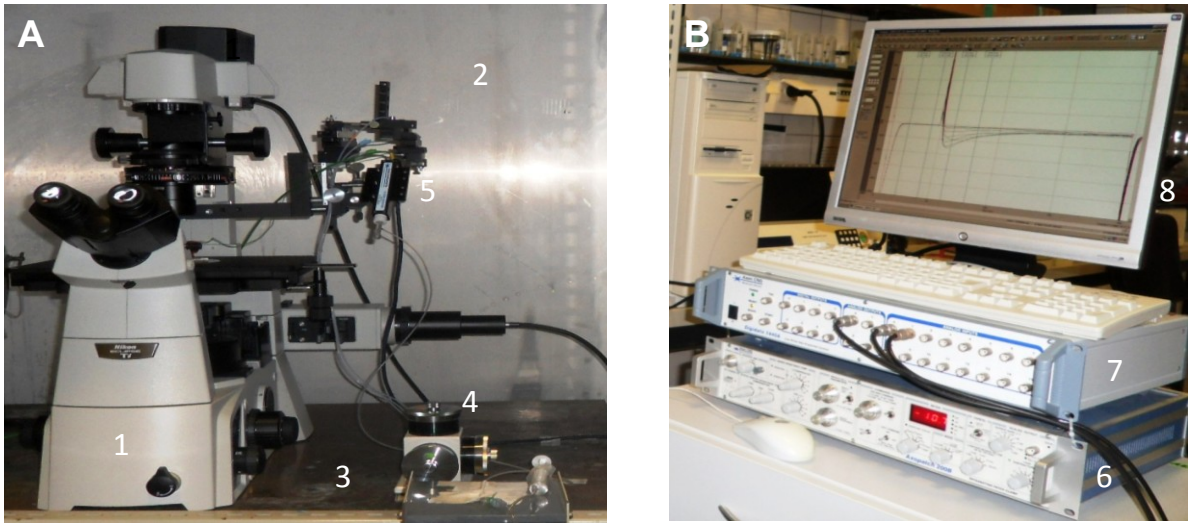

Figure 2.6 **Patch-clamp setup** (A): (1) inverted fluorescence microscope (2) faraday cage (3) vibration-cushioned table (4) hydraulic micromanipulator (5) headstage preamplifier with pipette holder (B): (6) main amplifier (7) AC/DA-converter (8) computer containing acquisition and analysis software.

2.8.3 Patch pipettes

The chemical composition of the glass used for preparation of patch pipettes is important to reduce the background noise level. Moreover, its ability to form pipettes with appropriate tip size and taper is crucial to achieve a good seal resistance between pipette and cell membrane (Rae and Levis, 1992). At the day of experiment pipettes were prepared out of borosilicate glass capillaries (1.7 mm OD; 1.133 mm ID; 0.283 mm wall thickness; Hilgenberg, Malsfeld, Germany) using a horizontal pipette puller (P-97, Sutter instruments). Fire-polishing of the micropipette tips was performed using a microforge (MF-83, Narishige International). Smoothing of the glass tips was necessary to ensure stable seal formation. In case of whole-cell recordings the pipette resistance should be in the range of 1.7-3.0 MΩ; the resistance is a useful indicator for the pipette tip size, i.e. the lower the resistance the larger the tip size and vice versa.

2.8.4 Whole-cell recordings: solutions and data acquisition

Whole-cell patch-clamp experiments were performed to detect the calcium current density of enzymatically isolated cardiac myocytes. Furthermore, the whole-cell mode also allows the description of kinetic properties of the membrane ion channels.
Bath and pipette solutions (table 2.24) were prepared freshly on each experimental day. Composition of bath solution was orientated on physiological extracellular ionic concentrations. Pipette solution contained cesium ions to block potassium channels, EGTA as a calcium chelator and ATP to prevent rapid calcium current rundown (Belles et al., 1988). Approx. 100 µl of cardiomyocyte cell suspension was transferred to a tissue culture dish (polystyrene, 35 x 10 mm) and covered with 3 ml of bath solution. Rod-shaped and quiescent myocytes were patched after having settled. Glass pipettes were filled with pipette solution in two steps (tip and back filling) and bubbles were completely removed via gentle tapping. Pipettes were connected to the pipette holder containing the recording electrode. To avoid clogging of the pipette tip, a small positive pressure was applied. 5 mV depolarization steps were repeatedly applied via the patch-clamp amplifier and the pipette immersed in the bath solution (figure 2.7 (A)). The approach of the pipette tip to the cell membrane was controlled by the change in pipette resistance. The pipette resistance was described by a visible rectangle pulse; the higher the pulse the lower the resistance.
To reach cell-attached configuration, the pipette was positioned over a cell and its pressure released shortly before contacting the cell membrane. Gigaohm seal formation was achieved either spontaneously or by gentle suction, indicated by a fast reduction and finally extinction of the rectangle pulse (figure 2.7 (B)). This cell-attached patch-clamp configuration is essential for preventing leak currents and allows for tight voltage control of the cell membrane. After achieving a stable gigaohm seal, membrane potential was set to -80 mV and fast capacity transients, that are mainly associated with pipette capacitance, were compensated (figure 2.7 (C)). A further suction was required to rupture the membrane and merge into the whole-cell mode (figure 2.7 (D)); the pipette solution then was in contact with the cytoplasm and equilibrated. Whole-cell capacitance transients, reflecting the passive charging of the cell, were adjusted with the appropriate amplifier controls. Membrane capacitance was automatically determined by pClamp 10.2 software. The amplifier was set as follows: V-Clamp mode, whole-cell configuration ß 1, output gain alpha 2, lowpass bessel filter 2 kHz.

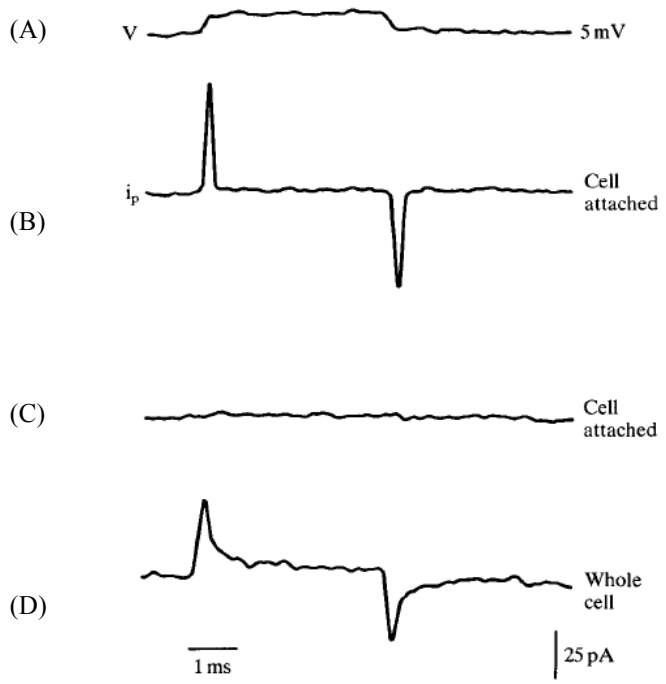

Figure 2.7 **Capacity transients observed going whole-cell**: (A) a rectangular test pulse of 5 mV amplitude is applied to the patch-clamp input in order to monitor the capacity transients. Fast capacity transient currents in a cell-attached configuration before (B) and after (C) compensation occur due to pipette resistance. (D) Whole-cell configuration is indicated by the appearance of large capacity transients at the leading and trailing edges of the pulse (adapted from Ogden and Stanfield, 1987).

Table 2.24 Patch-clamp solutions for whole-cell measurements

Bath solution	**Final concentration**
NaCl	137 mM
CsCl	5.4 mM
$CaCl_2$ * 2 H_2O	2 mM
$MgCl_2$ * 6 H_2O	1 mM
Glucose	10 mM
HEPES	10 mM
pH 7.4 with NaOH	

Pipette solution	**Final concentration**
CsCl	120 mM
Mg-ATP	4 mM
$MgCl_2$ * 6 H_2O	1 mM
EGTA	10 mM
HEPES	5 mM
pH 7.2 with CsOH	

2.8.5 Whole-cell recordings: pulse protocols

I/V curve pulse protocol

To evaluate the relation of current and voltage of $Ca_V1.2$ channels, a so-called current-voltage curve pulse protocol (I/V protocol) was used (figure 2.8 and 2.9 (B)). The cell was held at -80 mV and depolarized for 45 ms to the first level of -40 mV in order to inactivate sodium channels. Subsequently, 150 ms test pulse voltages were applied, ranging from -40 mV to +50 mV with 10 mV increment. After each of these test pulses the cell was repolarized to the resting potential of -80 mV. Pulse intervals were 3 sec. Sampling rate per pulse was 5 kHz. Further amplifier parameters were set as follows: additional gain x 2, lowpass filter frequency 500 Hz.

The peak current amplitudes were analyzed in order to obtain an I/V curve, to calculate the potential of half maximal (in-)activation $V_{0.5(in)act}$ and to determine the slope factor. The time constant of the inactivation kinetics tau (τ) was analyzed, too.

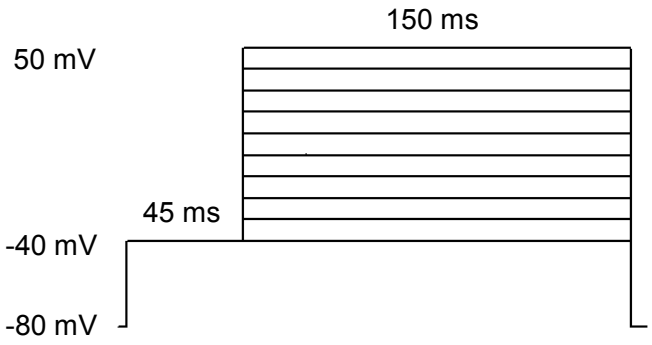

Figure 2.8 **I/V curve pulse protocol.** The cell was held at -80 mV and depolarized for 45 ms to the first level of -40 mV. Subsequently, 150 ms test pulse voltages were applied, ranging from -40 mV to +50 mV with 10 mV increment.

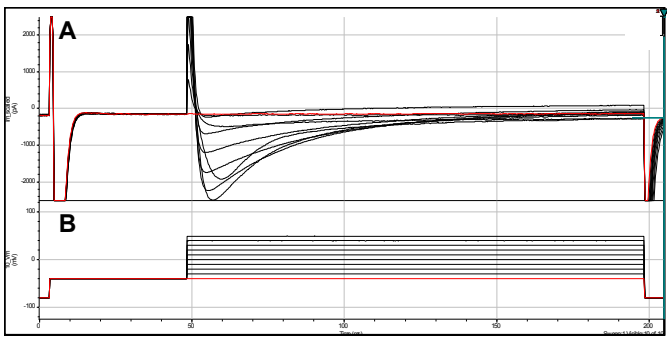

Figure 2.9 **Exemplary original traces** (A) recorded with the I/V curve pulse protocol (B). For analysis, the peak current amplitudes were determined.

A high-quality I/V relationship was prerequisite for further experiments, i.e. determination of recovery from inactivation and steady-state inactivation, respectively. These pulse protocols were run in order to determine kinetic properties, that are characteristic for LTCCs switching between open, closed and inactive state.

Recovery from inactivation

Recovery from inactivation was examined by a double-pulse step protocol with 15 sweeps, as outlined in figure 2.10 and 2.11 (B). With a prepulse the holding potential of -45 mV was set to 0 mV for 100 ms to induce calcium currents close to maximum amplitude (current I1, figure 2.11 (A)). After this prepulse membrane potential was set back to -45 mV for varying time intervals ranging from 25 ms to 375 ms (with 25 ms increment per sweep). Subsequently, a second test pulse of 50 ms to 0 mV was applied (current I2, figure 2.11 (A)). Thereafter, cells were held at -45 mV until the sweep ends (sweep duration: 1024 ms). During the increasing time intervals channels recovered partially in a time-dependent manner, i.e. I2 and the ratio of I2 and I1 were enhanced with prolonging interval duration. Three sec time intervals between sweeps at -45 mV allowed complete recovery of all channels and thus (close to) maximum current response again. Sampling rate per sweep was 2 kHz. Further amplifier parameters were set as follows: additional gain x 2, lowpass filter frequency 500 Hz. The relative current after 375 ms of recovery, the time constant tau (τ) and the half-time were determined.

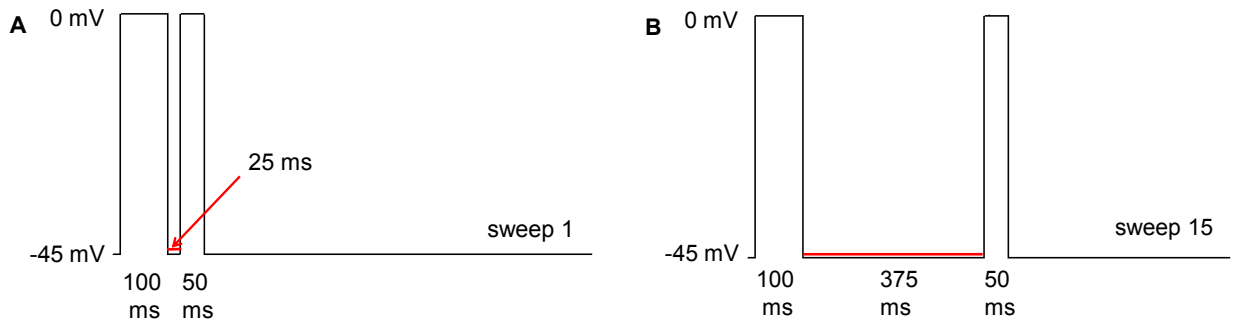

Figure 2.10 **Pulse protocol for recovery from inactivation**. With a prepulse the holding potential of -45 mV was set to 0 mV for 100 ms. After this prepulse the membrane potential was set back to -45 mV for varying time intervals with 25 ms increment per sweep: sweep 1 starts with 25 ms time interval duration (A) and the last sweep ends with 375 ms time interval duration (B). Subsequently, a second test pulse of 50 ms to 0 mV was applied. Thereafter, cells were held at -45 mV until the sweep ends.

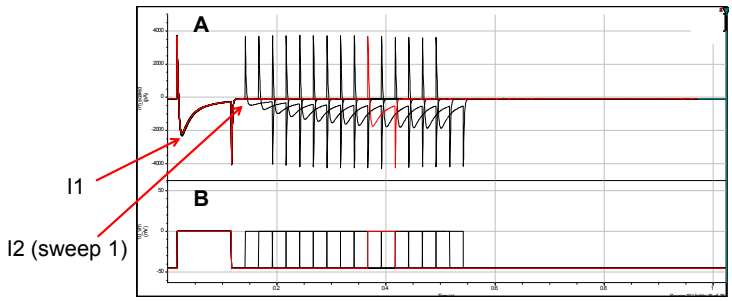

Figure 2.11 **Exemplary original traces** (A) recorded with the recovery from inactivation protocol (B). For analysis, the peak current amplitudes I1 and I2 were determined.

Steady-state inactivation

Steady-state inactivation kinetics of the cell was determined using a step protocol consisting of 13 sweeps, as demonstrated in figure 2.12 and 2.13 (B). Corresponding to the I/V-protocol, the membrane potential was initially set to -80 mV (for 5 ms) and then depolarized to -40 mV (for 25 ms) for sodium current inactivation. Thereafter, maximum current density (I1, figure 2.13 (A)) of the calcium channels was induced via a 200 ms prepulse to 0 mV. Steady-state inactivation was induced by conditional test pulses ranging from -60 mV to +60 mV for 2000 ms (in 10 mV steps per sweep). Immediately after this the -80 mV / -40 mV / 0 mV protocol was repeated to quantify the still inducible currents (I2, figure 2.13 (A)). Sweep interval was 10 sec at -80 mV. Sampling rate per sweep was 2 kHz. Further amplifier parameters were set as follows: additional gain x 2, lowpass filter frequency 500 Hz. The voltage of half maximum inactivation $V_{0.5inact}$ and the slope factor were calculated.

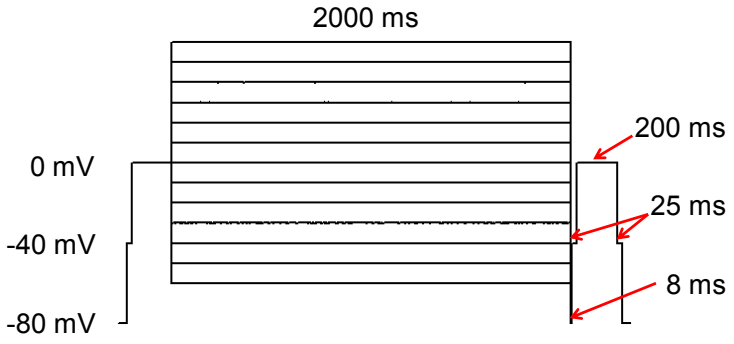

Figure 2.12 **Steady-state inactivation pulse protocol.** Membrane potential was initially set to -80 mV and then depolarized to -40 mV for 25 ms. Thereafter, a 200 ms prepulse to 0 mV followed. Steady-state inactivation was induced by conditional test pulses ranging from -60 mV to +60 mV. After each conditional test pulse, the -80 mV / -40 mV / 0 mV protocol was repeated.

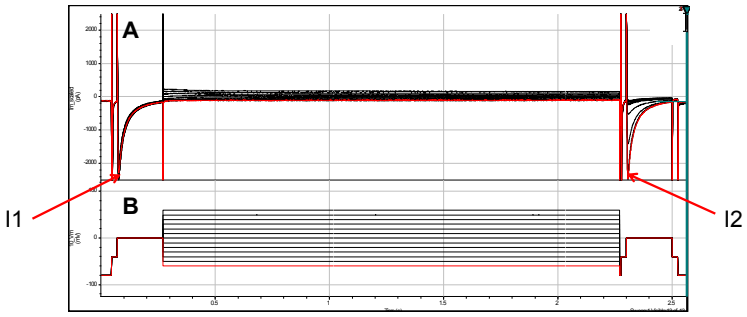

Figure 2.13 **Exemplary original traces** (A) recorded with the steady-state inactivation protocol (B). For analysis, the peak current amplitudes I1 and I2 were determined.

2.8.6 Whole-cell recordings: data analysis

For data analysis Clampfit 10.2 software (Axon Instruments) and GraphPad Prism®6 (GraphPad Software, La Jolla, CA, USA) were used.

To determine current-voltage dependency, the peak current amplitude of each test pulse was measured and corrected by the leak current of the corresponding potential. By dividing the leak-corrected peak current amplitude by the cell capacitance and thus normalizing to cell size, the I/V relationship was obtained. To determine the potential of half maximal activation $V_{0.5act}$ and the slope factor, I/V curves were fitted to a combined Boltzmann and Ohm relation using the following equation:

$$I_V = G_{max} (V-V_{rev})/(1+\exp[(V_{0.5act}-V)/k])$$

I_V: current density at voltage V
k: slope factor
G_{max}: maximal slope conductance
V_{rev}: reversal potential
$V_{0.5act}$: half maximal activation voltage

The time constant of the inactivation kinetics tau (τ) was calculated by a mono-exponential fit of the slow inactivation phase of the raw calcium current traces according to following equation:

$$I_t = I_0 + (plateau-I_0)*(1-\exp(-k*t))$$

I_t: current density at time t
I_0: “starting” current density
t: time
k: slope factor

The recovery from inactivation curve was determined by calculating the second peak current amplitude (I2) at 0 mV after varying test pulse time intervals and normalizing it to the respective first peak current amplitude (I1) measured during the prepulse. The relative currents after varying recovery intervals, the time constant tau (τ) and the half-time were determined by a mono-exponential fit of the data.

The steady-state inactivation curve was assessed by the peak current amplitude (I2) obtained at 0 mV after variable conditional test pulse potentials, normalized to the peak current amplitude (I1) measured at the beginning of each sweep. The voltage of half maximum inactivation $V_{0.5inact}$ and the slope factor of steady-state inactivation were determined by fitting a Boltzmann function (k-sigmoidal) to the data:

$$I_v = I_{max}/(1+\exp[(V_{0.5inact}-V)/-k])$$

I_V: current density at voltage V
$V_{0.5inact}$: half maximal inactivation voltage
k: slope factor

3 Results

The investigated mouse lines (ob/ob, Rad-k.o., ob/ob x Rad-k.o. and IRS 2-k.o. mice) were compared to age-matched wt animals (C57BL/6J). For each comparison the same wt cohort was used (at 16 and 28 weeks, respectively).

All data are given as geometrical mean ± standard error of the mean (SEM). If not mentioned otherwise Student's t-test was used for statistical analysis. P-values < 0.05 were defined to indicate statistically significant differences.

An overview of all results in more detail is given in the appendix (tables 8.1–8.10). Additional information about results of method validation can be found in the appendix, too.

3.1 Offspring statistics

Over a period of 3.5 years our own breedings were observed with respect to mean litter size and distribution of sexes and genotypes. In all breedings distribution of sexes was similar, as outlined in figure 3.1.

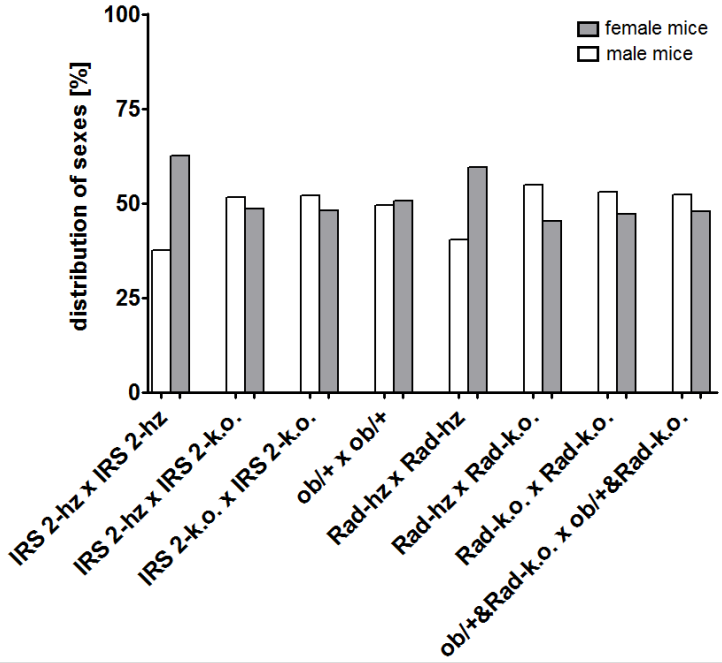

Figure 3.1 **Distribution of sexes:** sexes were similarly distributed in most breedings (hz = heterozygous, k.o. = knockout).

Averages of offspring per litter of the different breeding schemes did not differ as well (in one-way ANOVA; Bonferroni's Post Test; figure 3.2).

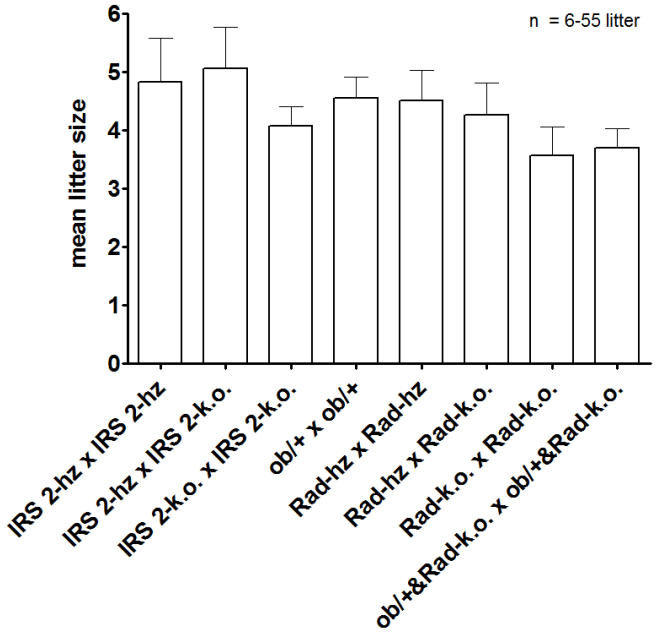

Figure 3.2 **Mean litter sizes:** averages of offspring per litter of the different breeding schemes did not differ (n = 6–55 litter; in one-way ANOVA; Bonferroni's Post Test).

Mendelian inheritance stands for heredity transmission of genes from one generation to the next following the laws proposed by Gregor Johann Mendel. According to Mendel genotypes of descendants are expected to split in distinct ratios. For example, genotypes of descendants should be distributed 1:1 in breedings consisting of a heterozygous (hz) and a k.o. mouse. The predicted Mendelian ratio in breedings with only hz animals is 1:2:1, with hz offspring dominating. As demonstrated in table 3.1, all genotypes were distributed as expectable according to these ratios.

Table 3.1 **Genotype distributions:** all genotypes were distributed as expectable according to the Mendelian Law.

Breeding scheme	Number of genotyped mice	Genotype distribution wt : hz : k.o.
IRS 2-hz x IRS 2-k.o.	64	1.0 : 0.6
IRS 2-hz x IRS 2-hz	32	1.0 : 2.1 : 0.9
Ob/+ x ob/+	210	1.0 : 2.2 : 1.3
Rad-hz x Rad-k.o.	51	1.0 : 0.5
Rad-hz x Rad-hz	125	1.0 : 1.4 : 0.8
Ob/+ x Rad-k.o.	129	1.0 : 1.6 : 1.0

3.2 Phenotype characterization

Regarding the behavior of IRS 2-k.o. and Rad-k.o. mice there was no obvious difference compared to C57BL/6J control animals. Ob/ob and ob/ob x Rad-k.o. mice showed a different feeding behavior. These animals appeared to be mainly focused on food uptake and thus gained an intense weight with progressing age (figure 3.3; chapter 3.3.1 and 3.5.1). Moreover, increased urination was noticeable.

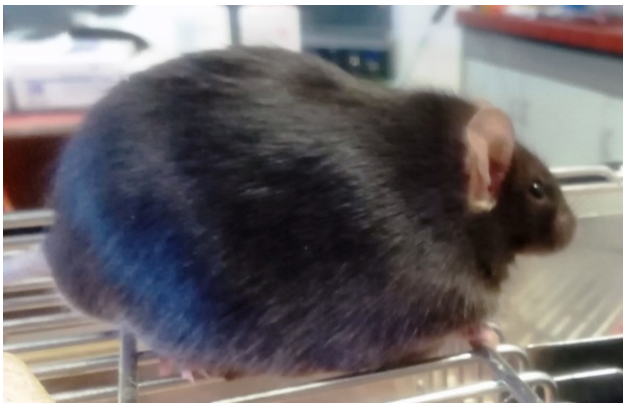

Figure 3.3 **Phenotype of ob/ob mice:** ob/ob mice gained remarkably weight because of feeding behavior.

3.3 Ob/ob mice

3.3.1 Blood glucose, body weight, ventricle weight and ventricle-to-body weight ratio

As illustrated in figure 3.4 (A), 16 week old ob/ob mice' (non-fasting) blood glucose values were significantly elevated compared to age-matched wt animals (ob/ob: 270 ± 29 mg/dl, N = 20 vs. wt: 158 ± 5 mg/dl, N = 58). At 28 weeks of age blood glucose of ob/ob mice dropped significantly compared to younger mice of the same genotype, but still exceeded that of age-matched wt (ob/ob: 203 ± 18 mg/dl, N = 33 vs. wt: 168 ± 6 mg/dl, N = 41; p = 0.05). Already at an age of 16 weeks body weight of ob/ob mice was nearly twice than that of age-matched wt littermates (ob/ob: 46.6 ± 2.0 g, N = 20 vs. wt: 24.4 ± 0.5 g, N = 62). At an age of 28 weeks body weight was even more than doubled compared to wt (ob/ob: 60.3 ± 1.5 g, N = 33 vs. wt: 27.6 ± 0.6 g, N = 42; figure 3.4 (B)). Ventricle weights of ob/ob and age-matched wt mice were not significantly different at both ages (figure 3.4 (C)). Ventricle-to-body weight ratios were determined in order to detect a putative cardiac hypertrophy (figure 3.4 (D)). As expected, ob/ob mice showed significantly decreased ratios (2.8 ± 0.2 mg/g at 16 and 28 weeks, N = 13 and 16) in comparison to wt animals (5.4 ± 0.2 mg/g, N = 36 at 16 weeks and 5.2 ± 0.2 mg/g, N = 21 at 28 weeks), but there was no difference between young and old ob/ob mice.

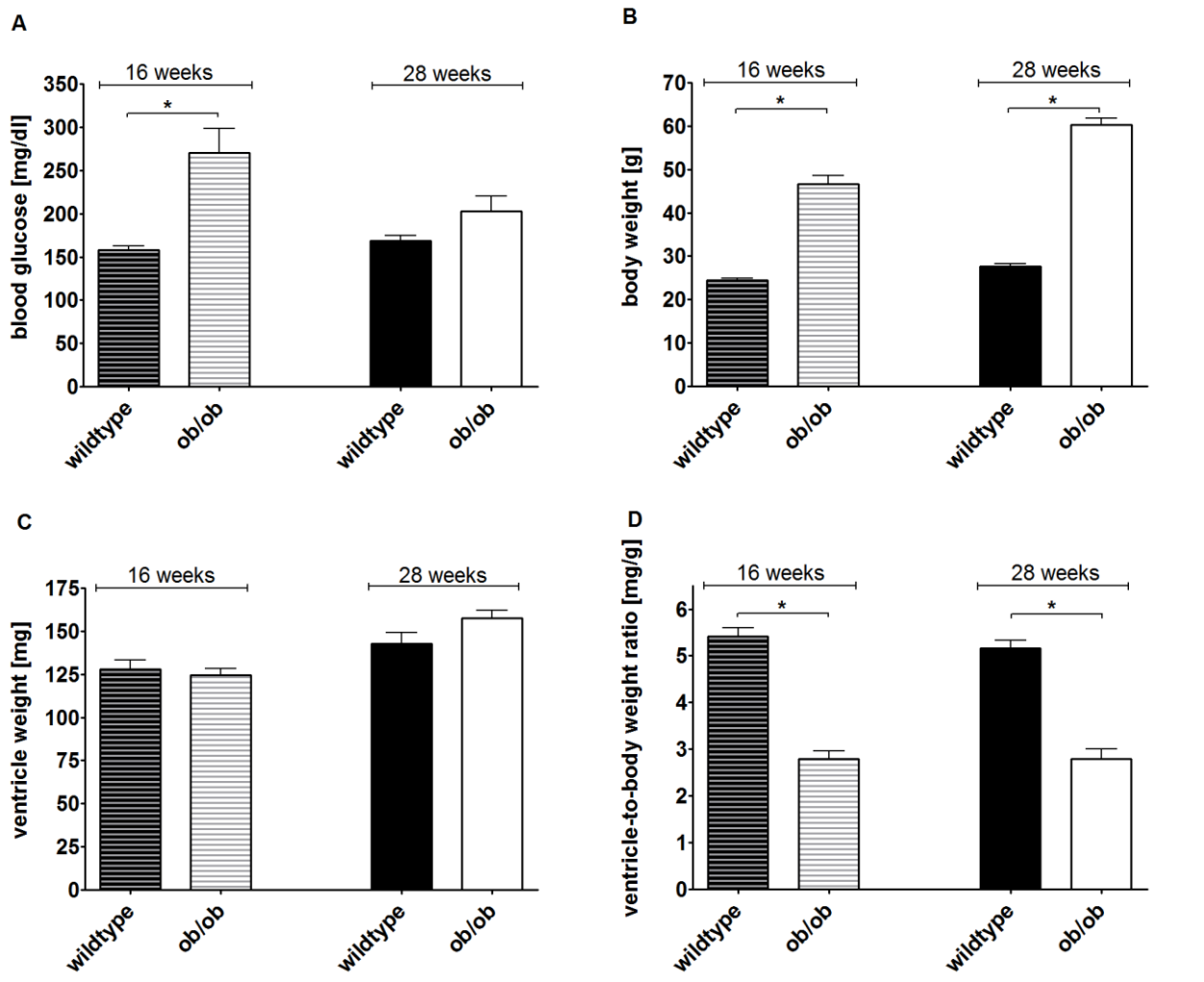

Figure 3.4 **Blood glucose, body weight, ventricle weight and ventricle-to-body weight ratio of ob/ob mice:** young ob/ob mice had significantly higher blood glucose values compared to wt (A). Body weights of ob/ob mice were (nearly) twice than that of wt (B). Ventricle weights of ob/ob and wt mice were similar (C). As expected, ob/ob mice showed significantly decreased ventricle-to-body weight ratios in comparison to wt animals (D) (N = 20-62 for (A, B); N = 13-36 for (C, D); * = $p < 0.05$ vs. age-matched wt).

3.3.2 Functional properties of cardiac whole-cell LTCC currents

To investigate the functional properties of the isolated cardiomyocytes patch-clamp experiments were performed with rod-shaped and mainly quiescent cells. Patched cells isolated from ob/ob and wt mice had similar mean cell capacitances at both ages investigated (appendix, chapter 8.3.1). Therefore, experiments were comparable and there was no hint towards cellular hypertrophy. Only recordings of stable-patched cells were analyzed. Measurements reflecting strong leak currents were discarded. The I/V relationship always was the first protocol of a cell measured according to the pulse protocol in figure 2.8. Representative I/V recordings for ob/ob and wt mice are depicted in figure 3.5.

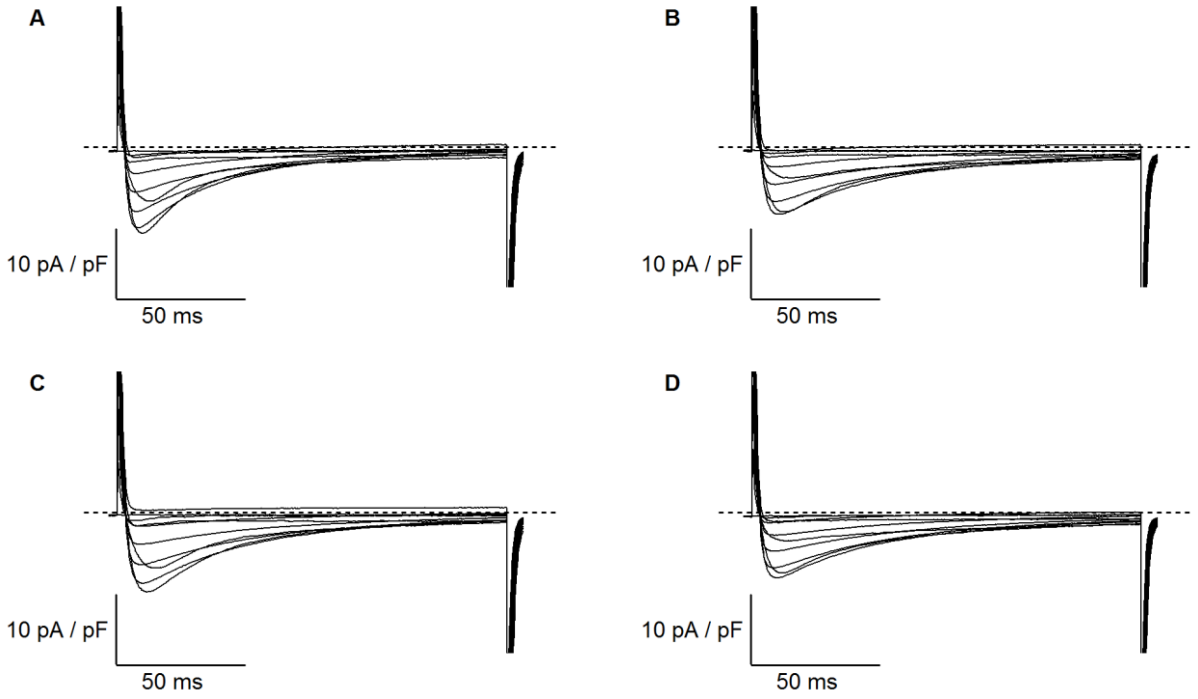

Figure 3.5 **Example of representative and good quality I/V recordings for wt (A, B) and ob/ob (C, D) mice** at 16 and 28 weeks of age, respectively.

As demonstrated in figure 3.6, at all applied test potentials the maximum whole-cell Ca^{2+} current densities were similar in ob/ob and age-matched wt mice at both ages (ob/ob: -10.75 ± 0.65 pA/pF, n = 10 vs. wt: -10.92 ± 0.90 pA/pF, n =17 at 16 weeks of age and ob/ob: -8.44 ± 0.43 pA/pF, n = 11 vs. wt: -8.91 ± 0.54 pA/pF, n = 13 at 28 weeks of age). The potential of half maximal activation ($V_{0.5act}$) was slightly altered in both age groups. In 16 week old ob/ob mice $V_{0.5act}$ was significantly shifted to the left (ob/ob: -11.72 ± 0.60 mV vs. wt: 8.69 ± 1.06 mV), while in older mice $V_{0.5act}$ was significantly shifted to the right (ob/ob: -4.86 ± 0.67 mV vs. wt: -7.51 ± 0.96 mV).

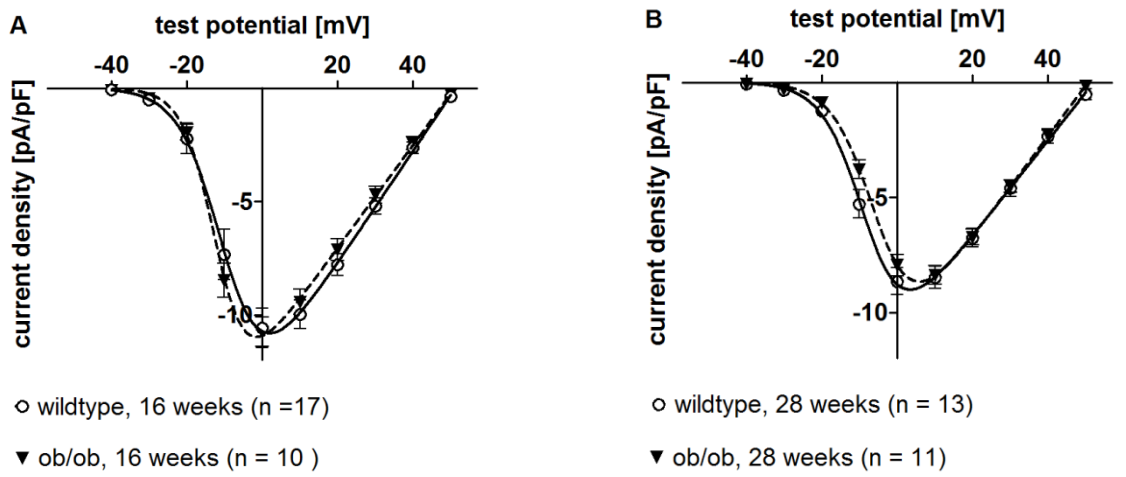

Figure 3.6 **Current density-voltage relationships of ob/ob mice:** the I/V curves revealed that the maximum whole-cell Ca^{2+} current densities were similar in ob/ob and wt mice. In young ob/ob mice $V_{0.5act}$ was significantly shifted to the left (A), while in older animals $V_{0.5act}$ was significantly shifted to the right (B) (n = number of patched cells; number of mice: N = 5-10 for wt, N = 4-5 for ob/ob).

Ventricular whole-cell LTCCs of 16 week old ob/ob mice showed a significantly faster time-dependent inactivation at -10 mV as well as a significantly slower inactivation at 10 mV (figure 3.7 (A)). At 28 weeks of age time-dependent inactivation was significantly slowed at -10 mV and significantly faster in the range of 10 to 40 mV (figure 3.7 (B)).

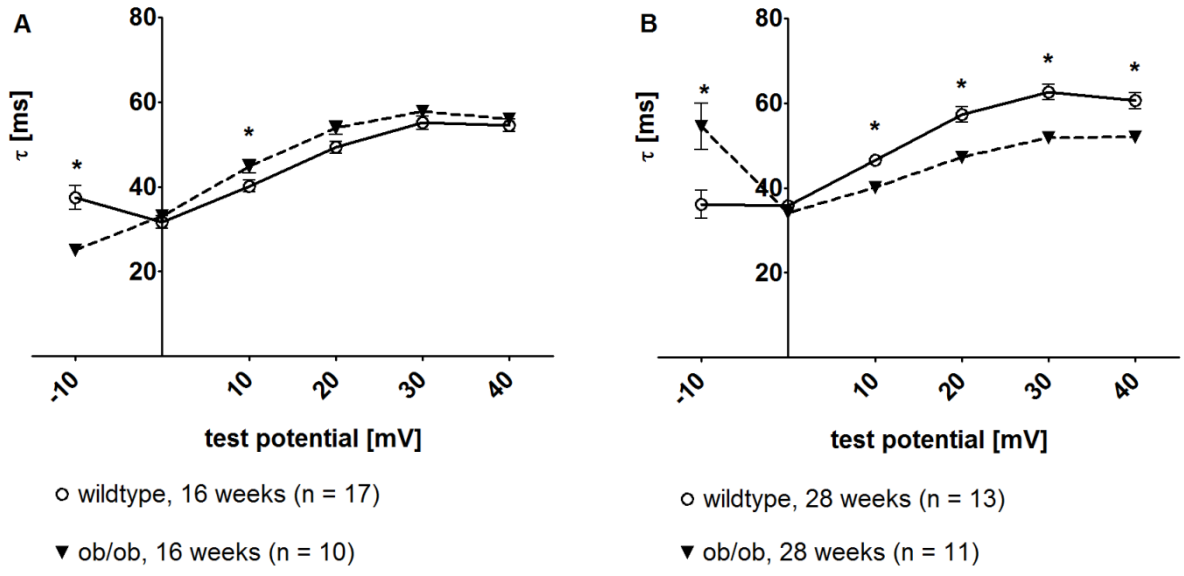

Figure 3.7 **Time-dependent inactivation properties of ob/ob mice:** the time constant of the inactivation kinetics tau was slightly changed in ventricular whole-cell LTCCs of 16 week old ob/ob mice (A). Whole-cell LTCCs inactivated significantly faster in the range of 10 mV to 40 mV in cells of 28 week old ob/ob mice (B) (n = number of patched cells; number of mice: N = 5-10 for wt, N = 4-5 for ob/ob; * = $p < 0.05$ vs. age-matched wt).

Voltage-dependent inactivation/steady-state inactivation properties of ventricular whole-cell LTCCs of ob/ob and wt mice were comparable at both ages investigated (figure 3.8).

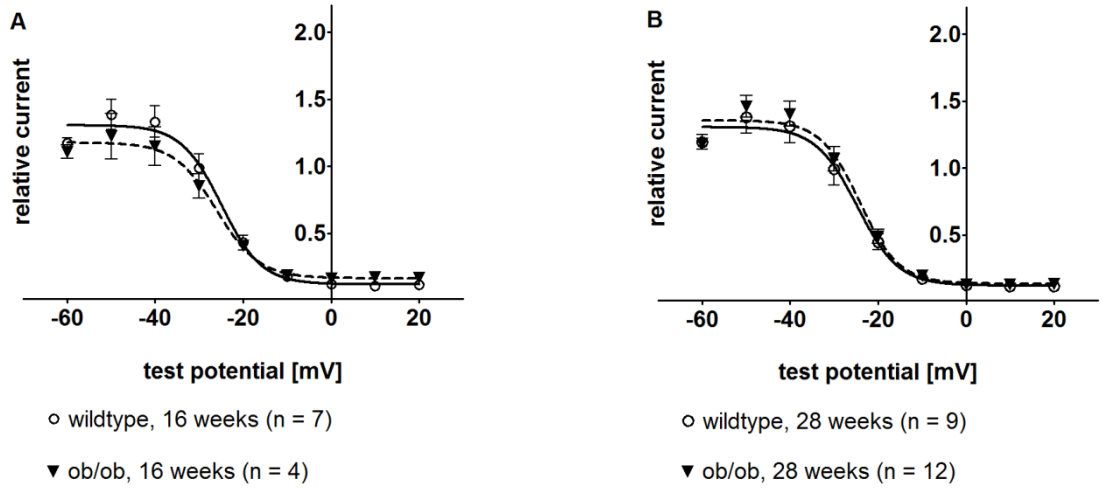

Figure 3.8 **Steady-state inactivation properties of ob/ob mice:** steady-state inactivation properties of ventricular whole-cell LTCCs of ob/ob and wt mice were comparable at both age groups (n = number of patched cells; number of mice: N = 4 for wt, N = 2-3 for ob/ob).

At both age groups recovery from inactivation was similar in ob/ob and wt mice. The relative current after 375 ms of recovery reached mean values in the range of 0.76-0.84 (figure 3.9).

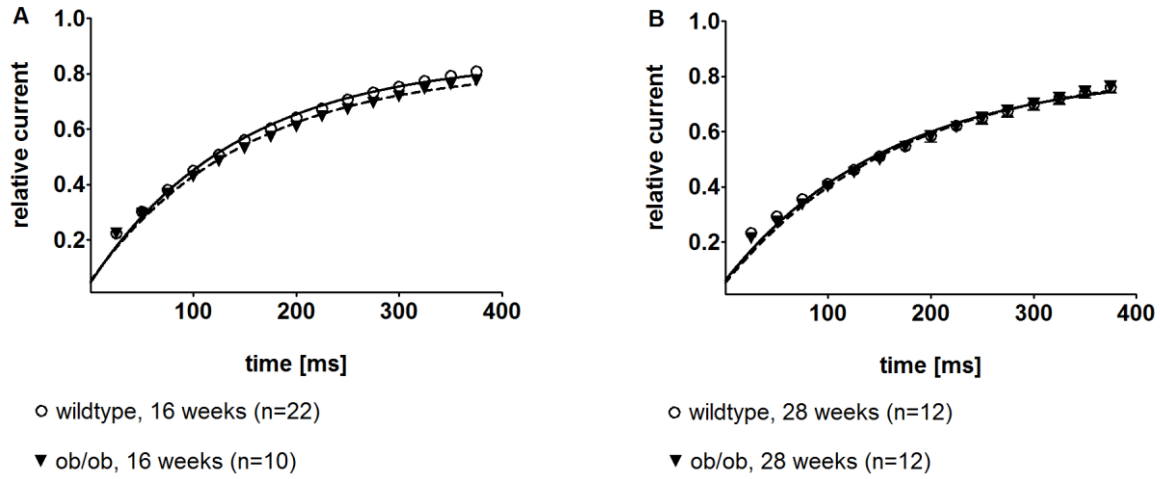

Figure 3.9 **Recovery from inactivation properties of ob/ob mice:** recovery from inactivation revealed no significant differences between ob/ob and wt mice at both age groups (n = number of patched cells; number of mice: N = 5-8 for wt, N = 4-5 for ob/ob).

3.3.3 Cardiac mRNA expression levels

Compared to age-matched wt mice RGK mRNA expression was not significantly altered in ventricles of ob/ob mice, though there was a numerical increase of Rad mRNA expression (1.55 ± 0.27, p = 0.19 at 16 weeks of age and 1.50 ± 0.23, p = 0.09 at 28 weeks of age in $2^{-\Delta\Delta Ct}$ analysis; N = 5-6; figure 3.10).

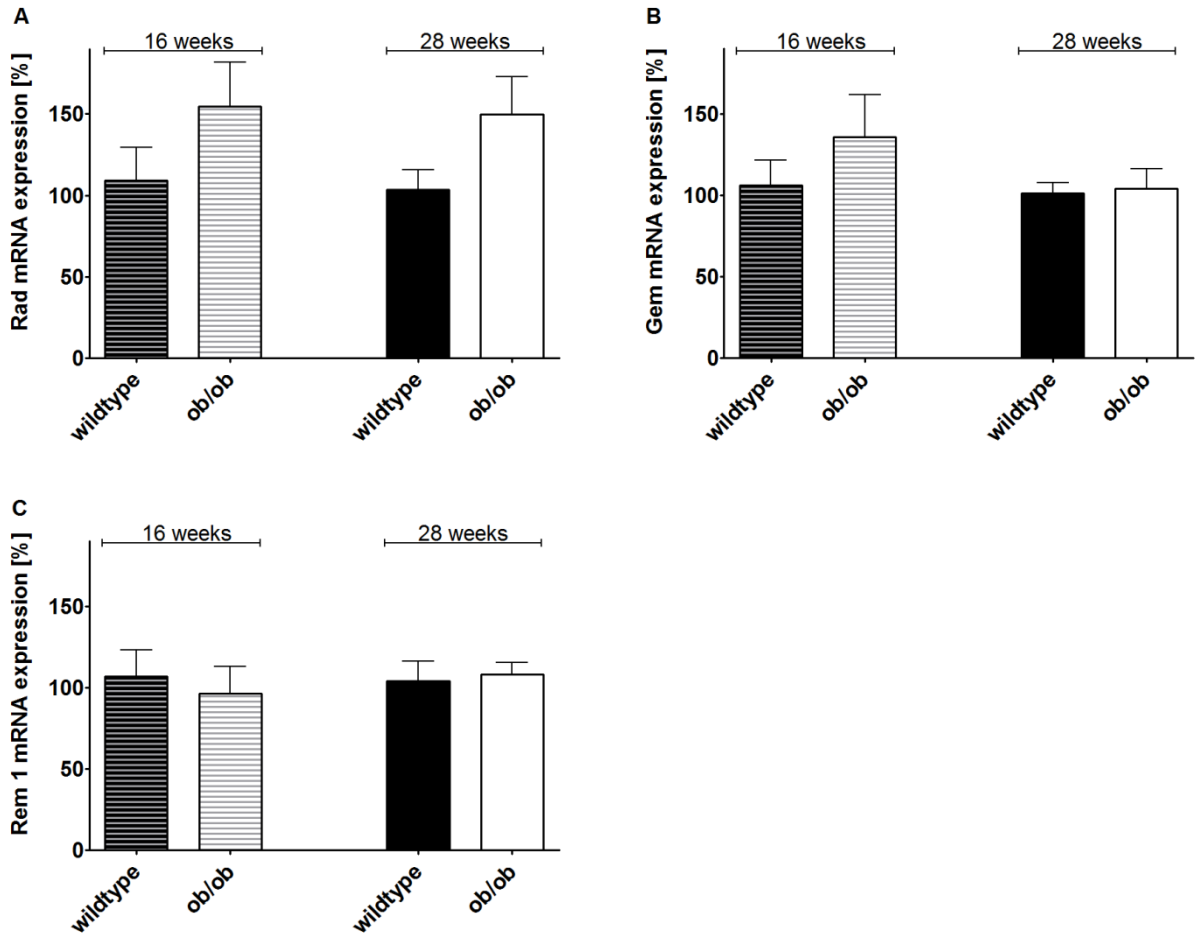

Figure 3.10 **Ventricular expression of RGK mRNA in ob/ob mice:** RGK mRNA was not significantly altered in ventricles of ob/ob and wt mice at both ages (N = 5-6 mice per group).

As outlined in figure 3.11, ventricular expression of $Ca_v1.2$ mRNA was significantly reduced in ventricles of 28 week old ob/ob mice (0.76 ± 0.65-0.93 in REST-2009© analysis; N = 5-6).

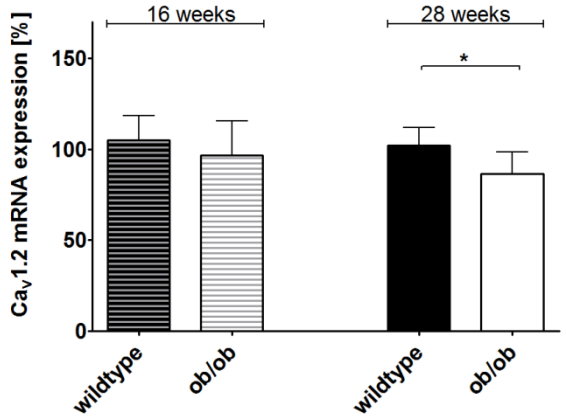

Figure 3.11 **Ventricular expression of $Ca_v1.2$ mRNA in ob/ob mice:** in 28 week old ob/ob mice ventricular expression of $Ca_v1.2$ mRNA was significantly reduced (N = 5-6 animals per group; * = $p < 0.05$ vs. age-matched wt in REST-2009© analysis).

Since $Ca_vß$-subunits ($Ca_vß1$, $Ca_vß2$, $Ca_vß3$) are involved in LTCC expression and function their expression levels were investigated, too. qRT-PCR analysis revealed a significant downregulation of $Ca_vß1$- and $Ca_vß2$- but not $Ca_vß3$-subunit mRNA in ventricles of 16 week old ob/ob mice ($Ca_vß1$ = 0.57 ± 0.30-0.82, $Ca_vß2$ = 0.47 ± 0.32-0.74 in REST-2009© analysis; N = 5-6). At 28 weeks of age all $Ca_vß$-subunits were significantly downregulated compared to age-matched wt ($Ca_vß1$ = 0.54 ± 0.35-0.90, $Ca_vß2$ = 0.68 ± 0.52-0.86, $Ca_vß3$ = 0.63 ± 0.38-0.90 in REST-2009© analysis; N = 5-6; figure 3.12).

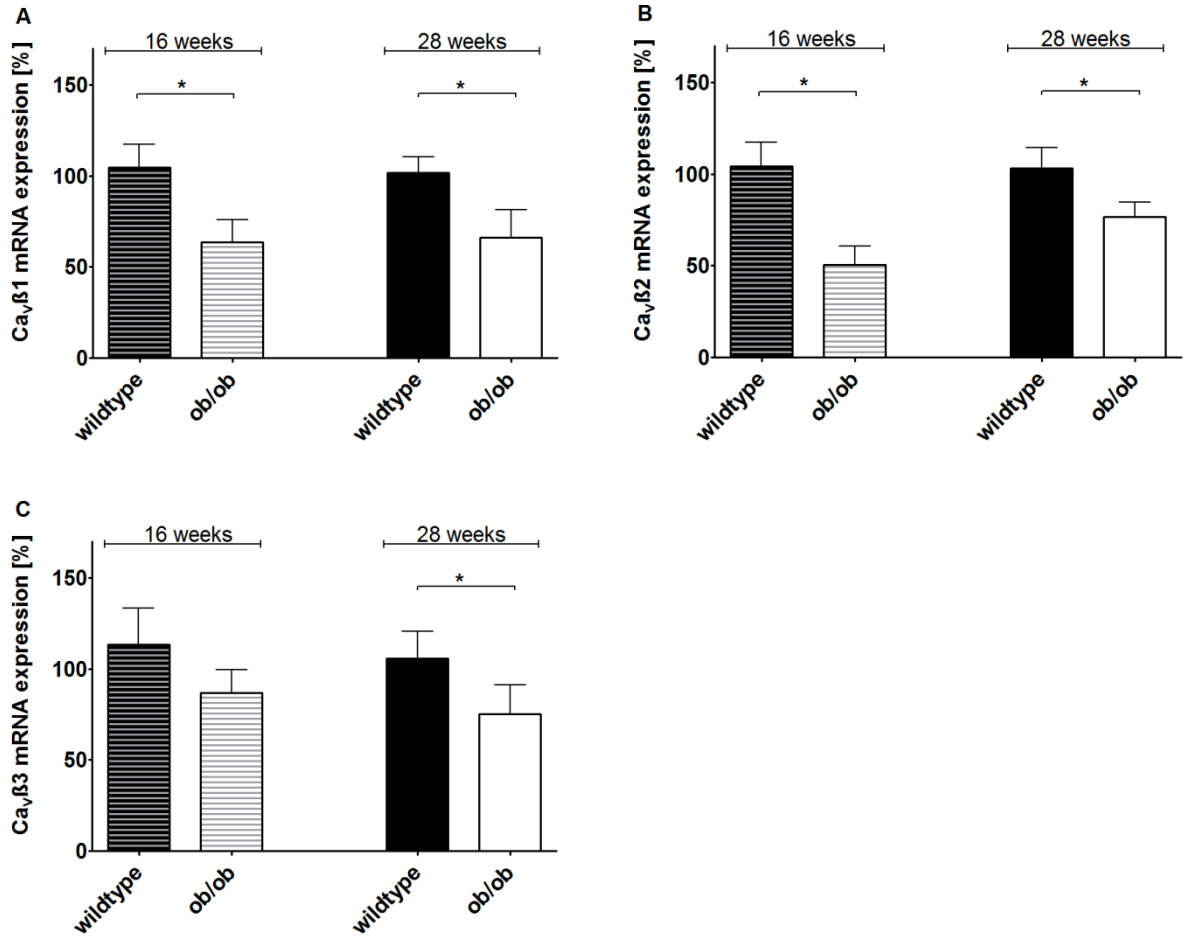

Figure 3.12 **Ventricular expression of the Ca_vß-subunits mRNA in ob/ob mice:** qRT-PCR analysis detected a significant downregulation of Ca_vß1- and Ca_vß2- but not Ca_vß3-subunits in ventricles of 16 week old ob/ob mice. At 28 weeks of age all Ca_vß-subunits were significantly downregulated compared to age-matched wt (N = 5-6 animals per group; * = $p < 0.05$ vs. age-matched wt in REST-2009© analysis).

3.4 Rad-k.o. mice

3.4.1 Blood glucose value, body weight, ventricle weight and ventricle-to-body weight ratio

Rad-k.o. mice' (non-fasting) blood glucose was significantly lower compared to wt animals (Rad-k.o.: 140 ± 4 mg/dl at 16 weeks, N = 27 and 151 ± 5 mg/dl, N = 49 at 28 weeks vs. wt: 158 ± 5 mg/dl, N = 58 at 16 weeks and 168 ± 6 mg/dl, N = 41 at 28 weeks; figure 3.13 (A)). Young Rad-k.o. mice weighed significantly more than age-matched wt animals (Rad-k.o.: 26.9 ± 0.7 g, N = 27 vs. wt: 24.4 ± 0.5 g, N = 62; figure 3.13 (B)). As demonstrated in figure 3.13 (C), 28 week old Rad-k.o. mice had significantly lower ventricle weights compared to age-matched wt littermates (Rad-k.o.: 120.9 ± 8.3 mg, N = 21 vs. wt: 142.7 ± 6.4 mg, N = 21). Rad-k.o. mice' ventricle-to-body

weight ratios thus were significantly decreased compared to wt animals at both ages (Rad-k.o.: 4.6 ± 0.1 mg/g at 16 and 28 weeks, N = 21 each vs. wt: 5.4 ± 0.2 mg/g, N = 36 at 16 weeks and 5.2 ± 0.2 mg/g, N = 21 at 28 weeks, figure 3.13 (D)).

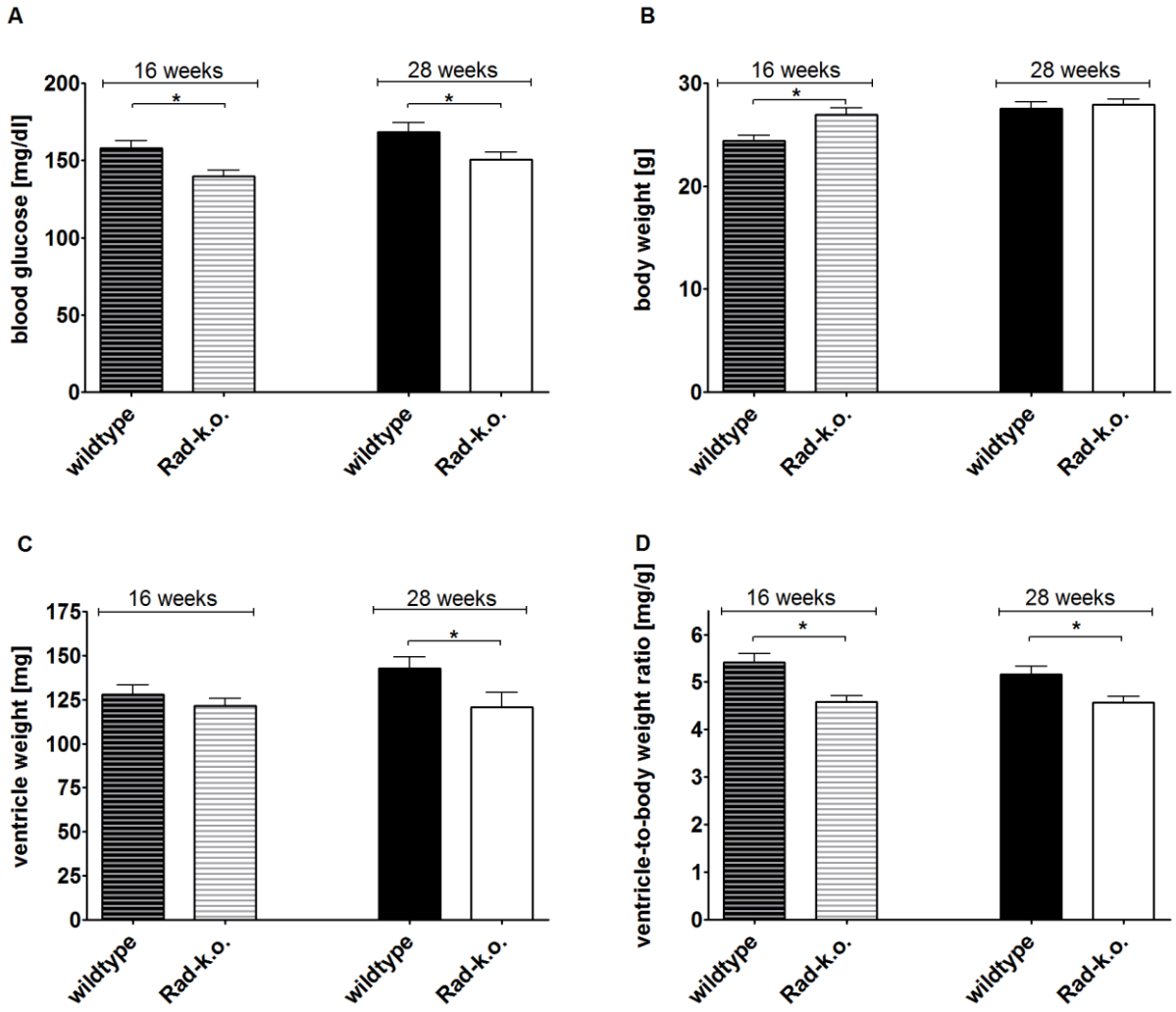

Figure 3.13 **Blood glucose, body weight, ventricle weight and ventricle-to-body weight ratio of Rad-k.o. mice:** Rad-k.o. mice had significantly lower blood glucose values compared to wt (A). Young Rad-k.o. mice weighed significantly more than age-matched wt (B). Ventricle weights of older Rad-k.o. mice were significantly lower in comparison to wt (C). Ventricle-to-body weight ratios were significantly decreased in Rad-k.o. mice at both ages investigated (D) (N = 27-62 for (A, B); N = 21-36 for (C, D); * = $p < 0.05$ vs. age-matched wt in REST-2009© analysis).

3.4.2 Functional properties of cardiac whole-cell LTCC currents

At both ages investigated mean cell capacitances of cardiomyocytes from Rad-k.o. and wt mice were similar (appendix, chapter 8.3.1). Therefore, experiments appeared to be comparable and cellular hypertrophy was excluded. Only recordings of stable-patched cells were analyzed. Representative I/V recordings for Rad-k.o. mice are illustrated in figure 3.14.

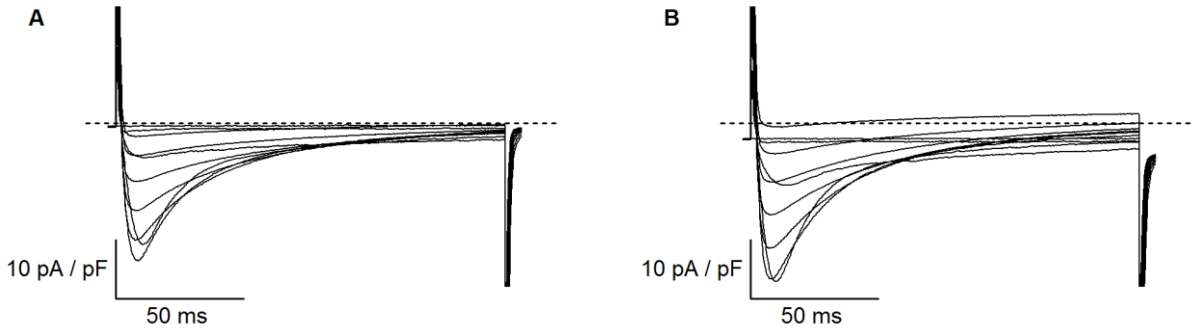

Figure 3.14 **Example of representative and good quality I/V recordings for Rad-k.o. mice** at 16 (A) and 28 (B) weeks of age.

As depicted in figure 3.15, the knockout of Rad protein caused the expected increase in whole-cell Ca^{2+} current density compared to wt mice (Rad-k.o.: -20.12 ± 1.49 pA/pF, n = 5 vs. wt: -10.92 ± 0.90 pA/pF, n = 17 at 16 weeks of age and Rad-k.o.: -21.58 ± 5.05 pA/pF, n = 2 vs. wt: -8.91 ± 0.54 pA/pF, n = 13 at 28 weeks of age). At both ages $V_{0.5act}$ was significantly shifted to the left and the slope factor was significantly decreased ($V_{0.5act}$ at 16 weeks: -14.74 ± 1.33 mV for Rad-k.o. mice vs. -8.69 ± 1.06 mV for wt mice; $V_{0.5act}$ at 28 weeks: -16.13 ± 0.08 mV for Rad-k.o. mice vs. -7.51 ± 0.96 mV for wt mice; slope factor at 16 weeks: 3.97 ± 0.22 for Rad-k.o. mice vs. 5.05 ± 1.02 for wt mice; slope factor at 28 weeks: 3.37 ± 0.53 for Rad-k.o. mice vs. 5.01 ± 0.5 for wt mice).

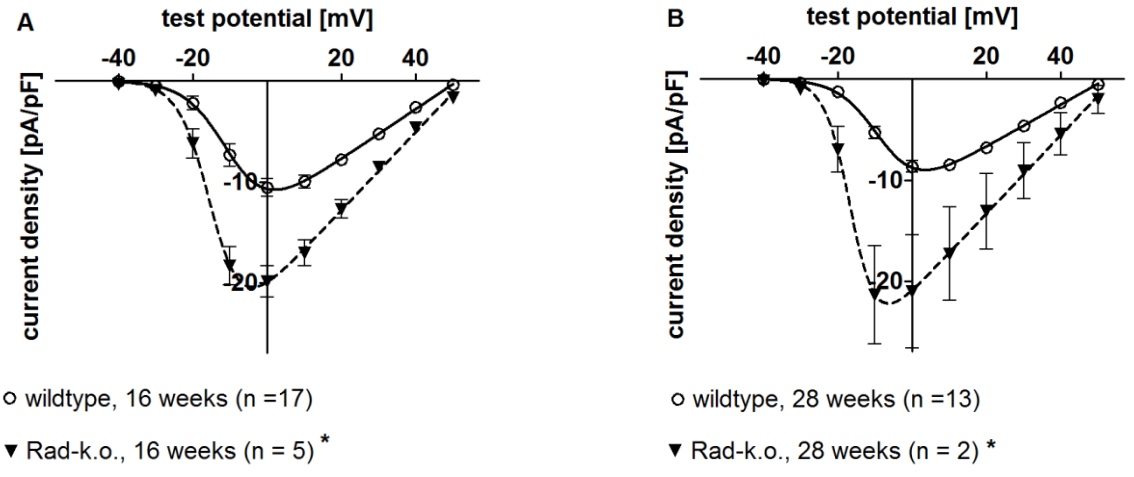

Figure 3.15 **Current density-voltage relationships of Rad-k.o. mice:** the knockout of Rad protein caused the expected increase in whole-cell Ca^{2+} current density at both ages (n = number of patched cells; number of mice: N = 5-10 for wt, N = 2-3 for Rad-k.o., * = $p < 0.05$ vs. age-matched wt).

Whole-cell LTCCs of 16 week old Rad-k.o. mice showed a significantly faster time-dependent inactivation at -10 mV, but significantly slower kinetics at 40 mV (figure 3.16 (A)). Time-dependent inactivation was significantly faster at 0 mV in cells of 28 week old Rad-k.o. mice (figure 3.16 (B)).

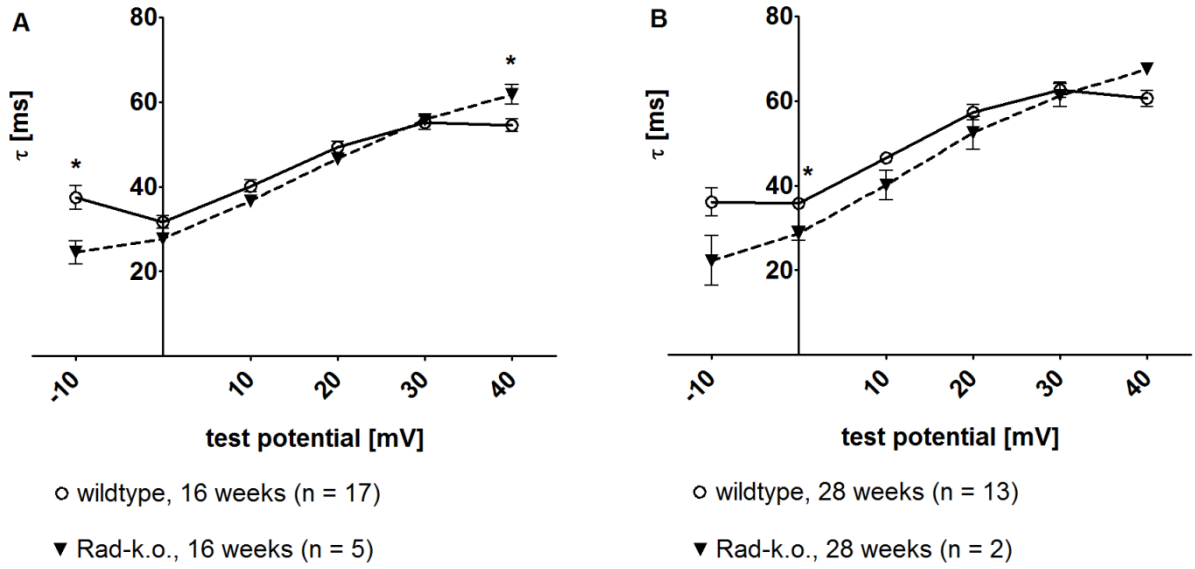

Figure 3.16 **Time-dependent inactivation properties of Rad-k.o. mice:** whole-cell LTCCs of 16 week old Rad-k.o. mice showed a significantly slowed time-dependent inactivation at -10 mV and significantly faster kinetics at 40 mV (A). Time-dependent inactivation was significantly faster at 0 mV in cells of 28 week old Rad-k.o. mice (B) (n = number of patched cells; number of mice: N = 5-10 for wt, N = 2-3 for Rad-k.o.; * = $p < 0.05$ vs. age-matched wt).

Voltage-dependent inactivation (slope factor) of whole-cell LTCCs differed significantly in 28 week old Rad-k.o. mice compared to age-matched wt animals (Rad-k.o.: 3.76 ± 0.28, n = 3 vs. wt: 4.70 ± 0.20, n = 9; figure 3.17 (B)).

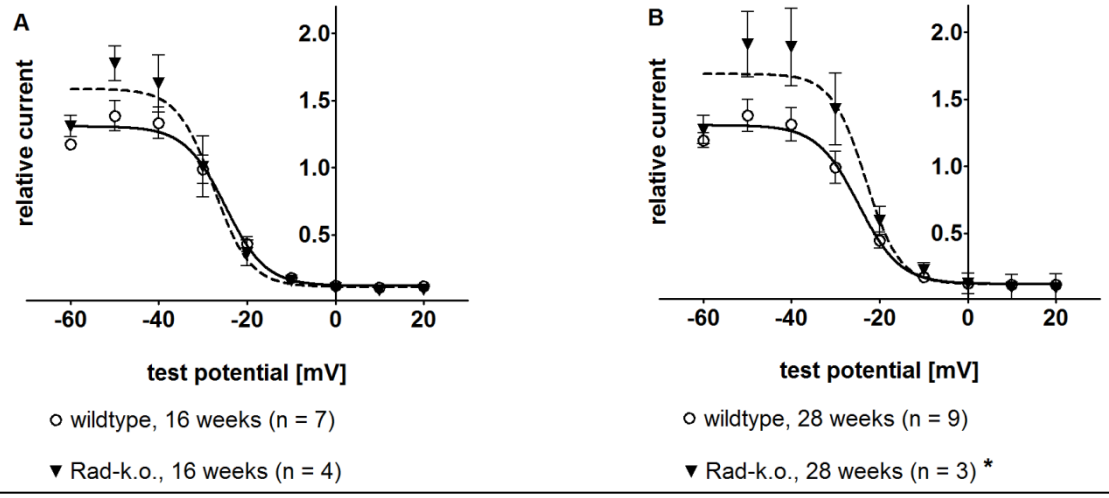

Figure 3.17 **Steady-state inactivation properties of Rad-k.o. mice:** 16 week old Rad-k.o. mice showed no significant change in steady-state inactivation compared to wt (A). In older mice voltage-dependent inactivation differed significantly compared to age-matched wt (B) (n = number of patched cells; number of mice: N = 4 for wt, N = 3 for Rad-k.o.; * = $p < 0.05$ vs. age-matched wt).

As illustrated in figure 3.18 (A), recovery from inactivation was altered in Rad-k.o. mice at 16 weeks of age. Tau as well as the half-time values were significantly augmented compared to age-matched wt (tau: 206.20 ± 27.75 and half-time: 142.89 ± 19.24 for Rad-k.o. mice vs. tau: 150.28 ± 8.87 and half-time: 104.17 ± 6.15 for wt mice). The relative current after 375 ms of recovery (I2/I1) was significantly decreased (Rad-k.o.: 0.70 ± 0.06 vs. wt: 0.81 ± 0.02). At 28 weeks of age recovery from inactivation was not significantly altered (figure 3.18 (B)).

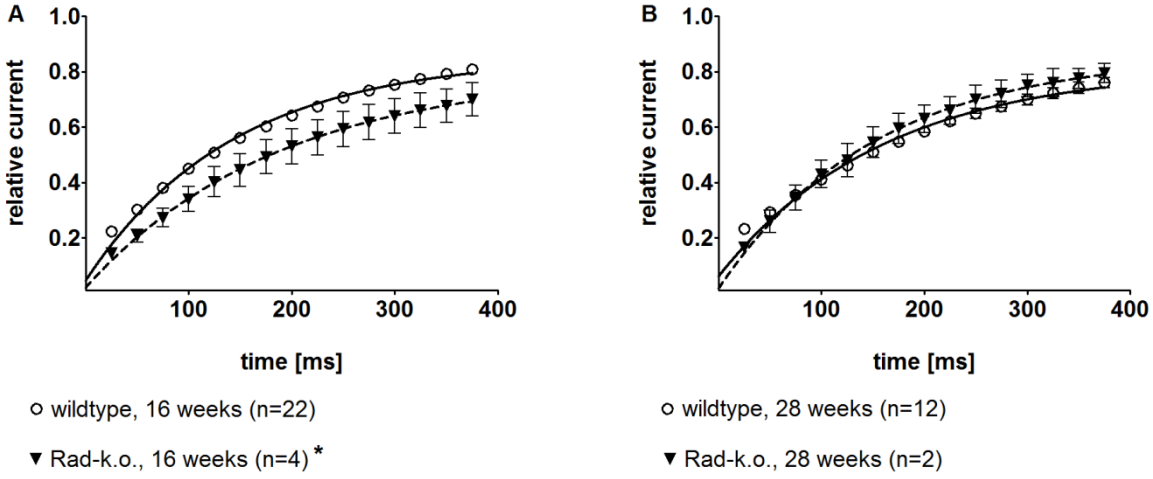

Figure 3.18 **Recovery from inactivation properties of Rad-k.o. mice:** the recovery from inactivation was significantly altered in young Rad-k.o. mice (A). At 28 weeks of age recovery from inactivation was not significantly altered (B). (n = number of patched cells; number of mice: N = 5-8 for wt, N = 2-3 for Rad-k.o.; * = $p < 0.05$ vs. age-matched wt).

3.4.3 Cardiac mRNA expression levels

As expected Rad mRNA was not detectable in ventricles of Rad-k.o. mice (see also appendix). Gem was upregulated about twofold at both ages (1.92 ± 1.29-2.82 at 16 weeks of age and 2.13 ± 1.74-2.67 at 28 weeks of age in REST-2009© analysis; N = 6; figure 3.19 (A)). Analysis of Rem 1 detected an increased expression in ventricles of 28 week old Rad-k.o. mice (1.28 ± 1.05-1.67 in REST-2009© analysis; N = 6; figure 3.19 (B)).

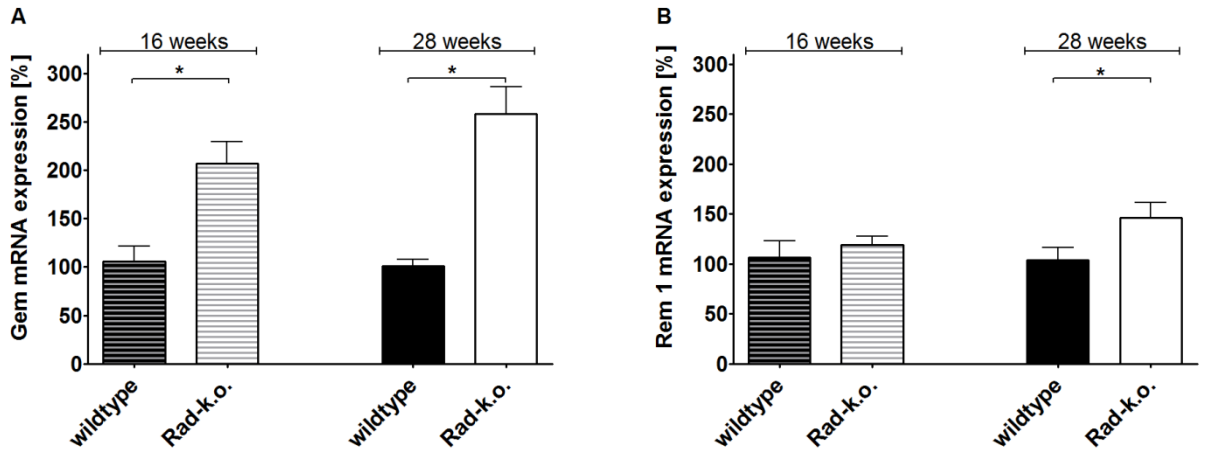

Figure 3.19 **Ventricular expression of RGK mRNA in Rad-k.o. mice:** in Rad-k.o. mice Gem was upregulated about twofold at both ages (A). Analysis of Rem 1 detected an increased expression in ventricles of 28 week old Rad-k.o. mice (B) (N = 6 animals per group; * = $p < 0.05$ vs. age matched wt in REST-2009© analysis).

$Ca_v1.2$ mRNA expression was significantly reduced by nearly 50% in hearts of Rad-k.o. mice at the age of 28 weeks (0.50 ± 0.35-0.68, $p < 0.05$ in REST-2009©; N = 6; figure 3.20).

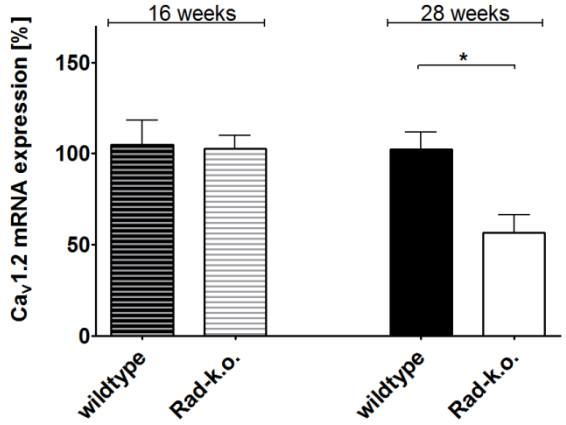

Figure 3.20 **Ventricular expression of $Ca_v1.2$ mRNA in Rad-k.o. mice:** $Ca_v1.2$ mRNA was significantly reduced by nearly 50% in hearts of Rad-k.o. mice at the age of 28 weeks (N = 6 animals per group; * = $p < 0.05$ vs. age matched in REST-2009© analysis).

At both ages $Ca_vß2$-subunit mRNA was significantly reduced in Rad-k.o. mice ventricles compared to wt animals (0.69 ± 0.49-1.03 at 16 weeks of age and 0.40 ± 0.29-0.56 at 28 weeks of age in REST-2009© analysis; N = 6; figure 3.21 (B)). The expression of the other $Ca_vß$-subunits was not significantly altered (figure 3.21 (A,C)).

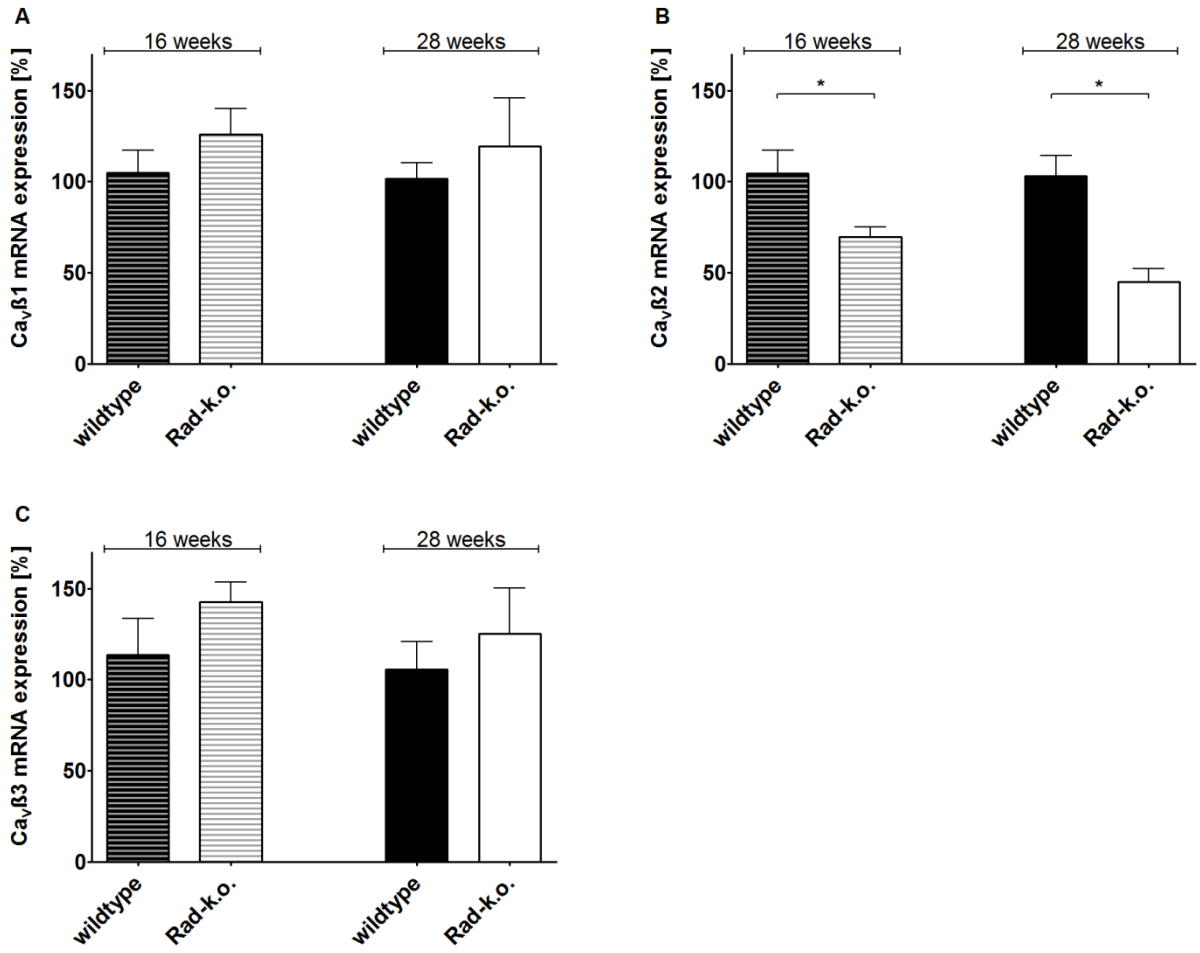

Figure 3.21 **Ventricular expression of the Ca_vß-subunits mRNA in Rad-k.o. mice:** at both ages the Ca_vß2-subunit mRNA was significantly reduced in Rad-k.o. mice ventricles compared to wt animals (B). The expression of the other Ca_vß-subunits was not significantly altered (A, C). (N = 6 animals per group; * = $p < 0.05$ vs. age matched in REST-2009© analysis).

3.5 Ob/ob x Rad-k.o. mice

3.5.1 Blood glucose value, body weight, ventricle weight and ventricle-to-body weight ratio

As demonstrated in figure 3.22 (A), ob/ob x Rad-k.o. mice had significantly increased (non-fasting) blood glucose levels compared to wt animals at both ages investigated (ob/ob x Rad-k.o.: 291 ± 26 mg/dl, N = 25 at 16 weeks and 276 ± 43 mg/dl, N = 9 at 28 weeks vs. wt: 158 ± 5 mg/dl, N = 58 at 16 weeks and 168 ± 6 mg/dl, N = 41 at 28 weeks). In both age groups ob/ob x Rad-k.o. mice‘ body weight was at least doubled compared to wt mice (ob/ob x Rad-k.o.: 51.1 ± 0.9 g, N = 25 at 16 weeks and 59.7 ± 1.6 g, N = 9 at 28 weeks vs. wt: 24.4 ± 0.5 g, N = 62 at 16 weeks and 27.6 ± 0.6 g, N = 42 at 28 weeks, figure 3.22 (B)). Young ob/ob x Rad-k.o. mice

weighed significantly less than older mice of the same genotype. Ventricle weights of 28 week old ob/ob x Rad-k.o. mice (170.8 ± 7.9 mg, N = 8) were significantly increased compared to age-matched wt (142.7 ± 6.4 mg, N = 21) and to younger animals of the same genotype (136.8 ± 4.7 mg, N = 16), as depicted in figure 3.22 (C). Similar to ob/ob mice, ob/ob x Rad-k.o. mice had significantly decreased ventricle-to-body weight ratios compared to wt, but were similar in this regard when comparing young and old ob/ob x Rad-k.o. mice (figure 3.22 (D)). The decreased ratios were attributable to the increased body weight.

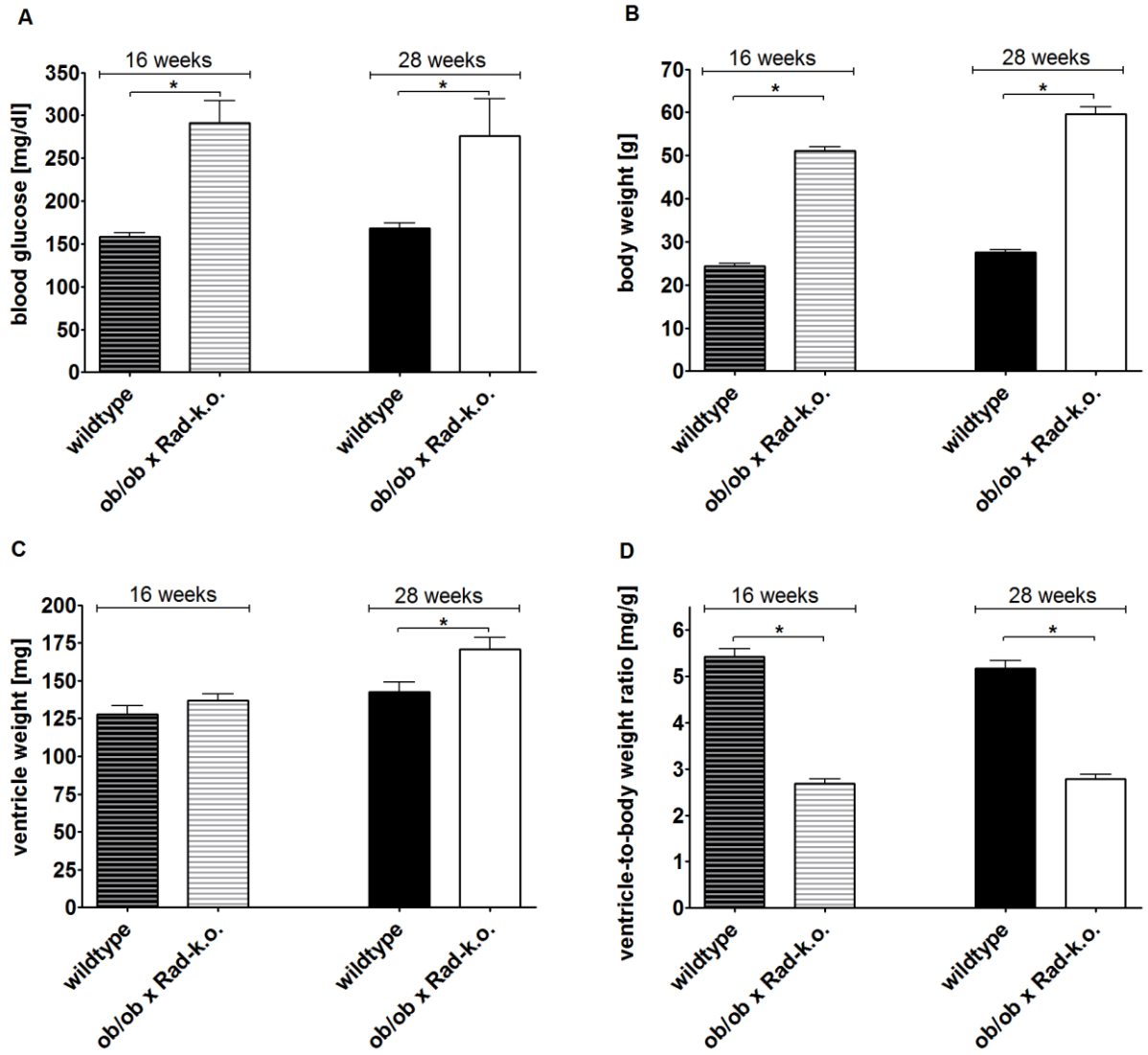

Figure 3.22 **Blood glucose, body weight, ventricle weight and ventricle-to-body weight ratio of ob/ob x Rad-k.o. mice:** ob/ob x Rad-k.o. mice had significantly higher blood glucose values compared to wt (A). Body weights of ob/ob x Rad-k.o. mice were (nearly) twice than that of wt (B). Ventricle weights of old ob/ob x Rad-k.o. were significantly elevated compared to wt (C). Ventricle-to-body weight ratios were significantly decreased in ob/ob x Rad-k.o. mice. This was most likely due to the increased body weight (D) (N = 9-62 for (A, B); N = 8-36 for (C, D); * = $p < 0.05$ vs. age-matched wt).

3.5.2 Functional properties of cardiac whole-cell LTCC currents in young mice

Cardiomyocytes isolated from 16 week old ob/ob x Rad-k.o. and wt mice had similar mean cell capacitances at both ages investigated (appendix, chapter 8.3.1). Therefore, experiments were comparable and cellular hypertrophy was excluded. Only recordings of stable-patched cells were analyzed. An I/V recording representative for ob/ob x Rad-k.o. mice can be seen in figure 3.23.

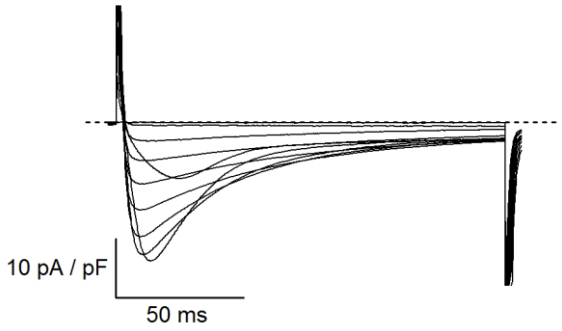

Figure 3.23 **Example of a representative and good quality I/V recording for ob/ob x Rad-k.o. mice** at 16 weeks of age.

Compared to age-matched wt animals ob/ob mice lacking Rad showed a significant increase in whole-cell Ca^{2+} current density (ob/ob x Rad-k.o.: -21.48 ± 1.10 pA/pF, n = 5 vs. wt: -10.92 ± 0.90 pA/pF, n =17; figure 3.24). This increase was similar to age-matched Rad-k.o. mice with a wt background (Rad-k.o.: -20.12 ± 1.49 pA/pF, n = 5). In young ob/ob x Rad-k.o. mice $V_{0.5act}$ was significantly shifted to the left and the slope factor was significantly decreased compared to age-matched wt ($V_{0.5act}$: -17.06 ± 1.71 mV for ob/ob x Rad-k.o. mice vs. -8.69 ± 1.06 mV for wt mice; slope factor: 3.65 ± 0.30 for ob/ob x Rad-k.o. mice vs. 5.05 ± 1.02 for wt mice).

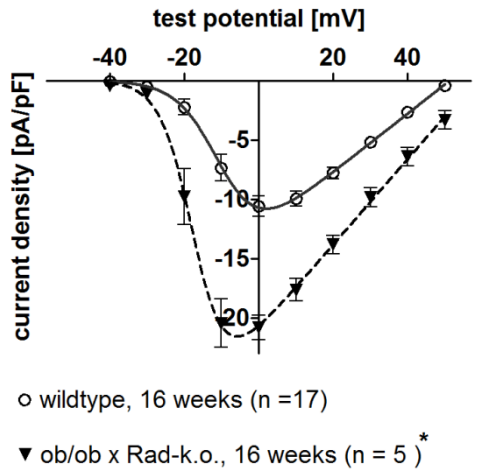

Figure 3.24 **Current density-voltage relationship of ob/ob x Rad-k.o. mice:** ob/ob x Rad-k-o. mice showed the expected significant increase in whole-cell Ca^{2+} current density (n = number of patched cells; number of mice: N = 5-10 for wt, N = 3 for ob/ob x Rad-k.o.; * = $p < 0.05$ vs. age-matched wt).

Time-dependent inactivation was similar in ventricular myocytes of ob/ob x Rad-k.o. and wt mice (figure 3.25).

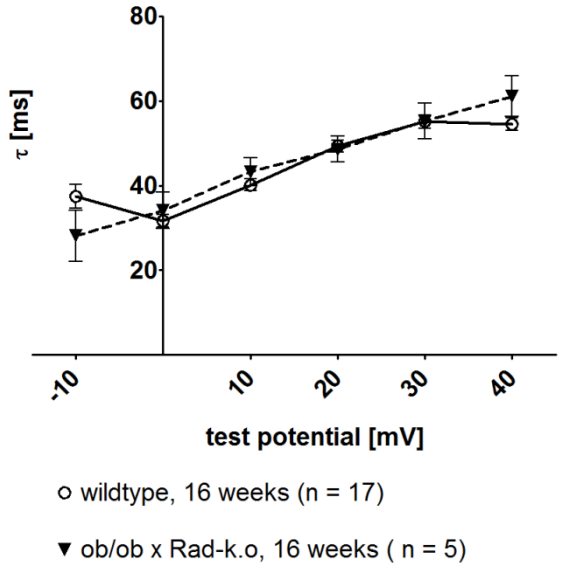

Figure 3.25 **Time-dependent inactivation properties of ob/ob x Rad-k.o. mice:** time-dependent inactivation was comparable in ventricular myocytes of ob/ob x Rad-k.o. and wt mice (n = number of patched cells; number of mice: N = 5-10 for wt, N = 3 for ob/ob x Rad-k.o.).

Voltage-dependent inactivation of 16 week old ob/ob x Rad-k.o. mice was similar to age-matched wt animals (figure 3.26).

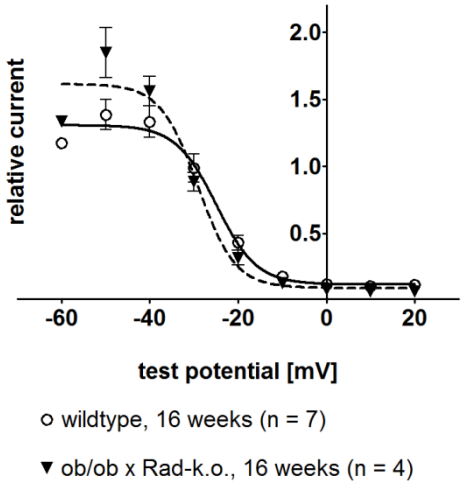

Figure 3.26 **Steady-state inactivation properties of ob/ob x Rad-k.o. mice:** voltage-dependent inactivation was comparable in ob/ob x Rad-k.o. and wt mice (n = number of patched cells; number of mice: N = 4 for wt, N = 3 for ob/ob x Rad-k.o.).

Recovery from inactivation was altered in 16 week old ob/ob x Rad-k.o. mice. Tau as well as the half-time value were significantly augmented compared to age-matched wt (tau: 224.45 ± 13.70 and half-time: 155.58 ± 9.84 for ob/ob x Rad-k.o. mice vs. tau: 150.28 ± 8.87 and half-time: 104.17 ± 6.15 for wt mice). The relative current after 375 ms of recovery (I2/I1) was significantly decreased (ob/ob x Rad-k.o.: 0.70 ± 0.03 vs. wt: 0.81 ± 0.02; figure 3.27).

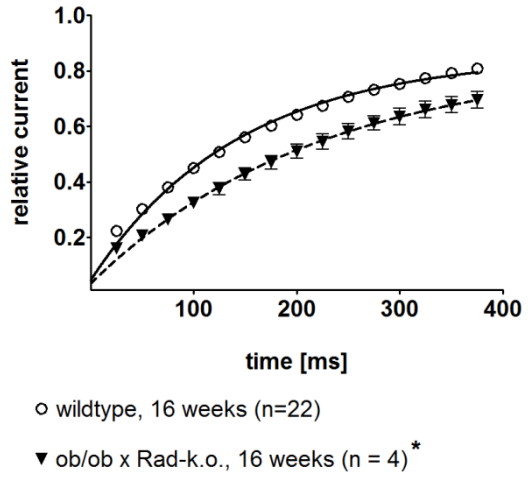

Figure 3.27 **Recovery from inactivation properties of ob/ob x Rad-k.o. mice:** the recovery from inactivation was significantly altered in young ob/ob x Rad-k.o. mice. (n = number of patched cells; number of mice: N = 5-8 for wt, N = 2 for ob/ob x Rad-k.o.).

3.6 IRS 2-k.o. mice

3.6.1 Blood glucose value, body weight, ventricle weight and ventricle-to-body weight ratio

As illustrated in figure 3.28 (A), IRS 2-k.o. mice showed significantly higher (non-fasting) blood glucose values compared to wt animals at both ages investigated (IRS 2-k.o.: 207 ± 10 mg/dl, n = 62 at 16 weeks and 239 ± 22 mg/dl at 28 weeks, N = 30 vs. wt: 158 ± 5 mg/dl, N = 58 at 16 weeks and 168 ± 6 mg/dl, N = 41 at 28 weeks). Body weight, ventricle weight as well as ventricle-to-body weight ratio of IRS 2-k.o. and wt mice were similar (figure 3.28 (B-D)).

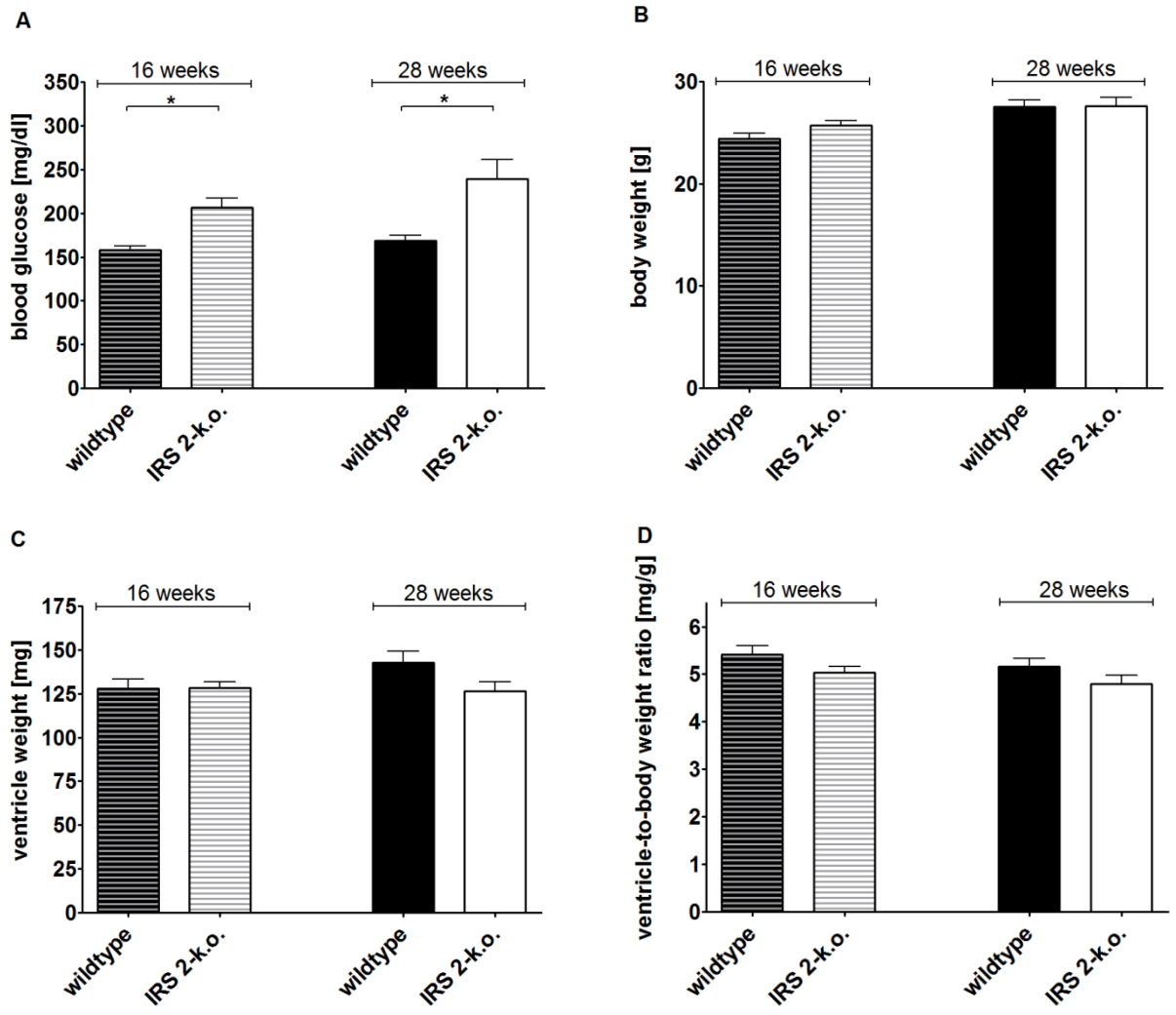

Figure 3.28 **Blood glucose, body weight, ventricle weight and ventricle-to-body weight ratio of IRS 2-k.o. mice:** IRS 2-k.o. mice had significantly higher blood glucose values compared to wt animals (A). Body weights, ventricle weights and ventricle-to-body weight ratios were similar in IRS 2-k.o. and wt mice (B-D) (N = 30-62 for (A, B); N = 21-36 for (C, D); * = $p < 0.05$ vs. age-matched wt).

3.6.2 Functional properties of cardiac whole-cell LTCC currents

Cardiomyocytes isolated from IRS 2-k.o. and wt mice had similar mean cell capacitances at both ages investigated (appendix, chapter 8.3.1). Therefore, experiments were comparable and there was no hint towards cellular hypertrophy. Only recordings of stable-patched cells were analyzed. Representative I/V recordings for IRS 2-k.o. mice are demonstrated in figure 3.29.

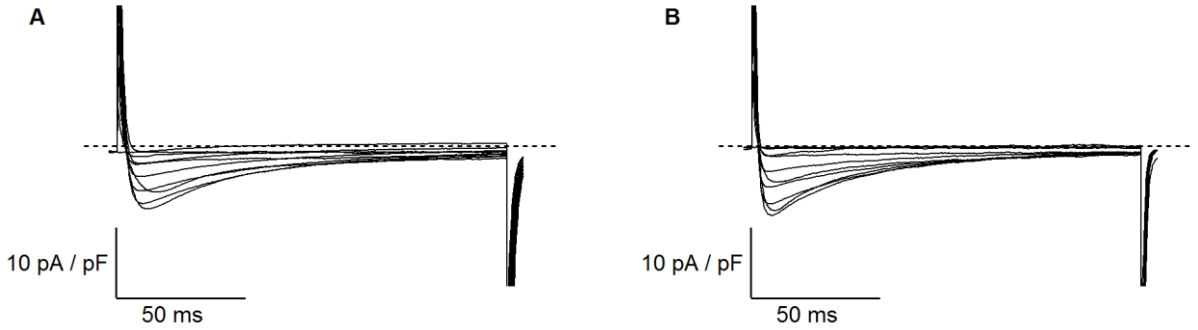

Figure 3.29 **Example of representative and good quality I/V recordings for IRS 2-k.o. mice** at 16 (A) and 28 (B) weeks of age.

The analysis of current density-voltage relationship revealed that the maximum whole-cell Ca^{2+} current density was significantly reduced in IRS 2-k.o. mice at the age of 16 weeks compared to age-matched wt animals (IRS 2-k.o.: -7.79 ± 0.79 pA/pF, n = 11 vs. wt: -10.92 ± 0.90 pA/pF, n =17; figure 3.30 (A)). Compared to younger IRS 2-k.o. mice whole-cell Ca^{2+} current density was increased at an age of 28 weeks and no longer significantly different to age-matched control (IRS 2-k.o.: -11.22 ± 1.27 pA/pF, n = 11 vs. wt: -8.91 ± 0.54 pA/pF, n = 13; figure 3.30 (B)). Moreover, $V_{0.5act}$ was significantly shifted to the left in recordings of 28 week old mice (IRS 2-k.o.: -10.88 ± 0.89 mV vs. wt: -7.51 ± 0.96 mV).

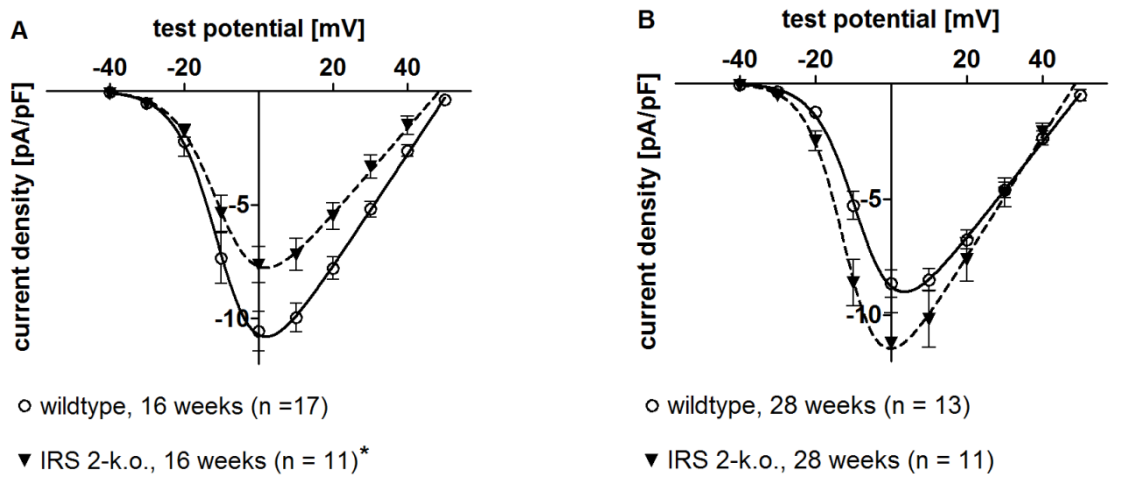

Figure 3.30 **Current density-voltage relationships of IRS 2-k.o. mice:** maximum whole-cell Ca^{2+} current density of 16 week old IRS 2-k.o. mice was significantly decreased compared to wt (A). At 28 weeks of age Ca^{2+} current density was no longer different to wt and $V_{0.5act}$ was significantly shifted to the left (B) (n = number of patched cells; number of mice: N = 5-10 for wt, N = 4-7 for IRS 2-k.o.; * = $p < 0.05$ vs. age-matched wt).

As illustrated in figure 3.31 (A), time-dependent inactivation was similar in 16 week old IRS 2-k.o. and wt mice. At 28 weeks of age IRS 2-k.o. mice revealed significantly faster inactivation kinetics in the range of 10 mV to 40 mV (figure 3.31 (B)).

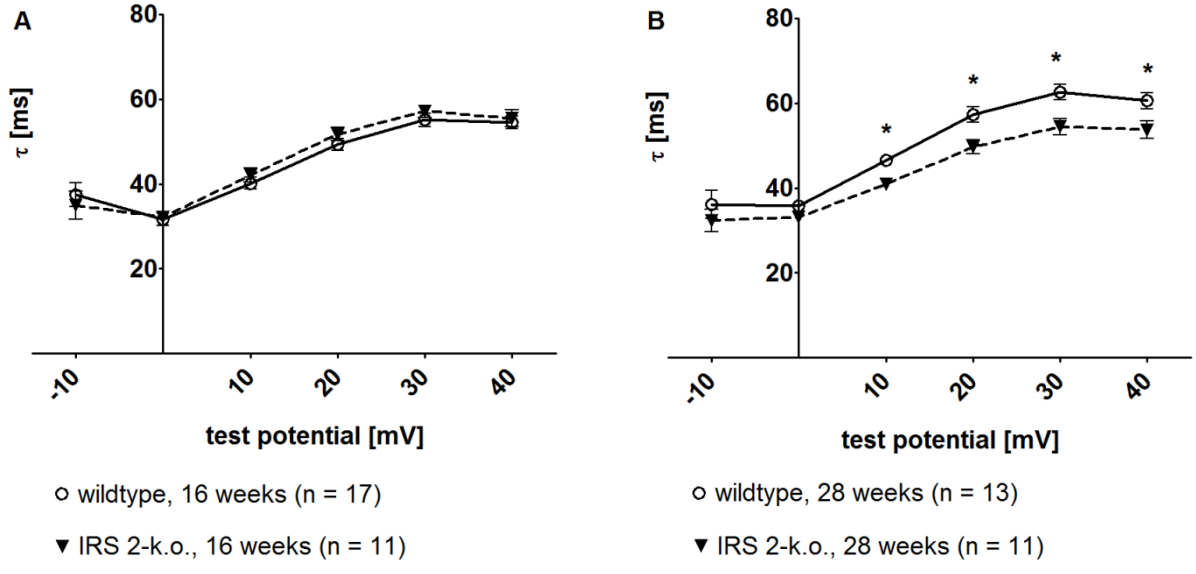

Figure 3.31 **Time-dependent inactivation properties of IRS 2-k.o. mice:** at 16 weeks of age no significant changes could be detected between IRS 2-k.o. and wt mice (A). At 28 weeks of age whole-cell LTCCs of IRS 2-k.o. mice revealed significantly faster inactivation kinetics in the range of 10 mV to 40 mV (B) (n = number of patched cells; number of mice: N = 5-10 for wt, N = 4-7 for IRS 2-k.o.; * = $p < 0.05$ vs. age-matched wt).

Voltage-dependent inactivation was comparable in 16 week old IRS 2-k.o. and wt mice (figure 3.32 (A)). In 28 week old IRS 2-k.o. mice $V_{0.5inact}$ was significantly shifted to more negative potentials (IRS 2-k.o.: -29.23 ± 1.06 mV, n = 4 vs. wt: -25.31 ± 0.84 mV, n = 9; figure 3.32 (B)).

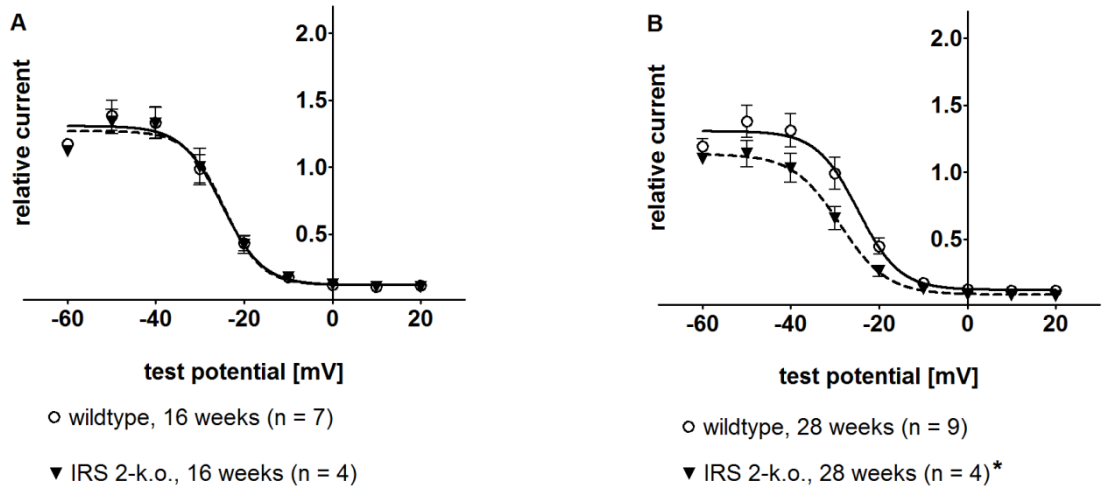

Figure 3.32 **Steady-state inactivation properties of IRS 2-k.o. mice:** at 16 weeks of age no significant changes could be detected between IRS 2-k.o. and wt mice (A). $V_{0.5inact}$ of 28 week old IRS 2-k.o. animals was significantly shifted to more negative potentials (B) (n = number of patched cells; number of mice: N = 4 for wt, N = 3 for IRS 2-k.o.).

At both ages, investigated recovery from inactivation revealed no significant differences between IRS 2-k.o. and wt mice. The relative current after 375 ms of recovery reached mean values in the range of 0.75-0.87 (figure 3.33).

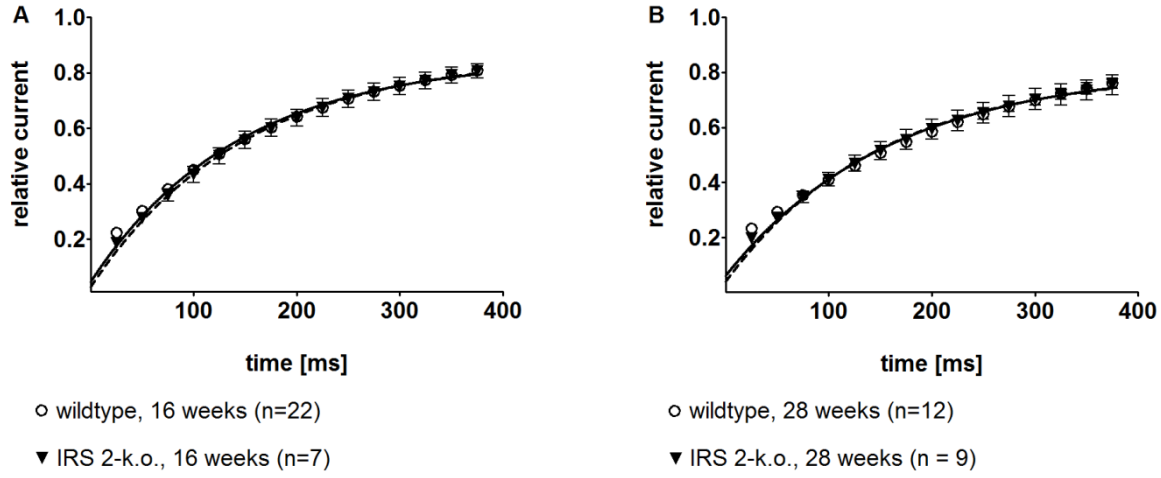

Figure 3.33 **Recovery from inactivation properties of IRS 2-k.o. mice:** recovery from inactivation revealed no significant differences between IRS 2-k.o. and wt mice at both ages (n = number of patched cells; number of mice: N = 5-8 for wt, N = 5-6 for IRS 2-k.o.).

3.6.3 Cardiac mRNA expression levels

Rad mRNA was significantly upregulated about twofold in ventricles of 16 week old IRS 2-k.o. mice compared to age-matched wt (2.01 ± 1.24-3.37 in REST-2009© analysis; N = 5-6; figure 3.34 (A)), while its expression was unchanged at an age of 28 weeks. At both ages, the mRNA expression of Gem and Rem 1 was not significantly altered compared to age-matched wt (figure 3.34 (B, C)).

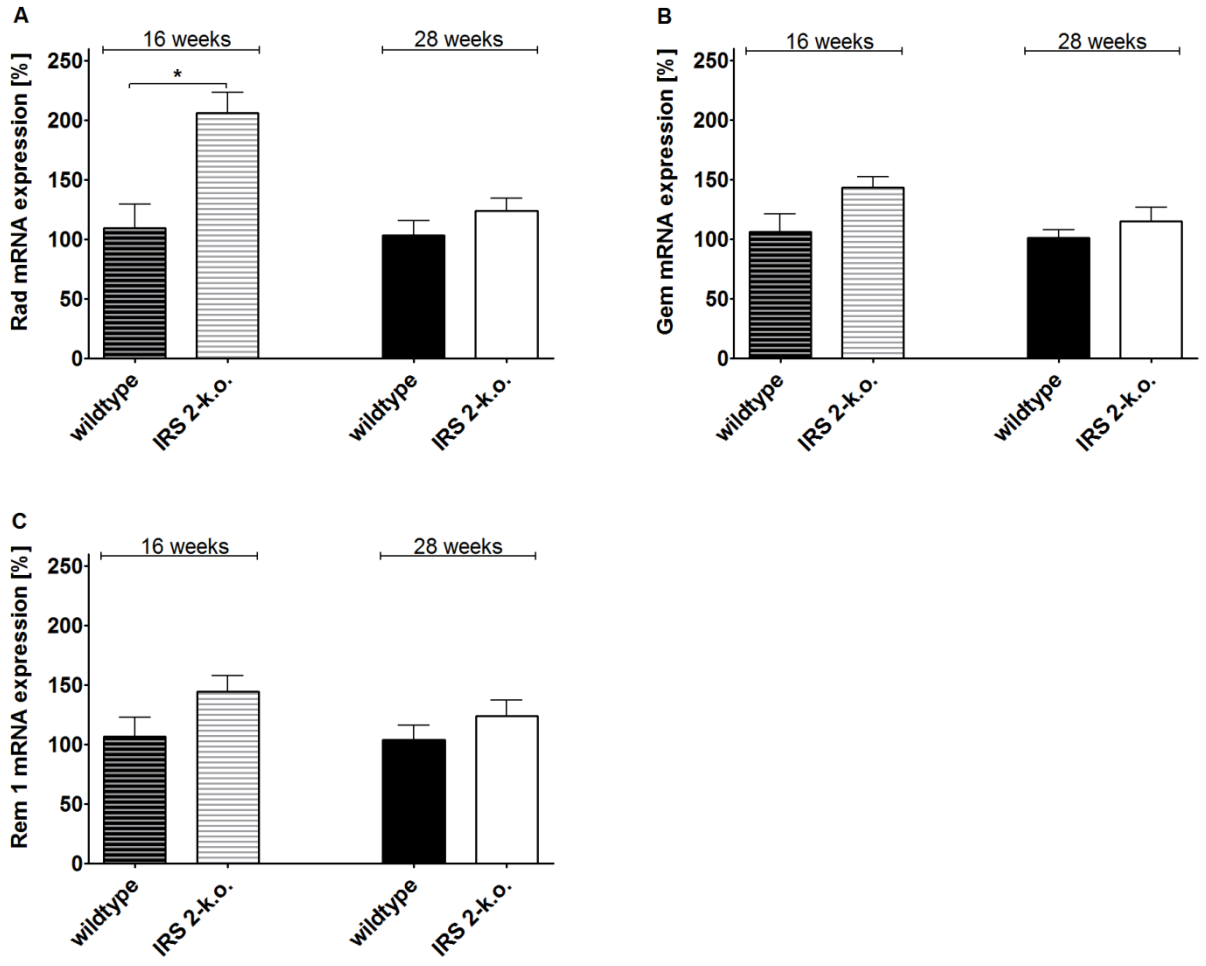

Figure 3.34 **Ventricular expression of RGK mRNA in IRS 2-k.o. mice:** Rad mRNA was significantly upregulated about twofold in ventricles of 16 week old IRS-k.o. mice (A). Gem and Rem 1 mRNA expression was not significantly changed compared to wt (B,C) (N = 5-6 animals per group; * = $p < 0.05$ vs. age-matched wt in REST-2009© analysis).

At both ages investigated the ventricular expression of $Ca_v1.2$ mRNA was similar in IRS 2-k.o. and wt mice (figure 3.35).

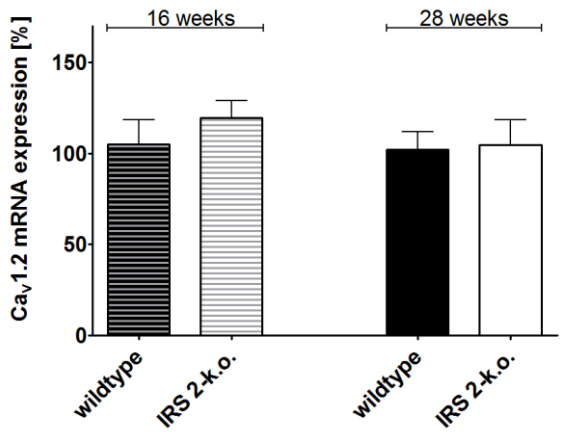

Figure 3.35 **Ventricular expression of $Ca_v1.2$ mRNA in IRS 2-k.o. mice:** $Ca_v1.2$ mRNA expression in IRS 2-k.o. mice and wt was comparable (N = 5-6 animals per group).

Furthermore, no significant changes in Ca_vß-subunits expression could be detected (figure 3.36).

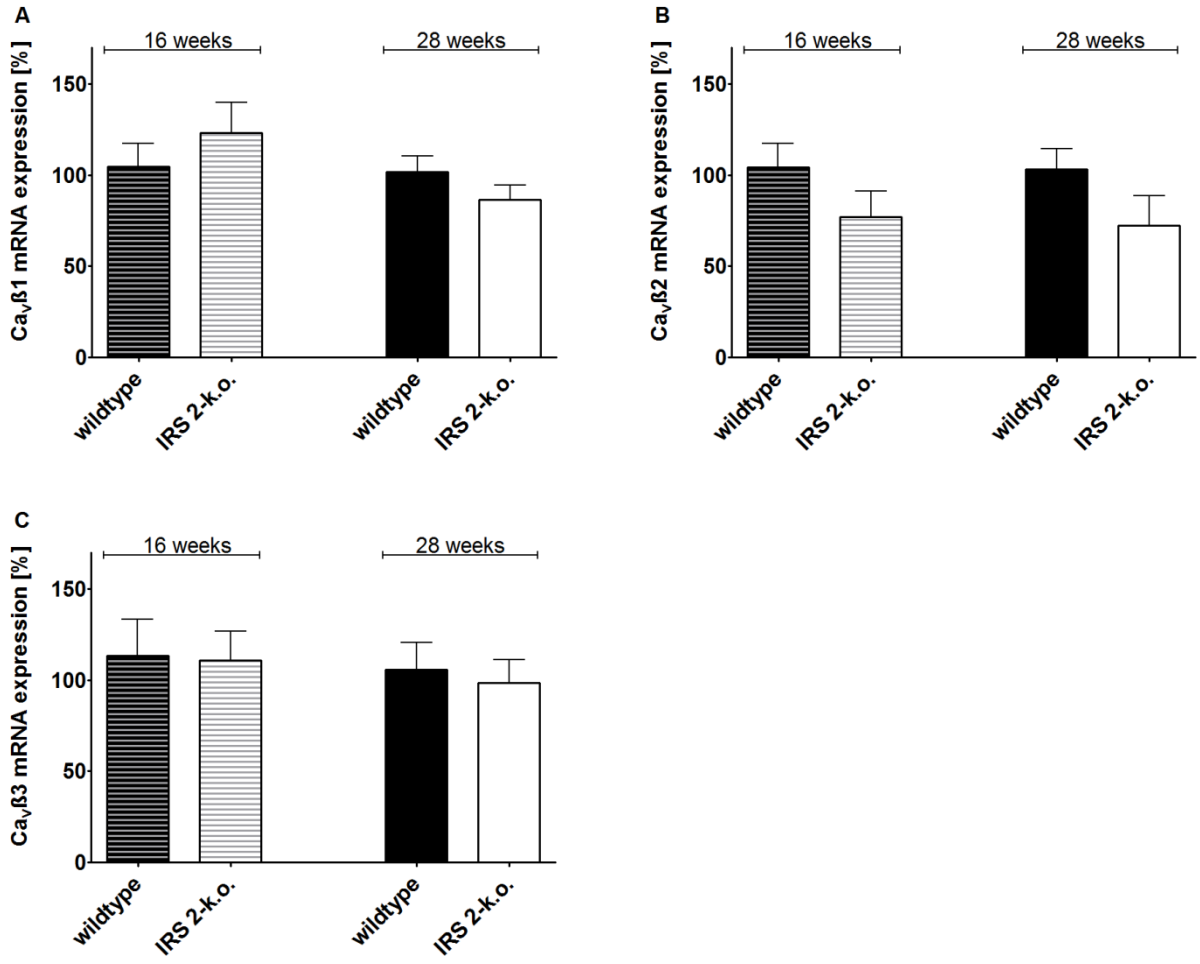

Figure 3.36 **Ventricular expression of the Ca_vß-subunits mRNA in IRS 2-k.o. mice:** mRNA expression of LTCC ß-subunits in IRS 2-k.o. mice and wt was comparable at both ages (N = 5-6 animals per group).

3.6.4 Cardiac protein expression levels

Of note, Western Blot analysis was performed without detection of a housekeeping protein due to technical reasons. As a kind of normalization thus, the ratio of intensities of $Ca_v1.2$ and Rad bands detected in one and the same lane was calculated. Note that levels of relative expression in ventricles of IRS 2-k.o. mice always refer to wt probes used in the same blot.

In ventricles of 16 week old IRS 2-k.o. mice the $Ca_v1.2$/Rad protein ratio was similar to age-matched wt animals (IRS 2-k.o.: 2.54 ± 0.43 vs. wt: 2.40 ± 0.48; N = 4 ventricles per genotype; n = 4-7 blots per ventricle). Of note, at 28 weeks of age the $Ca_v1.2$/Rad ratio was significantly decreased in wt mice compared to younger mice of the same genotype (wt: 0.96 ± 0.11 at 28 weeks vs. 2.40 ± 0.48 at 16 weeks; N = 4-5; n = 4-7). This putative age-related decrease of the $Ca_v1.2$/Rad ratio was not seen in 28 week old IRS 2-k.o. mice (IRS 2-k.o.: 2.61 ± 0.41 at 28 weeks vs. 2.54 ± 0.43 at 16 weeks; N = 4-5; n = 4-7; figure 3.37, (C)). While $Ca_v1.2$ protein expression was unaltered compared to age-matched wt mice (figure 3.37 (B)), Rad protein expression was significantly reduced in ventricles of 28 week old IRS 2-k.o. mice compared to age-matched wt (IRS 2-k.o.: 59.62 ± 3.17 vs. wt: 100.00 ± 5.49; N = 5; n = 4-5; figure 3.37 (A)), thus putatively masking the age-dependent effect on the $Ca_v1.2$/Rad ratio seen in wt mice.

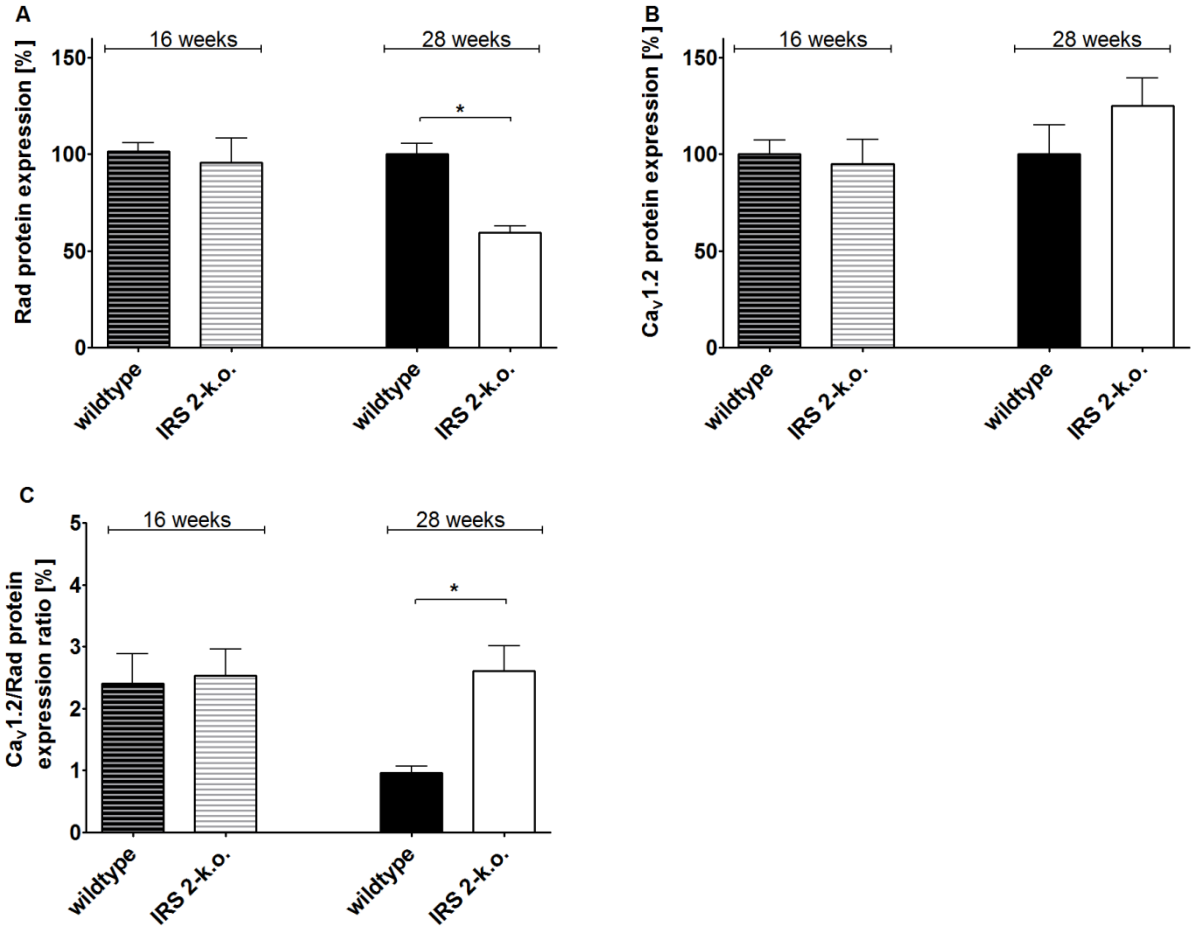

Figure 3.37 **Ventricular expression of Rad and $Ca_v1.2$ protein in IRS 2-k.o. mice:** Rad protein expression was reduced in ventricles of 28 week old IRS 2-k.o. mice (A), while $Ca_v1.2$ protein expression was unaltered (B). An age-related decrease of the $Ca_v1.2$/Rad ratio, as it was observed in wt mice, was absent in 28 week old IRS 2-k.o. mice (C). (N = 4-5 ventricles per genotype; n = 4-7 blots per ventricle).

4 Discussion

4.1 LTCC regulation by RGK proteins in the context of T2DM and/or DCM

Cardiovascular disease (CVD) is a leading cause of death for diabetic patients (Authors/Task Force et al., 2013, Paneni, 2014, Park and Peters, 2014). Since cardiac L-Type Ca^{2+} channels (LTCCs) are known to be involved in proper excitation-contraction coupling they are of high interest in the research of CVD. RGK proteins are known to regulate LTCCs (Buraei et al., 2015), but so far a diabetic context was neglected. This study was designed to shed some light on a putative association of an in vivo regulation of RGK protein expression (in particular of Rad) on ventricular LTCC expression and function in the context of type 2 diabetes mellitus (T2DM) and/or diabetic cardiomyopathy (DCM) in mice. A former study of our group revealed a consistent positive correlation between ventricular Rad and $Ca_v1.2$ protein expression in several mouse models associated with diabetes. E.g. in db/db mice a downregulation of both, Rad and $Ca_v1.2$ protein was found (Fabisch, 2010). An earlier study in db/db mice detected a reduced ventricular whole-cell Ca^{2+} current density with unchanged single-channel activity (Pereira, 2006). Since reduction of whole-cell currents was obviously due to a significantly decrease of $Ca_v1.2$ protein expression, it is tempting to speculate that the Rad protein downregulation was an attempt to compensate for the decreased current density.

In human failing hearts a reduced expression of Rad protein was detected, too (Chang et al., 2007). In contrast to data from diabetic db/db mice whole-cell Ca^{2+} current density in human heart failure (HF) was only slightly if at all decreased (Mukherjee and Spinale, 1998). Both, a decrease of plasmalemmal expression of $Ca_v1.2$ as well as an increased activity of single LTCCs was described ex vivo (Schroeder et al., 1998, Hong et al., 2012, Takahashi et al., 1992, Gruver et al., 1994) Of note, in both cases a reduced Rad expression would be in line with a counterregulation avoiding a reduced Ca^{2+} influx into cardiomyocytes.

In his thesis work C. Fabisch furthermore described an unchanged Rad and $Ca_v1.2$ protein expression in ventricles of 16 week old ob/ob mice (Fabisch, 2010), which fits the corresponding mRNA data determined in the current study. Given the above mentioned in vitro data, an unaltered expression should be suggestive of a “normal” LTCC function and expression. In fact, we found an unaltered maximum whole-cell current density and preliminary single-channel recordings at +10 mV (not shown; data

obtained by Jan Matthes, Center of Pharmacology, University Hospital of Cologne) suggested unchanged activity, too. However, the leftward-shift of the potential of half-maximum activation ($V_{0.5act}$) indicated functional alterations that could not be explained further. In older ob/ob mice both, Rad and $Ca_v1.2$ expression was significantly increased at the protein level (Fabisch, 2010). Assuming the "$Ca_v1.2$-antagonistic" function of Rad, L-type Ca^{2+} currents would thus be expected to be not or only slightly affected. Indeed, whole-cell recordings revealed an unchanged maximum Ca^{2+} current density compared to age-matched wt myocytes. However, we cannot say whether Rad upregulation induced the increase of $Ca_v1.2$ or vice versa. The fact that in cells from older ob/ob mice whole-cell LTCCs opened at more positive potentials and time- or rather calcium-dependent channel inactivation (CDI) was faster in the range of 10 mV to 40 mV might be explained by the observed increase in Rad protein since similar functional changes were described for rat cardiomyocytes overexpressing the human Rad protein after adenoviral infection (Wang et al., 2010). The slowed inactivation at -10 mV might be explained by an interaction with Ca^{2+}/calmodulin (CaM). Pang and colleagues suggested RGK proteins to compete with CaM, thus causing a slowed CDI (Pang et al., 2010). Since preliminary single-channel data indicated an unchanged LTCC activity (not shown; data obtained by Jan Matthes, Center of Pharmacology, University Hospital of Cologne), it is suggested that either Rad inhibited $Ca_v1.2$ channel trafficking to the surface membrane or completely "silenced" a certain fraction of already inserted $Ca_v1.2$ pores. Of note, whole-cell recordings detect the sum of currents carried by virtually all channels expressed in the plasmalemma. In mammalian cardiomyocytes the whole-cell LTCC Ca^{2+} current density is carried by channels located on the surface and in the depth of the T-tubuli, with the latter predominating under normal conditions (Horiuchi-Hirose et al., 2011). Single-channel recordings obtained in the conventional cell-attached configuration do only detect channels expressed in the surface membrane, i.e. channels expressed in the depth of the T-tubuli are neglected. Thus we cannot exclude that the activity of T-tubular but not surface channels was actually decreased. In fact, very recent data showed a differential regulation of surface and T-tubular single LTCCs in ventricular myocytes from human and rat (non-diabetic) hearts (Sanchez-Alonso et al., 2016). In the current study we find that in ventricles of 28 week old ob/ob mice Rad mRNA expression was unchanged and $Ca_v1.2$ mRNA was significantly decreased, while both appeared to be increased at the protein level (Fabisch, 2010). Many studies showed an apparently poor correlation between mRNA and protein expression levels (Koussounadis et al., 2015, Su et al., 2015). Discrepancies were

attributed to post-transcriptional modifications of mRNA, different half-lives of proteins as the result of varied protein synthesis and degradation and inaccuracies in experiments (Greenbaum et al., 2003). The present study also revealed that the mRNA amount of the accessory LTCC subunits Ca_vß1 and Ca_vß2 was nearly halved in ventricles of ob/ob mice at both ages investigated. If mRNA and protein expression data would correlate in this case, these findings would suggest a reduced surface expression of LTCCs and/or a decreased stimulation, i.e. a reduced channel open probability, a rightward shift of $V_{0.5act}$ or altered channel gating kinetics (Buraei and Yang, 2013). It might also be speculated that the Ca_vß-subunit regulated the Rad inhibitory effect since Ca_vß is required for an inhibition (Buraei and Yang, 2015). Since Rad and Ca_v1.2 expression changed with age (and/or duration of diabetes) in ob/ob mice while Ca_vß (mRNA) expression remained unaltered a relationship between these findings seems to be rather unlikely.

Whole-cell recordings of Rad-k.o. myocytes indicate the extent of an inhibitory effect of Rad on LTCCs. Manning et al. showed a significantly increased current density and a shift of steady-state activation to more negative potentials (Manning et al., 2013). Data obtained in the current study confirm these earlier findings. Compared to age-matched wt mice the mean peak current density of 16 week old mice was increased by about 84%. The mean peak current density of older mice was even augmented by 142% compared to age-matched wt. The leftward shift of $V_{0.5act}$ observed by Manning et al. and us strengthens our hypothesis of a connection between the rightward shift of $V_{0.5act}$ and (relative) Rad overexpression observed in 28 week old ob/ob mice. This is supported by findings of Wang et al. who showed that adenoviral induction of Rad (over-) expression caused a rightward shift of steady-state activation in cultured rat cardiomyocytes (Wang et al., 2010). While Manning et al. did not state the age of the mice they investigated our data suggest an age-related effect (or “decompensation”) of Rad deficiency in ventricular myocytes. An age-dependent effect is furthermore suggested by the observation that recovery from inactivation was decelerated only in Rad-k.o. mice at an age of 16 weeks. We for the first time analyzed mRNA levels of RGK proteins and LTCC Ca_vß-subunits in Rad-k.o. mice, which could give a hint towards further mechanisms in LTCC regulation and RGK interplay. At 16 weeks of age Gem mRNA was upregulated about twofold and Ca_vß2 mRNA was downregulated. This could be a first response to protect the heart against an increased LTCC function. In older mice Rem 1 mRNA expression was increased, too. In addition to reduced Ca_vß2 mRNA Ca_v1.2 mRNA was downregulated at 28 weeks of age. Of note, Manning et al.

(2015) observed a reduction of $Ca_v1.2$ protein expression. But again Manning et al. did not state the age of the mice they investigated. Taken together, the increased current density rather seems to be due to an increased activity of single LTCCs. Further studies have to test for this hypothesis. At this point it has to be mentioned that the extent of inhibition and the kind of interaction with $Ca_v1.2$ may vary depending on the particular RGK protein. In Rem 1-k.o. mice the increase in current density appeared weaker compared to our study (approx. +20%) and $V_{0.5act}$ was shifted to more positive potentials (Magyar et al., 2012).

In 16 week old ob/ob x Rad-k.o. mice whole-cell patch-clamp data were similar to age-matched Rad-k.o. mice: compared to age-matched wt mice the mean peak current density was increased by about 97%, $V_{0.5act}$ was shifted to more negative potentials and the recovery from inactivation was slowed, too. These findings suggest that the role of Rad (and thus the effects of lacking Rad) is similar on a wildtype and an ob/ob background - at least at an age of 16 weeks. Given the increased Rad (and $Ca_v1.2$) expression in older ob/ob mice it would be of particular interest to test for a putative additive effect of Rad deficiency and $Ca_v1.2$ increase.

In 16 week old IRS 2-k.o. mice whole-cell Ca^{2+} current density was significantly decreased compared to age-matched control, although Rad and $Ca_v1.2$ protein expression appeared to be unchanged. Thus, another mechanism underlying the decreased current density has to be assumed. mRNA analysis of accessory $Ca_vß$-subunits and of the other RGK proteins also did not reveal a hint towards the origin of current density reduction in young IRS 2-k.o. mice. In comparison to young IRS 2-k.o. mice 28 week old mice of the same genotype showed a significantly increased Ca^{2+} current density, that was no longer different compared to age-matched controls. Of interest, the putative age-related decrease of the $Ca_v1.2$/Rad ratio, which was observed in wt mice, was not seen in 28 week old IRS 2-k.o. mice. The finding that at an age of 28 weeks $Ca_v1.2$ protein expression was unaltered compared to age-matched wt mice, while Rad protein expression was significantly reduced indicates an (age-dependent) loss of LTCC inhibition by Rad in IRS 2-k.o. mice. This interpretation is supported by our finding that $V_{0.5act}$ was significantly shifted to more negative potentials similar to data obtained from Rad-k.o. mice. The increase in whole-cell Ca^{2+} current density compared to younger mice thus indicates a compensatory mechanism based upon regulation of Rad expression. Note, that in human heart failure unchanged current density and decreased expression of Rad suggest a similar mechanism (Chang et al., 2007, Mukherjee and Spinale, 1998). Further studies should investigate putative changes of

single ventricular LTCC activity in IRS 2-k.o. and/or Rad-k.o. mice. Again it is important to consider that Western Blot data represent the expression of the total cardiac membrane protein fraction, including T-tubular and sarcolemmal membrane proteins. We were not able to discriminate whether the decrease in Rad protein affected single-channel activity or $Ca_v1.2$ channel trafficking to the surface membrane or both, respectively. Experiments in order to differentially investigate the T-tubular and sarcolemmal expression of LTCCs would thus be helpful as well as single-channel measurements. Besides, Western Blot studies were limited because Coomassie staining of the already blotted SDS gels sometimes revealed an incomplete transfer of protein to the blotting membrane. But given that PVDF membrane protein binding capacity was not exhausted and that measurements were performed within the linearity of the detection system (figure 8.16, appendix), it is assumed that proteins were transferred equally within one blot. In contrast to our data C. Fabisch observed an unchanged protein expression ratio in ventricles of 28 week old IRS 2-k.o. mice (C. Fabisch; unpublished data). However, it should be noted that in the current study the $Ca_v1.2$-to-Rad ratio was calculated by detecting the intensities of $Ca_v1.2$ and Rad bands in one and the same lane, while C. Fabisch detected the proteins separately. The protein levels we obtained correlate poorly with the respective mRNA levels. While in young IRS 2-k.o. mice Rad mRNA was upregulated about twofold, Rad protein remained unchanged. In older mice Rad mRNA expression was no longer altered compared to age-matched wt, but Rad protein was decreased. It might be speculated that Rad mRNA was subject to post-transcriptional modifications or that protein degradation was enhanced. Of note, the current study was limited because of the use of whole-ventricle homogenates for expression analyses via qRT-PCR. Purification experiments in order to separate cardiomyocytes from other cell types failed. Thus we cannot exclude that the change in Rad mRNA expression was (partly) attributed to “non-cardiomyocytes”.

Taking together, the increase of both, Rad and $Ca_v1.2$ protein in old ob/ob mice while unchanged maximum Ca^{2+} current density suggests a functional role of Rad in LTCC regulation. However, we cannot say whether Rad upregulation induced the increase of $Ca_v1.2$ or vice versa. Our data obtained from Rad-k.o. mice confirm the inhibitory function of Rad and furthermore indicate an age-related effect. Whole-cell recordings of ob/ob x Rad-k.o. myocytes further suggest that the role of Rad or rather the effect of a Rad deficiency is similar on a wildtype and an ob/ob background. Our data received from 28 week old IRS 2-k.o. mice are suggestive of a compensatory effect of Rad

protein on LTCC function, i.e. an attempt to compensate for a reduced calcium current density independent of the $Ca_v1.2$ expression. The reduced Rad protein expression appeared to provoke effects similar to that observed in the total Rad deficiency in Rad-k.o. mice. Although the current study suggests LTCC regulation by Rad in two different diabetic mouse models, not all results could be explained only by assuming the "$Ca_v1.2$-antagonistic" or compensatory function of Rad. Our data suggest that there is no uniform, diabetes-associated mechanism of Rad-$Ca_v1.2$ interaction. Putative influencing factors that might also be involved in LTCC regulation are discussed in the following section.

4.2 Further molecular mechanisms that might be involved in LTCC regulation

Cardiac electrophysiological properties are amongst others regulated by the sympathetic nervous system (Yu et al., 2011). As a compensatory reaction to the reduced cardiac output in heart failure (HF) the renin-angiotensin-aldosterone system (RAAS) and the sympathetic nervous system are activated (King et al., 2012). An activation of the sympathetic nervous system increases the levels of catecholamines, endogenous agonists of adrenoceptors (α1, α2, ß1, ß2 and ß3). The β1-adrenergic receptor is predominantly expressed in the heart (Madamanchi, 2007). In general, stimulation of ß-adrenergic receptors leads to an activation of protein kinase A (PKA). PKA then phosphorylates several targets like troponin I, LTCCs or PLN, resulting in enhanced cardiac contractility (Madamanchi, 2007). Phosphorylation of LTCCs by PKA has been subject to various studies, indicating that either the Ca_vα1-subunit or the Ca_vß-subunits can mediate the ß-adrenergic stimulation (Hofmann et al., 2014). In HF the heart appears to be protected against chronic adrenergic (over-) stimulation via an impaired ß-adrenergic signaling and decreased PKA activity (Najafi et al., 2016). Rad-k.o. mice display a rather improved cardiac function. Nevertheless ß-adrenergic response is impaired (Manning et al., 2013), similar to findings from human HF (Schroeder et al., 1998, Chen et al., 2002). Since Rad is phosphorylated by Ca^{2+}/CaM-dependent protein kinase II, PKA and protein kinase C (Moyers et al., 1998), this RGK protein might be also involved in the adrenergic regulation of cardiac LTCCs. PKD1, a protein kinase downstream of α(1)-adrenergic signaling, was shown to phosphorylate Rem 1 upon α(1)-adrenergic stimulation with the release of the inhibitory effect of Rem 1 as a consequence (Jhun et al., 2012). Of note, Withers et al. showed that

α-adrenergic activation stimulated phosphorylation of Rem 1 but not of Rad. However, Rad was phosphorylated upon β-adrenergic receptor stimulation, a process that could be blocked by PKA inhibition. Indeed, CoIPs indicated that Rad phosphorylation weakened LTCC association (Withers et al., 2015). In 10 week old ob/ob mice ß-adrenergic responsiveness was impaired and PKA activity was significantly depressed (Minhas et al., 2005). Thus, Rad protein might have been less phosphorylated and LTCC inhibition weakened. Of note, our preliminary single-channel data from ob/ob mice do not hint at an altered adrenergic LTCC regulation. Garcia-Barrado and colleagues investigated ß-cell function and lipolysis in IRS 2-k.o. mice and demonstrated an impaired adrenergic signaling in combination with altered adrenoceptor expression levels (Garcia-Barrado et al., 2011). Such experiments with ventricular tissue of IRS 2-k.o. mice have not been performed so far. However, insulin-induced phosphorylation of ß-adrenergic receptors was shown to be dependent on IRS 2 with lack of IRS 2 leading to an attenuated cAMP/PKA activity in cardiomyocytes (Fu et al., 2014). To sum it up, altered adrenergic signaling can affect cardiac LTCC expression and function. RGK proteins might be involved since they are a well-known targets of PKA. However, so far our data do not indicate altered adrenergic regulation of LTCCs in the investigated mouse models.

In several studies it was suggested that PI3K/Akt signaling positively regulates LTCCs in ventricular myocytes (Ballou et al., 2015). In this context Viard et al. showed that an increase of PIK3 and Akt/PKB triggered $Ca_v1.2$ channel trafficking to the plasma membrane and that the Ca_vß2-subunit was required to support this regulation by PI3K in particular (Viard et al., 2004). Catalucci et al. suggested that an Akt-dependent phosphorylation of the Ca_vß2-subunit protects $Ca_v1.2$ from degradation and thus increases whole-cell current density (Catalucci et al., 2009). Recently Rusconi et al. published that the $Ca_v1.2$ amount and the Akt-dependent phosphorylation status of $Ca_vβ2$ were correlated and that Ca_vß2 underwent conformational changes upon phosphorylation which induced an increased current density (Rusconi et al., 2016). Two diabetic mouse models exhibited alterations in LTCC current density probably caused by a decrease in insulin/PI3K/Akt signaling: in type 1 diabetic $Ins2^{Akita}$ mice LTCC current density was reduced, including shifts in the voltage dependence of (in)activation to more positive potentials. Intracellular delivery of PI(3,4,5)P3 normalized these parameters to control levels and further experiments led to the hypothesis that $Ca_v1.2$ surface expression was reduced, whereas the total amount of protein was unaltered (Lu

et al., 2007). In db/db mice a defect in insulin signaling was suggested to be partly responsible for a depressed current density because infusion with $PI(3,4,5)P_3$, Akt1 or Akt2 increased the current density (Lu et al., 2011). Similar to human T2DM patients an excessive myocardial insulin signaling activity (IRS1-PI3K-activity) was shown in ob/ob mice. This went in parallel with an activation of the insulin receptor. Total Akt levels were unchanged, but basal Akt phosphorylation was increased and insulin-stimulated Akt phoshorylation was blunted (Cook et al., 2010). Given this interplay between insulin-signaling, Akt and Ca_vß2-subunits it would be desirable to check for the downregulation of Ca_vß2-subunits we observed at the mRNA level at the protein level or even to look at the phosphorylation of auxiliary LTCC subunits. Studies performed with IRS 2-k.o. mice demonstrated an insulin-dependent decrease in PI3K activity in liver and skeletal muscle (Withers et al., 1998). Cardiac PI3K activity has not been evaluated in IRS 2-k.o. mice yet. But a cardiac-specific k.o. of IRS 2 (CIRS 2 mice) revealed a lower cardiac PI3K activation (Riehle et al., 2014). In IRS 2-k.o. mice compensation for insulin resistance appeared to be impaired because hyperinsulinemia was accompanied by a ß-cell decrease of 42% compared to wt (Kubota et al., 2000, Withers et al., 1998). The decrease of cardiac whole-cell current density we observed in young IRS 2-k.o. mice might thus be attributed to an altered insulin signaling. Of note, a transgenic mouse overexpressing Rad in skeletal muscle and maintained on a high-fat diet developed more severe glucose intolerance and insulin resistance than control mice (Ilany et al., 2006). It is thus tempting to speculate that the reduced Rad expression observed in hearts of older IRS 2-k.o. mice was to reverse the decrease of ventricular Ca^{2+} currents by re-establishing insulin signaling. Taken together, several studies indicated an influence of PI3K/Akt signaling on LTCC regulation in ventricular myocytes. It was shown that an Akt-dependent phosphorylation of the Ca_vß2-subunit protects Ca_v1.2 from degradation. Since our whole-cell patch-clamp data obtained from young IRS 2-k.o. mice could not be explained only by assuming the "Ca_v1.2-antagonistic" function of Rad, here insulin signaling might be relevant for LTCC regulation, too. Of interest, in IRS 2-k.o. mice compensation for insulin resistance appeared to be impaired.

In ob/ob hearts strong evidence for oxidative stress was detected which worsened cardiac efficiency (Boudina et al., 2005, Li et al., 2006, Gharib et al., 2016). Increased mitochondrial oxidative stress was also observed in atrial tissue of T2DM patients (Anderson et al., 2009, Anderson et al., 2011). Moreover, in human muscle biopsies of patients with sporadic amyotrophic lateral sclerosis oxidative stress triggered Rad

upregulation (Halter et al., 2010). Thus, oxidative stress might be a contributing factor to the upregulation of Rad protein observed in ventricles of 28 week old ob/ob mice.

4.3 Reliability of investigated mouse models – relevance and metabolic determinants for human T2DM & DCM

In T2DM patients hyperglycemia develops slowly and worsens over time as a response to insulin resistance and compensatory hyperinsulinemia (Wang et al., 2014). Insulin resistance is associated with metabolic, structural and functional changes in the heart that may lead to DCM and HF (Abel et al., 2012). In humans, overweight/obesity is known to be a main risk factor for developing T2DM (Chatzigeorgiou et al., 2009, Wang et al., 2014). But it is disputable to what extent leptin and its signaling pathways contribute to the development of the disease. To date, eleven pathogenic mutations have been reported in the human leptin gene (Wasim et al., 2016). Interestingly, obese T2DM patients often reveal elevated leptin levels compared to non-diabetic obese humans (Wang et al., 2014). Amongst other reasons hyperleptinemia may be evoked by insulin resistance and may lead to leptin resistance (Ren, 2004). The specific cardiac effects of leptin are not fully elucidated and many studies reveal controversial results. But it is sure that leptin can have beneficial as well as detrimental effects on cardiac function (Feijoo-Bandin et al., 2015, Hall et al., 2015, Martinez-Martinez et al., 2014, Martin et al., 2008). In the ob/ob mouse model leptin deficiency appears to be a relevant factor for T2DM and DCM since replacement of leptin corrects many diabetic manifestations and improves left ventricle remodeling (Lindstrom, 2007, Barouch et al., 2003). Ob/ob mice develop obesity which then appears to predispose them to the development of diabetes-associated disturbances. These animals already exhibit mild hyperglycemia by four weeks of age and become severe hyperglycemic not later than at 15 weeks of age (Buchanan et al., 2005). Of note, in the current study the elevation of blood glucose of 28 week old ob/ob mice was less pronounced compared to younger ob/ob animals. According to The Jackson Laboratory hyperglycemia may be transient in ob/ob mice, but individual variability exists (Leiter, 1992). On the other hand, another study did not find an attenuation of hyperglycemia with progressing age (Van den Bergh et al., 2008). In addition, it has to be taken into account that, similar to human T2DM patients, the phenotype of a mouse model may vary due to differences in the genetic background, gender and age (Cefalu, 2006). For example, the severity of diabetes in ob/ob mice obviously varies depending on the genetic background (Coleman, 1978,

Haluzik et al., 2004). Although ob/ob mice develop T2DM associated changes earlier in life compared to humans they are accepted as an appropriate model for studying T2DM as well as DCM since as human patients ob/ob mice are hyperinsulinemic and develop severe insulin resistance (Lindstrom, 2007, Buchanan et al., 2005). In contrast to humans the pancreatic ß-cell morphology and amount differ. The insulin release capacity remains high throughout life (Bock et al., 2003, Kim et al., 2009, Lindstrom, 2007, Del Guerra et al., 2005). Interestingly, long-term microvascular complications observed in diabetic humans such as nephropathy, neuropathy and retinopathy and/or macrovascular complications due to atherosclerosis are absent in ob/ob mice (Wang et al., 2014). Therefore ob/ob mice might rather reflect the “prediabetic” phenotype, e.g. as common for the metabolic syndrome. However, similar to human diabetic patients hearts of ob/ob mice exhibit metabolic, structural and functional changes (Gharib et al., 2016, Sloan et al., 2011, Fukui et al., 2013, Buchanan et al., 2005, Christoffersen et al., 2003, Mazumder et al., 2004, Boudina et al., 2005, Li et al., 2006, Fauconnier et al., 2005, Minhas et al., 2005, Ren et al., 2010, Barouch et al., 2006). Both T2DM patients and ob/ob mice exhibit an excessive myocardial insulin signaling activity (Cook et al., 2010). Studies in mice and humans reveal an important role of myocardial insulin signaling in the context of cardiac hypertrophy and heart failure (Riehle and Abel, 2016). Based on our current findings though we cannot exclude that the increase of heart weight observed in older ob/ob mice is physiologic due to the vast increase of body weight. Other studies revealed a hypertrophy in this mouse model (Ren et al., 2010, Barouch et al., 2003). Since furthermore a major definition criteria, the absence of hypertension, is fulfilled ob/ob mice, this mouse model can be taken as a model of DCM (Mark et al., 1999, Fukui et al., 2013, Barouch et al., 2003).

Concerning the IRS 2 gene data in literature are inconsistent and rare in identifying human polymorphisms that might be associated with T2DM (Jiang et al., 2015). But it is known that the protein expression may be altered in diabetic humans (Hirashima et al., 2003). According to diabetic patients IRS 2-k.o. mice are hyperglycemic, hyperinsulinemic, insulin resistant as well as hyperleptinemic (Sesti et al., 2001, Burks et al., 2000, Withers et al., 1998, Kubota et al., 2000). Most likely depending on the genetic background several studies showed conflicting findings regarding body weight of IRS 2-k.o. mice (Garcia-Barrado et al., 2011, Masaki et al., 2004, Burks et al., 2000, Kubota et al., 2000, Withers et al., 1998). In the current study body weight of IRS 2-k.o. mice was similar to wt. There was no evidence for cardiac hypertrophy since ventricle weights as well as ventricle-to-body weight ratios were similar to wt, too. To our

knowledge no further data on cardiac morphology or function on the background of a global IRS 2-k.o. has been published, but premature death was observed (Withers et al., 1998). Of note, mice with a cardiac-specific k.o. of IRS 2 exhibit cardiac hypertrophy (Riehle et al., 2014). Several mouse models associated with disturbances of the IRS signaling have pathophysiological disturbances within the heart: for the cardiac-specific IRS 2-k.o. mouse model a reduced cardiac efficiency was shown (Riehle et al., 2014). Mice with a cardiac-specific k.o. of both, IRS 1 and IRS 2 die within 11 weeks. These mice have an impaired mitochondrial function, increased autophagy and apoptosis, myocyte loss and heart failure (Riehle et al., 2013, Qi et al., 2013). Mice with a global k.o. of both proteins appear to be not viable since no born animals rendered this genotype (Withers et al., 1999). The current study observed a significantly reduced whole-cell Ca^{2+} current density in young IRS 2-k.o. mice. This may suggest a disturbance in the contractile machinery, too. Indeed, genetically engineered mice expressing a lower level of cardiac L-type calcium channels develop hypertrophy and heart failure (Goonasekera et al., 2012). The observed normalization of calcium current density to wt levels in IRS 2-k.o. at 28 weeks of age might then be interpreted as anti-hypertrophic. However, in mice where cardiac calcium current density is reduced due to the knockout of an auxiliary beta-subunit the expression of the $Ca_v1.2$ channel pore was unchanged and these animals did not develop ventricular hypertrophy (Meissner et al., 2011).

To sum it up, ob/ob as well as IRS 2-k.o. mice are valuable mouse models in studying T2DM (King, 2012, Chatzigeorgiou et al., 2009, Lee and Cox, 2011). Both mouse models provide useful knowledge about different phenotypes and the underlying pathomechanisms that are prevalent in humans. Ob/ob mice also share many traits with the hearts of humans with DCM. So far it has not been evaluated whether the IRS 2-k.o. mouse model also represents a suitable model for DCM. One has to keep in mind that the transfer of murine data to humans should be done very carefully, though mouse models are helpful to understand the role of insulin signaling and other pathways/molecules in the regulation of cardiac function.

4.4 Limitations of the study

In the current study we wanted to consider the putative influence of a time-dependent onset of T2DM disease progression and following complications by using two different age groups. However, the ages 16 and 28 weeks were chosen arbitrarily. In the development of human DCM not only age but also gender appears to be an influencing factor. Of note, female T2DM patients seem to be more affected (Jia et al., 2016). But so far there is no evidence that sex difference is relevant for DCM in mice. E.g. in db/db mice no hints were found (Pereira, 2006). The present study was not designed to take a closer, separate look on gender and thus did not have the respective statistical power. However, in IRS 2-k.o. mice there is a gender difference regarding blood glucose (Withers et al., 1998). Given the discussed putative cardiac effects of insulin a gender-specific analysis should be considered. It should also be noted that the comparability of protein expression data obtained in the current study and in C. Fabisch's thesis work is limited due to differences in the used protocols (Fabisch, 2010). Furthermore, in the current project the completion of protein and mRNA data was not possible due to time constraints (protein data for Rad-k.o mice; mRNA and protein data for ob/ob x Rad-k.o. mice).

5 Conclusion & outlook

The current study indicates an interaction between Rad and LTCCs in two different diabetic mouse models. The obtained findings mostly correspond with a "$Ca_v1.2$-antagonistic" or compensatory function of Rad on LTCC expression and/or function. However, in young IRS 2-k.o. mice another mechanism underlying the decreased current density has to be assumed. Thus, our data suggest that there is no uniform, diabetes-associated mechanism of Rad-$Ca_v1.2$ interaction. Differences between the investigated mouse models might be attributed to differences in the underlying pathomechanisms. Further work is required for clarification e.g. of the pathophysiological importance of the disrupted insulin and leptin signaling pathways. Changes at the level of receptors or ligands might be compensated by the other signaling pathway while impairment downstream at the level of IRS 2 might severely affect insulin signaling here. It would be important to determine different phosphorylation states of the receptors and downstream signaling molecules such as IRS, Akt, PI3K or STAT in the heart, in particular for IRS 2-k.o. mice. It is probably more an interplay of parameters and not a single parameter that is crucial for LTCC regulation in DCM. Besides, the effect of an altered Rad protein expression on LTCC (expression and/or) function has not been conclusively clarified in the current study yet - further studies should investigate putative changes of single ventricular LTCC activities in cardiomyocytes of ob/ob and IRS 2-k.o. mice. It would also be reasonable to investigate other rodent mouse models associated with T2DM. Taken together, further research is necessary to evaluate the role of a Rad-$Ca_v1.2$ interaction in a diabetic context. Anyway, RGK proteins, e.g. Rad, might be promising targets to develop therapeutic strategies for the treatment of cardiac diseases.

6 Summary

Cardiovascular disease (CVD) is a leading cause of death for diabetic patients. Diabetic cardiomyopathy (DCM) is characterized by an abnormality of myocardial diastolic or systolic function in diabetic subjects without the major heart failure risk factors hypertension and/or (overt) coronary artery disease. The pathophysiology of DCM remains largely unclear and needs to be further elucidated in order to develop targeted therapeutic strategies. Since cardiac L-Type calcium channels (LTCCs) are known to be involved in proper excitation-contraction coupling, they are of high interest in the research of CVD, such as DCM and resulting heart failure (HF).

In human (non-diabetic) HF whole-cell Ca^{2+} current density of ventricular LTCCs was unchanged. Both, a decrease of plasmalemmal expression of $Ca_v1.2$ as well as an increased activity of single LTCCs was described ex vivo. These findings suggest changes in both expression and function of LTCCs. In contrast, in a mouse model associated with DCM (the so-called db/db mice with leptin receptor deficiency) whole-cell Ca^{2+} current density was reduced, while single-channel activity was unchanged. It has been shown that RGK proteins, like the diabetes-associated Rad, might be involved in LTCC regulation, both regarding its function and expression. Rad expression is reduced in human HF and whole-cell calcium current densities are increased in cardiomyocytes of Rad-k.o. mice. Though previous data suggest that the ventricular expression levels of Rad and $Ca_v1.2$ proteins are positively correlated in several mouse models with diabetes-associated metabolic disturbances, the effect of Rad on cardiac LTCCs in a diabetic context remains unclear.

To address Rad-LTCC interaction in a diabetic context two of the previously screened mouse models were investigated in the present study: leptin-deficient obese ob/ob mice and mice lacking IRS 2, respectively. Though experiments with Rad-k.o. and Rem 1-k.o. mice suggest an impressive inhibitory effect of RGK proteins on native cardiac LTCCs, it remains unclear whether differential expression of RGK proteins might be compensatory, causative or both regarding LTCC regulation. Thus, the present study aims at the role of in vivo regulation of Rad expression on ventricular LTCC expression and function. For this, ventricular L-type calcium current densities were obtained by patch-clamp recordings and compared to those of wildtype littermates in the context of ventricular expression levels of Rad and $Ca_v1.2$ mRNA and protein. In order to further evaluate the role of Rad in ob/ob mice, we generated and analyzed ob/ob mice lacking Rad. In summary, it should be elucidated whether there is a unifying effect of Rad on

LTCCs in diabetic hearts that might suggest a mechanism underlying diabetic cardiomyopathy.

Mice of different ages (16 and 28 weeks) were chosen for experiments to take time-dependent onset of obesity and disease progression of T2DM into account. Since the expression of the other RGK proteins and LTCC ß-subunits (Ca_vß1- Ca_vß3) might have contributed to an altered LTCC regulation, their expression levels were checked as well. In old ob/ob mice both, Rad and $Ca_v1.2$ expression was significantly upregulated at the protein level, while whole-cell Ca^{2+} current density was unaltered compared to age-matched control. Since preliminary single-channel data indicated an unchanged LTCC activity, it is suggested that either Rad inhibited $Ca_v1.2$ channel trafficking to the surface membrane or completely "silenced" a certain fraction of already inserted $Ca_v1.2$ pores. However, we cannot say whether Rad upregulation induced the increase of $Ca_v1.2$ or vice versa. Our data obtained from Rad-k.o. mice confirm the inhibitory function of Rad protein on LTCCs and furthermore indicate an age-dependent effect. Whole-cell recordings of ob/ob x Rad-k.o. myocytes further suggest that the role of Rad is similar on a wildtype and an ob/ob background.

In young IRS 2-k.o. mice whole-cell Ca^{2+} current density was significantly decreased compared to age-matched control. Since Rad and $Ca_v1.2$ protein expression appeared to be unchanged another mechanism underlying the decreased current density has to be assumed, e.g. altered insulin signaling. In comparison to young IRS 2-k.o. mice older mice of the same genotype showed a significantly increased Ca^{2+} current density, that was no longer different compared to age-matched control. Of interest, the putative age-related decrease of the $Ca_v1.2$/Rad ratio, which was observed in wt mice, was not seen in 28 week old IRS 2-k.o. mice. The finding that at an age of 28 weeks $Ca_v1.2$ protein expression was unaltered compared to age-matched wt mice, while Rad protein expression was significantly reduced indicates an (age-dependent) loss of LTCC inhibition by Rad in IRS 2-k.o. mice. It is tempting to speculate that this is an attempt to compensate for a reduced calcium current density independent of the $Ca_v1.2$ expression. Of note, in human heart failure unchanged current density and decreased expression of Rad suggest a similar mechanism.

To sum it up, the current study indicates interaction between Rad and LTCCs in two different diabetic mouse models. The obtained findings mostly correspond with a "$Ca_v1.2$-antagonistic" or compensatory function of Rad on LTCC expression and/or function, but our data suggest that there is no uniform, diabetes-associated mechanism of Rad-$Ca_v1.2$ interaction. Differences between the investigated mouse models might

be attributed to differences in the underlying pathomechanisms. Further work is required for clarification e.g. of the pathophysiological importance of the disrupted insulin and leptin signaling pathways. Changes at the level of receptors or ligands might be compensated by the other signaling pathway while impairment downstream at the level of IRS 2 might severely affect insulin signaling here. It is probably more an interplay of parameters and not a single parameter that is crucial for LTCC regulation in DCM. Anyway, RGK proteins, e.g. Rad, might be promising targets to develop therapeutic strategies for the treatment of cardiac diseases.

7 References

ABEL, E. D., O'SHEA, K. M. & RAMASAMY, R. 2012. Insulin resistance: metabolic mechanisms and consequences in the heart. *Arterioscler Thromb Vasc Biol,* 32**,** 2068-76.

ALEXANDER, M. C., LOMANTO, M., NASRIN, N. & RAMAIKA, C. 1988. Insulin stimulates glyceraldehyde-3-phosphate dehydrogenase gene expression through cis-acting DNA sequences. *Proc Natl Acad Sci U S A,* 85**,** 5092-6.

ALMAGOR, L., CHOMSKY-HECHT, O., BEN-MOCHA, A., HENDIN-BARAK, D., DASCAL, N. & HIRSCH, J. A. 2012. The role of a voltage-dependent Ca2+ channel intracellular linker: a structure-function analysis. *J Neurosci,* 32**,** 7602-13.

ALTIER, C., DUBEL, S. J., BARRERE, C., JARVIS, S. E., STOTZ, S. C., SPAETGENS, R. L., SCOTT, J. D., CORNET, V., DE WAARD, M., ZAMPONI, G. W., NARGEOT, J. & BOURINET, E. 2002. Trafficking of L-type calcium channels mediated by the postsynaptic scaffolding protein AKAP79. *J Biol Chem,* 277**,** 33598-603.

AMERICAN DIABETES, A. 2015. (2) Classification and diagnosis of diabetes. *Diabetes Care,* 38 Suppl**,** S8-S16.

ANDERSON, E. J., KYPSON, A. P., RODRIGUEZ, E., ANDERSON, C. A., LEHR, E. J. & NEUFER, P. D. 2009. Substrate-specific derangements in mitochondrial metabolism and redox balance in the atrium of the type 2 diabetic human heart. *J Am Coll Cardiol,* 54**,** 1891-8.

ANDERSON, E. J., RODRIGUEZ, E., ANDERSON, C. A., THAYNE, K., CHITWOOD, W. R. & KYPSON, A. P. 2011. Increased propensity for cell death in diabetic human heart is mediated by mitochondrial-dependent pathways. *Am J Physiol Heart Circ Physiol,* 300**,** H118-24.

AROOR, A. R., MANDAVIA, C. H. & SOWERS, J. R. 2012. Insulin resistance and heart failure: molecular mechanisms. *Heart Fail Clin,* 8**,** 609-17.

AUTHORS/TASK FORCE, M., RYDEN, L., GRANT, P. J., ANKER, S. D., BERNE, C., COSENTINO, F., DANCHIN, N., DEATON, C., ESCANED, J., HAMMES, H. P., HUIKURI, H., MARRE, M., MARX, N., MELLBIN, L., OSTERGREN, J., PATRONO, C., SEFEROVIC, P., UVA, M. S., TASKINEN, M. R., TENDERA, M., TUOMILEHTO, J., VALENSI, P., ZAMORANO, J. L., GUIDELINES, E. S. C. C. F. P., ZAMORANO, J. L., ACHENBACH, S., BAUMGARTNER, H., BAX, J. J., BUENO, H., DEAN, V., DEATON, C., EROL, C., FAGARD, R., FERRARI, R., HASDAI, D., HOES, A. W., KIRCHHOF, P., KNUUTI, J., KOLH, P., LANCELLOTTI, P., LINHART, A., NIHOYANNOPOULOS, P., PIEPOLI, M. F., PONIKOWSKI, P., SIRNES, P. A., TAMARGO, J. L., TENDERA, M., TORBICKI, A., WIJNS, W., WINDECKER, S., DOCUMENT, R., DE BACKER, G., SIRNES, P. A., EZQUERRA, E. A., AVOGARO, A., BADIMON, L., BARANOVA, E., BAUMGARTNER, H., BETTERIDGE, J., CERIELLO, A., FAGARD, R., FUNCK-BRENTANO, C., GULBA, D. C., HASDAI, D., HOES, A. W., KJEKSHUS, J. K., KNUUTI, J., KOLH, P., LEV, E., MUELLER, C., NEYSES, L., NILSSON, P. M., PERK, J., PONIKOWSKI, P., REINER, Z., SATTAR, N., SCHACHINGER, V., SCHEEN, A., SCHIRMER, H., STROMBERG, A., SUDZHAEVA, S., TAMARGO, J. L., VIIGIMAA, M., VLACHOPOULOS, C. & XUEREB, R. G. 2013. ESC Guidelines on diabetes,

pre-diabetes, and cardiovascular diseases developed in collaboration with the EASD: the Task Force on diabetes, pre-diabetes, and cardiovascular diseases of the European Society of Cardiology (ESC) and developed in collaboration with the European Association for the Study of Diabetes (EASD). *Eur Heart J,* 34**,** 3035-87.

BACK, M. & HANSSON, G. K. 2015. Anti-inflammatory therapies for atherosclerosis. *Nat Rev Cardiol,* 12**,** 199-211.

BAI, Y., MORGAN, E. E., GIOVANNUCCI, D. R., PIERRE, S. V., PHILIPSON, K. D., ASKARI, A. & LIU, L. 2013. Different roles of the cardiac Na+/Ca2+-exchanger in ouabain-induced inotropy, cell signaling, and hypertrophy. *Am J Physiol Heart Circ Physiol,* 304**,** H427-35.

BALAKUMAR, P., MAUNG, U. K. & JAGADEESH, G. 2016. Prevalence and prevention of cardiovascular disease and diabetes mellitus. *Pharmacol Res,* 113**,** 600-609.

BALLOU, L. M., LIN, R. Z. & COHEN, I. S. 2015. Control of cardiac repolarization by phosphoinositide 3-kinase signaling to ion channels. *Circ Res,* 116**,** 127-37.

BARBER, R. D., HARMER, D. W., COLEMAN, R. A. & CLARK, B. J. 2005. GAPDH as a housekeeping gene: analysis of GAPDH mRNA expression in a panel of 72 human tissues. *Physiol Genomics,* 21**,** 389-95.

BAROUCH, L. A., BERKOWITZ, D. E., HARRISON, R. W., O'DONNELL, C. P. & HARE, J. M. 2003. Disruption of leptin signaling contributes to cardiac hypertrophy independently of body weight in mice. *Circulation,* 108**,** 754-9.

BAROUCH, L. A., GAO, D., CHEN, L., MILLER, K. L., XU, W., PHAN, A. C., KITTLESON, M. M., MINHAS, K. M., BERKOWITZ, D. E., WEI, C. & HARE, J. M. 2006. Cardiac myocyte apoptosis is associated with increased DNA damage and decreased survival in murine models of obesity. *Circ Res,* 98**,** 119-24.

BARROSO, I., BENITO, B., GARCI-JIMENEZ, C., HERNANDEZ, A., OBREGON, M. J. & SANTISTEBAN, P. 1999. Norepinephrine, tri-iodothyronine and insulin upregulate glyceraldehyde-3-phosphate dehydrogenase mRNA during Brown adipocyte differentiation. *Eur J Endocrinol,* 141**,** 169-79.

BAUMGARD, L. H., HAUSMAN, G. J. & SANZ FERNANDEZ, M. V. 2016. Insulin: pancreatic secretion and adipocyte regulation. *Domest Anim Endocrinol,* 54**,** 76-84.

BEETZ, N., HEIN, L., MESZAROS, J., GILSBACH, R., BARRETO, F., MEISSNER, M., HOPPE, U. C., SCHWARTZ, A., HERZIG, S. & MATTHES, J. 2009. Transgenic simulation of human heart failure-like L-type Ca2+-channels: implications for fibrosis and heart rate in mice. *Cardiovasc Res,* 84**,** 396-406.

BEGUIN, P., MAHALAKSHMI, R. N., NAGASHIMA, K., CHER, D. H., IKEDA, H., YAMADA, Y., SEINO, Y. & HUNZIKER, W. 2006. Nuclear sequestration of beta-subunits by Rad and Rem is controlled by 14-3-3 and calmodulin and reveals a novel mechanism for Ca2+ channel regulation. *J Mol Biol,* 355**,** 34-46.

BEGUIN, P., NAGASHIMA, K., GONOI, T., SHIBASAKI, T., TAKAHASHI, K., KASHIMA, Y., OZAKI, N., GEERING, K., IWANAGA, T. & SEINO, S. 2001. Regulation of Ca2+ channel expression at the cell surface by the small G-protein kir/Gem. *Nature,* 411**,** 701-6.

BÉGUIN, P., NG, Y. J., KRAUSE, C., MAHALAKSHMI, R. N., NG, M. Y. & HUNZIKER, W. 2007. RGK small GTP-binding proteins interact with the nucleotide kinase domain of Ca2+-channel beta-subunits via an uncommon effector binding domain. *J Biol Chem,* 282**,** 11509-20.

BELFIORE, A., FRASCA, F., PANDINI, G., SCIACCA, L. & VIGNERI, R. 2009. Insulin receptor isoforms and insulin receptor/insulin-like growth factor receptor hybrids in physiology and disease. *Endocr Rev,* 30**,** 586-623.

BELLES, B., MALECOT, C. O., HESCHELER, J. & TRAUTWEIN, W. 1988. "Run-down" of the Ca current during long whole-cell recordings in guinea pig heart cells: role of phosphorylation and intracellular calcium. *Pflugers Arch,* 411**,** 353-60.

BERS, D. M. 2002. Cardiac excitation-contraction coupling. *Nature,* 415**,** 198-205.

BOCK, T., PAKKENBERG, B. & BUSCHARD, K. 2003. Increased islet volume but unchanged islet number in ob/ob mice. *Diabetes,* 52**,** 1716-22.

BODI, I., MIKALA, G., KOCH, S. E., AKHTER, S. A. & SCHWARTZ, A. 2005. The L-type calcium channel in the heart: the beat goes on. *J Clin Invest,* 115**,** 3306-17.

BÖHNKE, A. K. 2012. Structural remodeling of L-type calcium channel subunits in human and murine atherosclerosis. Doctoral thesis, University of Bonn.

BOUDINA, S., SENA, S., O'NEILL, B. T., TATHIREDDY, P., YOUNG, M. E. & ABEL, E. D. 2005. Reduced mitochondrial oxidative capacity and increased mitochondrial uncoupling impair myocardial energetics in obesity. *Circulation,* 112**,** 2686-95.

BRADFORD, M. M. 1976. A rapid and sensitive method for the quantitation of microgram quantities of protein utilizing the principle of protein-dye binding. *Anal Biochem,* 72**,** 248-54.

BUCHANAN, J., MAZUMDER, P. K., HU, P., CHAKRABARTI, G., ROBERTS, M. W., YUN, U. J., COOKSEY, R. C., LITWIN, S. E. & ABEL, E. D. 2005. Reduced cardiac efficiency and altered substrate metabolism precedes the onset of hyperglycemia and contractile dysfunction in two mouse models of insulin resistance and obesity. *Endocrinology,* 146**,** 5341-9.

BUGGER, H. & ABEL, E. D. 2014. Molecular mechanisms of diabetic cardiomyopathy. *Diabetologia,* 57**,** 660-671.

BUGGER, H. & BODE, C. 2015. The vulnerable myocardium. Diabetic cardiomyopathy. *Hamostaseologie,* 35**,** 17-24.

BURAEI, Z., LUMEN, E., KAUR, S. & YANG, J. 2015. RGK regulation of voltage-gated calcium channels. *Sci China Life Sci,* 58**,** 28-38.

BURAEI, Z. & YANG, J. 2010. The ß subunit of voltage-gated Ca2+ channels. *Physiol Rev,* 90**,** 1461-506.

BURAEI, Z. & YANG, J. 2013. Structure and function of the beta subunit of voltage-gated Ca(2)(+) channels. *Biochim Biophys Acta,* 1828**,** 1530-40.

BURAEI, Z. & YANG, J. 2015. Inhibition of Voltage-Gated Calcium Channels by RGK Proteins. *Curr Mol Pharmacol,* 8**,** 180-7.

BURKS, D. J., FONT DE MORA, J., SCHUBERT, M., WITHERS, D. J., MYERS, M. G., TOWERY, H. H., ALTAMURO, S. L., FLINT, C. L. & WHITE, M. F. 2000. IRS-2 pathways integrate female reproduction and energy homeostasis.

Nature, 407**,** 377-82.

BUSTIN, S. A. 2000. Absolute quantification of mRNA using real-time reverse transcription polymerase chain reaction assays. *J Mol Endocrinol,* 25**,** 169-93.

BUSTIN, S. A., BENES, V., GARSON, J. A., HELLEMANS, J., HUGGETT, J., KUBISTA, M., MUELLER, R., NOLAN, T., PFAFFL, M. W., SHIPLEY, G. L., VANDESOMPELE, J. & WITTWER, C. T. 2009. The MIQE guidelines: minimum information for publication of quantitative real-time PCR experiments. *Clin Chem,* 55**,** 611-22.

CAMPIGLIO, M. & FLUCHER, B. E. 2015. The role of auxiliary subunits for the functional diversity of voltage-gated calcium channels. *J Cell Physiol,* 230**,** 2019-31.

CARVALHEIRA, J. B., RIBEIRO, E. B., FOLLI, F., VELLOSO, L. A. & SAAD, M. J. 2003. Interaction between leptin and insulin signaling pathways differentially affects JAK-STAT and PI 3-kinase-mediated signaling in rat liver. *Biol Chem,* 384**,** 151-9.

CARVALHEIRA, J. B., SILOTO, R. M., IGNACCHITTI, I., BRENELLI, S. L., CARVALHO, C. R., LEITE, A., VELLOSO, L. A., GONTIJO, J. A. & SAAD, M. J. 2001. Insulin modulates leptin-induced STAT3 activation in rat hypothalamus. *FEBS Lett,* 500**,** 119-24.

CATALUCCI, D., ZHANG, D. H., DESANTIAGO, J., AIMOND, F., BARBARA, G., CHEMIN, J., BONCI, D., PICHT, E., RUSCONI, F., DALTON, N. D., PETERSON, K. L., RICHARD, S., BERS, D. M., BROWN, J. H. & CONDORELLI, G. 2009. Akt regulates L-type Ca2+ channel activity by modulating Cavalpha1 protein stability. *J Cell Biol,* 184**,** 923-33.

CATTERALL, W. A. 2011. Voltage-gated calcium channels. *Cold Spring Harb Perspect Biol,* 3**,** a003947.

CATTERALL, W. A., PEREZ-REYES, E., SNUTCH, T. P. & STRIESSNIG, J. 2005. International Union of Pharmacology. XLVIII. Nomenclature and structure-function relationships of voltage-gated calcium channels. *Pharmacol Rev,* 57**,** 411-25.

CATTERALL, W. A., STRIESSNIG, J., SNUTCH, T. P. & PEREZ-REYES, E. 2003. International Union of Pharmacology. XL. Compendium of voltage-gated ion channels: calcium channels. *Pharmacol Rev,* 55**,** 579-81.

CHAN, L. K. & LEUNG, P. S. 2015. Multifaceted interplay among mediators and regulators of intestinal glucose absorption: potential impacts on diabetes research and treatment. *Am J Physiol Endocrinol Metab,* 309**,** E887-99.

CHANG, D. D. & COLECRAFT, H. M. 2015. Rad and Rem are non-canonical G-proteins with respect to the regulatory role of guanine nucleotide binding in CaV 1.2 channel regulation. *J Physiol,* 593**,** 5075-90.

CHANG, L., ZHANG, J., TSENG, Y. H., XIE, C. Q., ILANY, J., BRUNING, J. C., SUN, Z., ZHU, X., CUI, T., YOUKER, K. A., YANG, Q., DAY, S. M., KAHN, C. R. & CHEN, Y. E. 2007. Rad GTPase deficiency leads to cardiac hypertrophy. *Circulation,* 116**,** 2976-83.

CHATZIGEORGIOU, A., HALAPAS, A., KALAFATAKIS, K. & KAMPER, E. 2009. The use of animal models in the study of diabetes mellitus. *In Vivo,* 23**,** 245-58.

CHEN, X., PIACENTINO, V., 3RD, FURUKAWA, S., GOLDMAN, B., MARGULIES, K. B. & HOUSER, S. R. 2002. L-type Ca2+ channel density and regulation are

altered in failing human ventricular myocytes and recover after support with mechanical assist devices. *Circ Res,* 91**,** 517-24.

CHEN, Y. H., LI, M. H., ZHANG, Y., HE, L. L., YAMADA, Y., FITZMAURICE, A., SHEN, Y., ZHANG, H., TONG, L. & YANG, J. 2004. Structural basis of the alpha1-beta subunit interaction of voltage-gated Ca2+ channels. *Nature,* 429**,** 675-80.

CHRISTOFFERSEN, C., BOLLANO, E., LINDEGAARD, M. L., BARTELS, E. D., GOETZE, J. P., ANDERSEN, C. B. & NIELSEN, L. B. 2003. Cardiac lipid accumulation associated with diastolic dysfunction in obese mice. *Endocrinology,* 144**,** 3483-90.

CHU, P. J., LARSEN, J. K., CHEN, C. C. & BEST, P. M. 2004. Distribution and relative expression levels of calcium channel beta subunits within the chambers of the rat heart. *J Mol Cell Cardiol,* 36**,** 423-34.

COLECRAFT, H. M., ALSEIKHAN, B., TAKAHASHI, S. X., CHAUDHURI, D., MITTMAN, S., YEGNASUBRAMANIAN, V., ALVANIA, R. S., JOHNS, D. C., MARBAN, E. & YUE, D. T. 2002. Novel functional properties of Ca(2+) channel beta subunits revealed by their expression in adult rat heart cells. *J Physiol,* 541**,** 435-52.

COOK, S. A., VARELA-CARVER, A., MONGILLO, M., KLEINERT, C., KHAN, M. T., LECCISOTTI, L., STRICKLAND, N., MATSUI, T., DAS, S., ROSENZWEIG, A., PUNJABI, P. & CAMICI, P. G. 2010. Abnormal myocardial insulin signalling in type 2 diabetes and left-ventricular dysfunction. *Eur Heart J,* 31**,** 100-11.

CORRELL, R. N., PANG, C., NIEDOWICZ, D. M., FINLIN, B. S. & ANDRES, D. A. 2008. The RGK family of GTP-binding proteins: regulators of voltage-dependent calcium channels and cytoskeleton remodeling. *Cell Signal,* 20**,** 292-300.

CRAIG, M. E., JEFFERIES, C., DABELEA, D., BALDE, N., SETH, A., DONAGHUE, K. C., INTERNATIONAL SOCIETY FOR, P. & ADOLESCENT, D. 2014. ISPAD Clinical Practice Consensus Guidelines 2014. Definition, epidemiology, and classification of diabetes in children and adolescents. *Pediatr Diabetes,* 15 Suppl 20**,** 4-17.

DANDAMUDI, S., SLUSSER, J., MAHONEY, D. W., REDFIELD, M. M., RODEHEFFER, R. J. & CHEN, H. H. 2014. The prevalence of diabetic cardiomyopathy: a population-based study in Olmsted County, Minnesota. *J Card Fail,* 20**,** 304-9.

DE JONGH, K. S., MURPHY, B. J., COLVIN, A. A., HELL, J. W., TAKAHASHI, M. & CATTERALL, W. A. 1996. Specific phosphorylation of a site in the full-length form of the alpha 1 subunit of the cardiac L-type calcium channel by adenosine 3',5'-cyclic monophosphate-dependent protein kinase. *Biochemistry,* 35**,** 10392-402.

DE SIMONE, G., DEVEREUX, R. B., CHINALI, M., LEE, E. T., GALLOWAY, J. M., BARAC, A., PANZA, J. A. & HOWARD, B. V. 2010. Diabetes and incident heart failure in hypertensive and normotensive participants of the Strong Heart Study. *J Hypertens,* 28**,** 353-60.

DEL GUERRA, S., LUPI, R., MARSELLI, L., MASINI, M., BUGLIANI, M., SBRANA, S., TORRI, S., POLLERA, M., BOGGI, U., MOSCA, F., DEL PRATO, S. & MARCHETTI, P. 2005. Functional and molecular defects of pancreatic islets in human type 2 diabetes. *Diabetes,* 54**,** 727-35.

DIZAYEE, S. 2011. Cardiac Gαi2 Protein Function and Regulation of High-Voltage-Gated L-type Calcium Channels. Doctoral thesis, University of Bonn.

ERTEL, E. A., CAMPBELL, K. P., HARPOLD, M. M., HOFMANN, F., MORI, Y., PEREZ-REYES, E., SCHWARTZ, A., SNUTCH, T. P., TANABE, T., BIRNBAUMER, L., TSIEN, R. W. & CATTERALL, W. A. 2000. Nomenclature of voltage-gated calcium channels. *Neuron,* 25**,** 533-5.

FABISCH, C. 2010. Modulation des L-Typ Calciumkanals Cav1.2 in Diabetischer Kardiomyopathie. Doctoral thesis, University of Cologne.

FAN, M., BURAEI, Z., LUO, H. R., LEVENSON-PALMER, R. & YANG, J. 2010. Direct inhibition of P/Q-type voltage-gated Ca2+ channels by Gem does not require a direct Gem/Cavbeta interaction. *Proc Natl Acad Sci U S A,* 107**,** 14887-92.

FAUCONNIER, J., LANNER, J. T., ZHANG, S. J., TAVI, P., BRUTON, J. D., KATZ, A. & WESTERBLAD, H. 2005. Insulin and inositol 1,4,5-trisphosphate trigger abnormal cytosolic Ca2+ transients and reveal mitochondrial Ca2+ handling defects in cardiomyocytes of ob/ob mice. *Diabetes,* 54**,** 2375-81.

FEIJOO-BANDIN, S., PORTOLES, M., ROSELLO-LLETI, E., RIVERA, M., GONZALEZ-JUANATEY, J. R. & LAGO, F. 2015. 20 years of leptin: Role of leptin in cardiomyocyte physiology and physiopathology. *Life Sci,* 140**,** 10-8.

FERNANDEZ-FORMOSO, G., PEREZ-SIEIRA, S., GONZALEZ-TOUCEDA, D., DIEGUEZ, C. & TOVAR, S. 2015. Leptin, 20 years of searching for glucose homeostasis. *Life Sci,* 140**,** 4-9.

FINLIN, B. S., CORRELL, R. N., PANG, C., CRUMP, S. M., SATIN, J. & ANDRES, D. A. 2006. Analysis of the complex between Ca2+ channel beta-subunit and the Rem GTPase. *J Biol Chem,* 281**,** 23557-66.

FINLIN, B. S., SHAO, H., KADONO-OKUDA, K., GUO, N. & ANDRES, D. A. 2000. Rem2, a new member of the Rem/Rad/Gem/Kir family of Ras-related GTPases. *Biochem J,* 347 Pt 1**,** 223-31.

FLYNN, R. & ZAMPONI, G. W. 2010. Regulation of calcium channels by RGK proteins. *Channels (Austin),* 4**,** 434-9.

FOERSTER, K., GRONER, F., MATTHES, J., KOCH, W. J., BIRNBAUMER, L. & HERZIG, S. 2003. Cardioprotection specific for the G protein Gi2 in chronic adrenergic signaling through beta 2-adrenoceptors. *Proc Natl Acad Sci U S A,* 100**,** 14475-80.

FU, Q., XU, B., LIU, Y., PARIKH, D., LI, J., LI, Y., ZHANG, Y., RIEHLE, C., ZHU, Y., RAWLINGS, T., SHI, Q., CLARK, R. B., CHEN, X., ABEL, E. D. & XIANG, Y. K. 2014. Insulin inhibits cardiac contractility by inducing a Gi-biased beta2-adrenergic signaling in hearts. *Diabetes,* 63**,** 2676-89.

FU, Z., GILBERT, E. R. & LIU, D. 2013. Regulation of insulin synthesis and secretion and pancreatic Beta-cell dysfunction in diabetes. *Curr Diabetes Rev,* 9**,** 25-53.

FUKUI, A., TAKAHASHI, N., NAKADA, C., MASAKI, T., KUME, O., SHINOHARA, T., TESHIMA, Y., HARA, M. & SAIKAWA, T. 2013. Role of leptin signaling in the pathogenesis of angiotensin II-mediated atrial fibrosis and fibrillation. *Circ Arrhythm Electrophysiol,* 6**,** 402-9.

GARCIA-BARRADO, M. J., IGLESIAS-OSMA, M. C., MORENO-VIEDMA, V., PASTOR MANSILLA, M. F., GONZALEZ, S. S., CARRETERO, J., MORATINOS, J. & BURKS, D. J. 2011. Differential sensitivity to adrenergic

stimulation underlies the sexual dimorphism in the development of diabetes caused by Irs-2 deficiency. *Biochem Pharmacol,* 81**,** 279-88.

GHARIB, M., TAO, H., FUNGWE, T. V. & HAJRI, T. 2016. Cluster Differentiating 36 (CD36) Deficiency Attenuates Obesity-Associated Oxidative Stress in the Heart. *PLoS One,* 11**,** e0155611.

GOONASEKERA, S. A., HAMMER, K., AUGER-MESSIER, M., BODI, I., CHEN, X., ZHANG, H., REIKEN, S., ELROD, J. W., CORRELL, R. N., YORK, A. J., SARGENT, M. A., HOFMANN, F., MOOSMANG, S., MARKS, A. R., HOUSER, S. R., BERS, D. M. & MOLKENTIN, J. D. 2012. Decreased cardiac L-type Ca(2)(+) channel activity induces hypertrophy and heart failure in mice. *J Clin Invest,* 122**,** 280-90.

GREENBAUM, D., COLANGELO, C., WILLIAMS, K. & GERSTEIN, M. 2003. Comparing protein abundance and mRNA expression levels on a genomic scale. *Genome Biol,* 4**,** 117.

GRÜNDEMANN, D. & KOEPSELL, H. 1994. Ethidium bromide staining during denaturation with glyoxal for sensitive detection of RNA in agarose gel electrophoresis. *Anal Biochem,* 216**,** 459-61.

GRUVER, E. J., MORGAN, J. P., STAMBLER, B. S. & GWATHMEY, J. K. 1994. Uniformity of calcium channel number and isometric contraction in human right and left ventricular myocardium. *Basic Res Cardiol,* 89**,** 139-48.

HALL, M. E., HARMANCEY, R. & STEC, D. E. 2015. Lean heart: Role of leptin in cardiac hypertrophy and metabolism. *World J Cardiol,* 7**,** 511-24.

HALTER, B., GONZALEZ DE AGUILAR, J. L., RENE, F., PETRI, S., FRICKER, B., ECHANIZ-LAGUNA, A., DUPUIS, L., LARMET, Y. & LOEFFLER, J. P. 2010. Oxidative stress in skeletal muscle stimulates early expression of Rad in a mouse model of amyotrophic lateral sclerosis. *Free Radic Biol Med,* 48**,** 915-23.

HALUZIK, M., COLOMBO, C., GAVRILOVA, O., CHUA, S., WOLF, N., CHEN, M., STANNARD, B., DIETZ, K. R., LE ROITH, D. & REITMAN, M. L. 2004. Genetic background (C57BL/6J versus FVB/N) strongly influences the severity of diabetes and insulin resistance in ob/ob mice. *Endocrinology,* 145**,** 3258-64.

HAMILL, O. P., MARTY, A., NEHER, E., SAKMANN, B. & SIGWORTH, F. J. 1981. Improved patch-clamp techniques for high-resolution current recording from cells and cell-free membrane patches. *Pflugers Arch,* 391**,** 85-100.

HARDIE, D. G. 2012. Organismal carbohydrate and lipid homeostasis. *Cold Spring Harb Perspect Biol,* 4.

HARRISON, R. R., KOLB, I., KODANDARAMAIAH, S. B., CHUBYKIN, A. A., YANG, A., BEAR, M. F., BOYDEN, E. S. & FOREST, C. R. 2015. Microchip amplifier for in vitro, in vivo, and automated whole cell patch-clamp recording. *J Neurophysiol,* 113**,** 1275-82.

HERING, S., BERJUKOW, S., SOKOLOV, S., MARKSTEINER, R., WEISS, R. G., KRAUS, R. & TIMIN, E. N. 2000. Molecular determinants of inactivation in voltage-gated Ca2+ channels. *J Physiol,* 528 Pt 2**,** 237-49.

HEUBACH, J. F., TREBESS, I., WETTWER, E., HIMMEL, H. M., MICHEL, M. C., KAUMANN, A. J., KOCH, W. J., HARDING, S. E. & RAVENS, U. 1999. L-type calcium current and contractility in ventricular myocytes from mice overexpressing the cardiac beta 2-adrenoceptor. *Cardiovasc Res,* 42**,** 173-82.

HIRASHIMA, Y., TSURUZOE, K., KODAMA, S., IGATA, M., TOYONAGA, T., UEKI, K., KAHN, C. R. & ARAKI, E. 2003. Insulin down-regulates insulin receptor substrate-2 expression through the phosphatidylinositol 3-kinase/Akt pathway. *J Endocrinol,* 179**,** 253-66.

HODGKIN, A. L., HUXLEY, A. F. & KATZ, B. 1952. Measurement of current-voltage relations in the membrane of the giant axon of Loligo. *J Physiol,* 116**,** 424-48.

HOFMANN, F., FLOCKERZI, V., KAHL, S. & WEGENER, J. W. 2014. L-type CaV1.2 calcium channels: from in vitro findings to in vivo function. *Physiol Rev,* 94**,** 303-26.

HONG, T. T., SMYTH, J. W., CHU, K. Y., VOGAN, J. M., FONG, T. S., JENSEN, B. C., FANG, K., HALUSHKA, M. K., RUSSELL, S. D., COLECRAFT, H., HOOPES, C. W., OCORR, K., CHI, N. C. & SHAW, R. M. 2012. BIN1 is reduced and Cav1.2 trafficking is impaired in human failing cardiomyocytes. *Heart Rhythm,* 9**,** 812-20.

HORIUCHI-HIROSE, M., KASHIHARA, T., NAKADA, T., KUREBAYASHI, N., SHIMOJO, H., SHIBAZAKI, T., SHENG, X., YANO, S., HIROSE, M., HONGO, M., SAKURAI, T., MORIIZUMI, T., UEDA, H. & YAMADA, M. 2011. Decrease in the density of t-tubular L-type Ca2+ channel currents in failing ventricular myocytes. *Am J Physiol Heart Circ Physiol,* 300**,** H978-88.

HULLIN, R., KHAN, I. F., WIRTZ, S., MOHACSI, P., VARADI, G., SCHWARTZ, A. & HERZIG, S. 2003. Cardiac L-type calcium channel beta-subunits expressed in human heart have differential effects on single channel characteristics. *J Biol Chem,* 278**,** 21623-30.

HULLIN, R., MATTHES, J., VON VIETINGHOFF, S., BODI, I., RUBIO, M., D'SOUZA, K., FRIEDRICH KHAN, I., ROTTLÄNDER, D., HOPPE, U. C., MOHACSI, P., SCHMITTECKERT, E., GILSBACH, R., BÜNEMANN, M., HEIN, L., SCHWARTZ, A. & HERZIG, S. 2007. Increased expression of the auxiliary beta(2)-subunit of ventricular L-type Ca(2)+ channels leads to single-channel activity characteristic of heart failure. *PLoS One,* 2**,** e292.

ILANY, J., BILAN, P. J., KAPUR, S., CALDWELL, J. S., PATTI, M. E., MARETTE, A. & KAHN, C. R. 2006. Overexpression of Rad in muscle worsens diet-induced insulin resistance and glucose intolerance and lowers plasma triglyceride level. *Proc Natl Acad Sci U S A,* 103**,** 4481-6.

INGALLS, A. M., DICKIE, M. M. & SNELL, G. D. 1950. Obese, a new mutation in the house mouse. *J Hered,* 41**,** 317-8.

JHUN, B. S., J, O. U., WANG, W., HA, C. H., ZHAO, J., KIM, J. Y., WONG, C., DIRKSEN, R. T., LOPES, C. M. & JIN, Z. G. 2012. Adrenergic signaling controls RGK-dependent trafficking of cardiac voltage-gated L-type Ca2+ channels through PKD1. *Circ Res,* 110**,** 59-70.

JIA, G., DEMARCO, V. G. & SOWERS, J. R. 2016. Insulin resistance and hyperinsulinaemia in diabetic cardiomyopathy. *Nat Rev Endocrinol,* 12**,** 144-53.

JIANG, F., LI, S., PAN, L. & JIA, C. 2015. Association of the G1057D polymorphism in insulin receptor substrate 2 gene with type 2 diabetes mellitus: a meta-analysis. *J Diabetes Complications,* 29**,** 731-6.

KANNEL, W. B., HJORTLAND, M. & CASTELLI, W. P. 1974. Role of diabetes in congestive heart failure: the Framingham study. *Am J Cardiol,* 34**,** 29-34.

KARMAZINOVA, M. & LACINOVA, L. 2010. Measurement of cellular excitability by whole cell patch clamp technique. *Physiol Res,* 59 Suppl 1**,** S1-7.

KIDO, Y., BURKS, D. J., WITHERS, D., BRUNING, J. C., KAHN, C. R., WHITE, M. F. & ACCILI, D. 2000. Tissue-specific insulin resistance in mice with mutations in the insulin receptor, IRS-1, and IRS-2. *J Clin Invest,* 105**,** 199-205.

KIM, A., MILLER, K., JO, J., KILIMNIK, G., WOJCIK, P. & HARA, M. 2009. Islet architecture: A comparative study. *Islets,* 1**,** 129-36.

KIM, J. A., WEI, Y. & SOWERS, J. R. 2008. Role of mitochondrial dysfunction in insulin resistance. *Circ Res,* 102**,** 401-14.

KING, A. J. 2012. The use of animal models in diabetes research. *Br J Pharmacol,* 166**,** 877-94.

KING, M., KINGERY, J. & CASEY, B. 2012. Diagnosis and evaluation of heart failure. *Am Fam Physician,* 85**,** 1161-8.

KONNER, A. C. & BRUNING, J. C. 2012. Selective insulin and leptin resistance in metabolic disorders. *Cell Metab,* 16**,** 144-52.

KOUSSOUNADIS, A., LANGDON, S. P., UM, I. H., HARRISON, D. J. & SMITH, V. A. 2015. Relationship between differentially expressed mRNA and mRNA-protein correlations in a xenograft model system. *Sci Rep,* 5**,** 10775.

KUBISTA, M., ANDRADE, J. M., BENGTSSON, M., FOROOTAN, A., JONAK, J., LIND, K., SINDELKA, R., SJOBACK, R., SJOGREEN, B., STROMBOM, L., STAHLBERG, A. & ZORIC, N. 2006. The real-time polymerase chain reaction. *Mol Aspects Med,* 27**,** 95-125.

KUBOTA, N., TOBE, K., TERAUCHI, Y., ETO, K., YAMAUCHI, T., SUZUKI, R., TSUBAMOTO, Y., KOMEDA, K., NAKANO, R., MIKI, H., SATOH, S., SEKIHARA, H., SCIACCHITANO, S., LESNIAK, M., AIZAWA, S., NAGAI, R., KIMURA, S., AKANUMA, Y., TAYLOR, S. I. & KADOWAKI, T. 2000. Disruption of insulin receptor substrate 2 causes type 2 diabetes because of liver insulin resistance and lack of compensatory beta-cell hyperplasia. *Diabetes,* 49**,** 1880-9.

LANGENDORFF, O. 1895. Untersuchungen am überlebenden Säugetierherzen. *Pflügers Archiv* 61

291 - 332.

LAVILLE, M., AUBOEUF, D., KHALFALLAH, Y., VEGA, N., RIOU, J. P. & VIDAL, H. 1996. Acute regulation by insulin of phosphatidylinositol-3-kinase, Rad, Glut 4, and lipoprotein lipase mRNA levels in human muscle. *J Clin Invest,* 98**,** 43-9.

LEE, A. W. & COX, R. D. 2011. Use of mouse models in studying type 2 diabetes mellitus. *Expert Rev Mol Med,* 13**,** e1.

LEITER, E. H. 1992. Variation in the severity and duration of hyperglycemia in the C57BL/6J-ob/ob (obese) mouse *[Available: https://www.jax.org/news-and-insights/1992/october/variation-in-the-severity-and-duration-of-hyperglycemia-in-the-c57bl6j-obob].* Bar Harbor, Maine: The Jackson Laboratory.

LI, S. Y., YANG, X., CEYLAN-ISIK, A. F., DU, M., SREEJAYAN, N. & REN, J. 2006. Cardiac contractile dysfunction in Lep/Lep obesity is accompanied by NADPH oxidase activation, oxidative modification of sarco(endo)plasmic reticulum Ca2+-ATPase and myosin heavy chain isozyme switch. *Diabetologia,* 49**,** 1434-46.

LINDSTROM, P. 2007. The physiology of obese-hyperglycemic mice [ob/ob mice]. *ScientificWorldJournal,* 7**,** 666-85.

LIPUT, D. J., LU, V. B., DAVIS, M. I., PUHL, H. L. & IKEDA, S. R. 2016. Rem2, a member of the RGK family of small GTPases, is enriched in nuclei of the basal ganglia. *Sci Rep,* 6**,** 25137.

LIVAK, K. J. & SCHMITTGEN, T. D. 2001. Analysis of relative gene expression data using real-time quantitative PCR and the 2(-Delta Delta C(T)) Method. *Methods,* 25**,** 402-8.

LODISH, H., BERK, A., KAISER, C. A., KRIEGER, M., P., S. M., A., B., H., P. & P., M. (eds.) 2007. *Molecular Cell Biology,* New York: W. H. Freeman.

LOUCH, W. E., SHEEHAN, K. A. & WOLSKA, B. M. 2011. Methods in cardiomyocyte isolation, culture, and gene transfer. *J Mol Cell Cardiol,* 51**,** 288-98.

LU, Z., BALLOU, L. M., JIANG, Y. P., COHEN, I. S. & LIN, R. Z. 2011. Restoration of defective L-type Ca2+ current in cardiac myocytes of type 2 diabetic db/db mice by Akt and PKC-iota. *J Cardiovasc Pharmacol,* 58**,** 439-45.

LU, Z., JIANG, Y. P., XU, X. H., BALLOU, L. M., COHEN, I. S. & LIN, R. Z. 2007. Decreased L-type Ca2+ current in cardiac myocytes of type 1 diabetic Akita mice due to reduced phosphatidylinositol 3-kinase signaling. *Diabetes,* 56**,** 2780-9.

MADAMANCHI, A. 2007. Beta-adrenergic receptor signaling in cardiac function and heart failure. *Mcgill J Med,* 10**,** 99-104.

MAGUIRE, J., SANTORO, T., JENSEN, P., SIEBENLIST, U., YEWDELL, J. & KELLY, K. 1994. Gem: an induced, immediate early protein belonging to the Ras family. *Science,* 265**,** 241-4.

MAGYAR, J., KIPER, C. E., SIEVERT, G., CAI, W., SHI, G. X., CRUMP, S. M., LI, L., NIEDERER, S., SMITH, N., ANDRES, D. A. & SATIN, J. 2012. Rem-GTPase regulates cardiac myocyte L-type calcium current. *Channels (Austin),* 6**,** 166-73.

MANNING, J. R., YIN, G., KAMINSKI, C. N., MAGYAR, J., FENG, H. Z., PENN, J., SIEVERT, G., THOMPSON, K., JIN, J. P., ANDRES, D. A. & SATIN, J. 2013. Rad GTPase deletion increases L-type calcium channel current leading to increased cardiac contraction. *J Am Heart Assoc,* 2**,** e000459.

MARDILOVICH, K., PANKRATZ, S. L. & SHAW, L. M. 2009. Expression and function of the insulin receptor substrate proteins in cancer. *Cell Commun Signal,* 7**,** 14.

MARGETIC, S., GAZZOLA, C., PEGG, G. G. & HILL, R. A. 2002. Leptin: a review of its peripheral actions and interactions. *Int J Obes Relat Metab Disord,* 26**,** 1407-33.

MARK, A. L., SHAFFER, R. A., CORREIA, M. L., MORGAN, D. A., SIGMUND, C. D. & HAYNES, W. G. 1999. Contrasting blood pressure effects of obesity in leptin-deficient ob/ob mice and agouti yellow obese mice. *J Hypertens,* 17**,** 1949-53.

MARTIN, S. S., QASIM, A. & REILLY, M. P. 2008. Leptin resistance: a possible interface of inflammation and metabolism in obesity-related cardiovascular disease. *J Am Coll Cardiol,* 52**,** 1201-10.

MARTINEZ-MARTINEZ, E., JURADO-LOPEZ, R., CERVANTES-ESCALERA, P.,

CACHOFEIRO, V. & MIANA, M. 2014. Leptin, a mediator of cardiac damage associated with obesity. *Horm Mol Biol Clin Investig,* 18**,** 3-14.

MASAKI, T., CHIBA, S., NOGUCHI, H., YASUDA, T., TOBE, K., SUZUKI, R., KADOWAKI, T. & YOSHIMATSU, H. 2004. Obesity in insulin receptor substrate-2-deficient mice: disrupted control of arcuate nucleus neuropeptides. *Obes Res,* 12**,** 878-85.

MAZUMDER, P. K., O'NEILL, B. T., ROBERTS, M. W., BUCHANAN, J., YUN, U. J., COOKSEY, R. C., BOUDINA, S. & ABEL, E. D. 2004. Impaired cardiac efficiency and increased fatty acid oxidation in insulin-resistant ob/ob mouse hearts. *Diabetes,* 53**,** 2366-74.

MEISSNER, M., WEISSGERBER, P., LONDONO, J. E., PRENEN, J., LINK, S., RUPPENTHAL, S., MOLKENTIN, J. D., LIPP, P., NILIUS, B., FREICHEL, M. & FLOCKERZI, V. 2011. Moderate calcium channel dysfunction in adult mice with inducible cardiomyocyte-specific excision of the cacnb2 gene. *J Biol Chem,* 286**,** 15875-82.

MEZA, U., BEQOLLARI, D., ROMBERG, C. F., PAPADOPOULOS, S. & BANNISTER, R. A. 2013. Potent inhibition of L-type Ca2+ currents by a Rad variant associated with congestive heart failure. *Biochem Biophys Res Commun,* 439**,** 270-4.

MINHAS, K. M., KHAN, S. A., RAJU, S. V., PHAN, A. C., GONZALEZ, D. R., SKAF, M. W., LEE, K., TEJANI, A. D., SALIARIS, A. P., BAROUCH, L. A., O'DONNELL, C. P., EMALA, C. W., BERKOWITZ, D. E. & HARE, J. M. 2005. Leptin repletion restores depressed {beta}-adrenergic contractility in ob/ob mice independently of cardiac hypertrophy. *J Physiol,* 565**,** 463-74.

MOON, B. C. & FRIEDMAN, J. M. 1997. The molecular basis of the obese mutation in ob2J mice. *Genomics,* 42**,** 152-6.

Mouse Genome Database (MGD). Mouse Strain Datasheet - 000632. *Mouse Genome Informatics website [Available: https://www.jax.org/strain/000632].* Bar Habor, Maine: The Jackson Laboratory; cited 02.2017.

MOYERS, J. S., ZHU, J. & KAHN, C. R. 1998. Effects of phosphorylation on function of the Rad GTPase. *Biochem J,* 333 (Pt 3)**,** 609-14.

MUKHERJEE, R. & SPINALE, F. G. 1998. L-type calcium channel abundance and function with cardiac hypertrophy and failure: a review. *J Mol Cell Cardiol,* 30**,** 1899-916.

MUNZBERG, H. & MORRISON, C. D. 2015. Structure, production and signaling of leptin. *Metabolism,* 64**,** 13-23.

MURATA, M., CINGOLANI, E., MCDONALD, A. D., DONAHUE, J. K. & MARBAN, E. 2004. Creation of a genetic calcium channel blocker by targeted gem gene transfer in the heart. *Circ Res,* 95**,** 398-405.

NAJAFI, A., SEQUEIRA, V., KUSTER, D. W. & VAN DER VELDEN, J. 2016. beta-adrenergic receptor signalling and its functional consequences in the diseased heart. *Eur J Clin Invest,* 46**,** 362-74.

NEELY, A. & HIDALGO, P. 2014. Structure-function of proteins interacting with the alpha1 pore-forming subunit of high-voltage-activated calcium channels. *Front Physiol,* 5**,** 209.

NEHER, E., SAKMANN, B. & STEINBACH, J. H. 1978. The extracellular patch clamp: a method for resolving currents through individual open channels in

biological membranes. *Pflugers Arch,* 375**,** 219-28.

NEUMAIER, F., DIBUE-ADJEI, M., HESCHELER, J. & SCHNEIDER, T. 2015. Voltage-gated calcium channels: Determinants of channel function and modulation by inorganic cations. *Prog Neurobiol,* 129**,** 1-36.

NEWSHOLME, E. A. & DIMITRIADIS, G. 2001. Integration of biochemical and physiologic effects of insulin on glucose metabolism. *Exp Clin Endocrinol Diabetes,* 109 Suppl 2**,** S122-34.

NICHOLS, G. A., GULLION, C. M., KORO, C. E., EPHROSS, S. A. & BROWN, J. B. 2004. The incidence of congestive heart failure in type 2 diabetes: an update. *Diabetes Care,* 27**,** 1879-84.

OGDEN, D. & STANFIELD, P. R. 1987. Patch clamp techniques for single channel and whole-cell recording. *Microelectrode techniques: the Plymouth workshop handbook.* Cambridge: The Company of Biologists.

OLIVEIRA, J. M., REBUFFAT, S. A., GASA, R. & GOMIS, R. 2014. Targeting type 2 diabetes: lessons from a knockout model of insulin receptor substrate 2. *Can J Physiol Pharmacol,* 92**,** 613-20.

PANENI, F. 2014. 2013 ESC/EASD guidelines on the management of diabetes and cardiovascular disease: established knowledge and evidence gaps. *Diab Vasc Dis Res,* 11**,** 5-10.

PANG, C., CRUMP, S. M., JIN, L., CORRELL, R. N., FINLIN, B. S., SATIN, J. & ANDRES, D. A. 2010. Rem GTPase interacts with the proximal CaV1.2 C-terminus and modulates calcium-dependent channel inactivation. *Channels (Austin),* 4**,** 192-202.

PARK, J. & PETERS, P. A. 2014. Mortality from diabetes mellitus, 2004 to 2008: A multiple-cause-of-death analysis. *Health Rep,* 25**,** 12-6.

PEREIRA, L. 2006. Mechanisms of [Ca2+]i Transient Decrease in Cardiomyopathy of db/db Type 2 Diabetic Mice. *Diabetes,* 55**,** 608-615.

PFAFFL, M. W., HORGAN, G. W. & DEMPFLE, L. 2002. Relative expression software tool (REST) for group-wise comparison and statistical analysis of relative expression results in real-time PCR. *Nucleic Acids Res,* 30**,** e36.

PJANIC, M., MILLER, C. L., WIRKA, R., KIM, J. B., DIRENZO, D. M. & QUERTERMOUS, T. 2016. Genetics and Genomics of Coronary Artery Disease. *Curr Cardiol Rep,* 18**,** 102.

PONIKOWSKI, P., VOORS, A. A., ANKER, S. D., BUENO, H., CLELAND, J. G., COATS, A. J., FALK, V., GONZALEZ-JUANATEY, J. R., HARJOLA, V. P., JANKOWSKA, E. A., JESSUP, M., LINDE, C., NIHOYANNOPOULOS, P., PARISSIS, J. T., PIESKE, B., RILEY, J. P., ROSANO, G. M., RUILOPE, L. M., RUSCHITZKA, F., RUTTEN, F. H., VAN DER MEER, P., AUTHORS/TASK FORCE, M. & DOCUMENT, R. 2016. 2016 ESC Guidelines for the diagnosis and treatment of acute and chronic heart failure: The Task Force for the diagnosis and treatment of acute and chronic heart failure of the European Society of Cardiology (ESC). Developed with the special contribution of the Heart Failure Association (HFA) of the ESC. *Eur J Heart Fail,* 18**,** 891-975.

QI, Y., XU, Z., ZHU, Q., THOMAS, C., KUMAR, R., FENG, H., DOSTAL, D. E., WHITE, M. F., BAKER, K. M. & GUO, S. 2013. Myocardial loss of IRS1 and IRS2 causes heart failure and is controlled by p38alpha MAPK during insulin resistance. *Diabetes,* 62**,** 3887-900.

RAE, J. L. & LEVIS, R. A. 1992. Glass technology for patch clamp electrodes. *Methods Enzymol,* 207**,** 66-92.

REN, J. 2004. Leptin and hyperleptinemia - from friend to foe for cardiovascular function. *J Endocrinol,* 181**,** 1-10.

REN, J., DONG, F., CAI, G. J., ZHAO, P., NUNN, J. M., WOLD, L. E. & PEI, J. 2010. Interaction between age and obesity on cardiomyocyte contractile function: role of leptin and stress signaling. *PLoS One,* 5**,** e10085.

REYNET, C. & KAHN, C. R. 1993. Rad: a member of the Ras family overexpressed in muscle of type II diabetic humans. *Science,* 262**,** 1441-4.

RICHARD, S., LECLERCQ, F., LEMAIRE, S., PIOT, C. & NARGEOT, J. 1998. Ca2+ currents in compensated hypertrophy and heart failure. *Cardiovasc Res,* 37**,** 300-11.

RIEHLE, C. & ABEL, E. D. 2016. Insulin Signaling and Heart Failure. *Circ Res,* 118**,** 1151-69.

RIEHLE, C., WENDE, A. R., SENA, S., PIRES, K. M., PEREIRA, R. O., ZHU, Y., BUGGER, H., FRANK, D., BEVINS, J., CHEN, D., PERRY, C. N., DONG, X. C., VALDEZ, S., RECH, M., SHENG, X., WEIMER, B. C., GOTTLIEB, R. A., WHITE, M. F. & ABEL, E. D. 2013. Insulin receptor substrate signaling suppresses neonatal autophagy in the heart. *J Clin Invest,* 123**,** 5319-33.

RIEHLE, C., WENDE, A. R., ZHU, Y., OLIVEIRA, K. J., PEREIRA, R. O., JAISHY, B. P., BEVINS, J., VALDEZ, S., NOH, J., KIM, B. J., MOREIRA, A. B., WEATHERFORD, E. T., MANIVEL, R., RAWLINGS, T. A., RECH, M., WHITE, M. F. & ABEL, E. D. 2014. Insulin receptor substrates are essential for the bioenergetic and hypertrophic response of the heart to exercise training. *Mol Cell Biol,* 34**,** 3450-60.

ROUGIER, J. S. & ABRIEL, H. 2016. Cardiac voltage-gated calcium channel macromolecular complexes. *Biochim Biophys Acta,* 1863**,** 1806-12.

RUBLER, S., DLUGASH, J., YUCEOGLU, Y. Z., KUMRAL, T., BRANWOOD, A. W. & GRISHMAN, A. 1972. New type of cardiomyopathy associated with diabetic glomerulosclerosis. *Am J Cardiol,* 30**,** 595-602.

RUSCONI, F., CERIOTTI, P., MIRAGOLI, M., CARULLO, P., SALVARANI, N., ROCCHETTI, M., DI PASQUALE, E., ROSSI, S., TESSARI, M., CAPRARI, S., CAZADE, M., KUNDERFRANCO, P., CHEMIN, J., BANG, M. L., POLTICELLI, F., ZAZA, A., FAGGIAN, G., CONDORELLI, G. & CATALUCCI, D. 2016. Peptidomimetic Targeting of Cavbeta2 Overcomes Dysregulation of the L-Type Calcium Channel Density and Recovers Cardiac Function. *Circulation*.

SANCHEZ-ALONSO, J. L., BHARGAVA, A., O'HARA, T., GLUKHOV, A. V., SCHOBESBERGER, S., BHOGAL, N., SIKKEL, M. B., MANSFIELD, C., KORCHEV, Y. E., LYON, A. R., PUNJABI, P. P., NIKOLAEV, V. O., TRAYANOVA, N. A. & GORELIK, J. 2016. Microdomain-Specific Modulation of L-Type Calcium Channels Leads to Triggered Ventricular Arrhythmia in Heart Failure. *Circ Res,* 119**,** 944-55.

SASAKI, T., SHIBASAKI, T., BEGUIN, P., NAGASHIMA, K., MIYAZAKI, M. & SEINO, S. 2005. Direct inhibition of the interaction between alpha-interaction domain and beta-interaction domain of voltage-dependent Ca2+ channels by Gem. *J Biol Chem,* 280**,** 9308-12.

SASSON, Y., NAVON-PERRY, L., HUPPERT, D. & HIRSCH, J. A. 2011. RGK family

G-domain:GTP analog complex structures and nucleotide-binding properties. *J Mol Biol,* 413**,** 372-89.

SCHROEDER, F., HANDROCK, R., BEUCKELMANN, D. J., HIRT, S., HULLIN, R., PRIEBE, L., SCHWINGER, R. H., WEIL, J. & HERZIG, S. 1998. Increased availability and open probability of single L-type calcium channels from failing compared with nonfailing human ventricle. *Circulation,* 98**,** 969-76.

SESTI, G., FEDERICI, M., HRIBAL, M. L., LAURO, D., SBRACCIA, P. & LAURO, R. 2001. Defects of the insulin receptor substrate (IRS) system in human metabolic disorders. *FASEB J,* 15**,** 2099-111.

SHAW, R. M. & COLECRAFT, H. M. 2013. L-type calcium channel targeting and local signalling in cardiac myocytes. *Cardiovasc Res,* 98**,** 177-86.

SLOAN, C., TUINEI, J., NEMETZ, K., FRANDSEN, J., SOTO, J., WRIDE, N., SEMPOKUYA, T., ALEGRIA, L., BUGGER, H. & ABEL, E. D. 2011. Central leptin signaling is required to normalize myocardial fatty acid oxidation rates in caloric-restricted ob/ob mice. *Diabetes,* 60**,** 1424-34.

SOWERS, J. R. & LESTER, M. A. 1999. Diabetes and cardiovascular disease. *Diabetes Care,* 22 Suppl 3**,** C14-20.

SU, Y. R., CHIUSA, M., BRITTAIN, E., HEMNES, A. R., ABSI, T. S., LIM, C. C. & DI SALVO, T. G. 2015. Right ventricular protein expression profile in end-stage heart failure. *Pulm Circ,* 5**,** 481-97.

SZANTO, I. & KAHN, C. R. 2000. Selective interaction between leptin and insulin signaling pathways in a hepatic cell line. *Proc Natl Acad Sci U S A,* 97**,** 2355-60.

TAEGTMEYER, H. 1995. One hundred years ago: Oscar Langendorff and the birth of cardiac metabolism. *Can J Cardiol,* 11**,** 1030-5.

TAKAHASHI, T., ALLEN, P. D., LACRO, R. V., MARKS, A. R., DENNIS, A. R., SCHOEN, F. J., GROSSMAN, W., MARSH, J. D. & IZUMO, S. 1992. Expression of dihydropyridine receptor (Ca2+ channel) and calsequestrin genes in the myocardium of patients with end-stage heart failure. *J Clin Invest,* 90**,** 927-35.

TAYLOR, S., WAKEM, M., DIJKMAN, G., ALSARRAJ, M. & NGUYEN, M. 2010. A practical approach to RT-qPCR-Publishing data that conform to the MIQE guidelines. *Methods,* 50**,** S1-5.

VAN DEN BERGH, A., VANDERPER, A., VANGHELUWE, P., DESJARDINS, F., NEVELSTEEN, I., VERRETH, W., WUYTACK, F., HOLVOET, P., FLAMENG, W., BALLIGAND, J. L. & HERIJGERS, P. 2008. Dyslipidaemia in type II diabetic mice does not aggravate contractile impairment but increases ventricular stiffness. *Cardiovasc Res,* 77**,** 371-9.

VAN PETEGEM, F., CLARK, K. A., CHATELAIN, F. C. & MINOR, D. L., JR. 2004. Structure of a complex between a voltage-gated calcium channel beta-subunit and an alpha-subunit domain. *Nature,* 429**,** 671-5.

VAN PETEGEM, F. & MINOR, D. L., JR. 2006. The structural biology of voltage-gated calcium channel function and regulation. *Biochem Soc Trans,* 34**,** 887-93.

VANGUILDER, H. D., VRANA, K. E. & FREEMAN, W. M. 2008. Twenty-five years of quantitative PCR for gene expression analysis. *Biotechniques,* 44**,** 619-26.

VELEZ, M., KOHLI, S. & SABBAH, H. N. 2014. Animal models of insulin resistance and heart failure. *Heart Fail Rev,* 19**,** 1-13.

VIARD, P., BUTCHER, A. J., HALET, G., DAVIES, A., NURNBERG, B., HEBLICH, F. & DOLPHIN, A. C. 2004. PI3K promotes voltage-dependent calcium channel trafficking to the plasma membrane. *Nat Neurosci,* 7**,** 939-46.

VIKRAMADITHYAN, R. K., HU, Y., NOH, H. L., LIANG, C. P., HALLAM, K., TALL, A. R., RAMASAMY, R. & GOLDBERG, I. J. 2005. Human aldose reductase expression accelerates diabetic atherosclerosis in transgenic mice. *J Clin Invest,* 115**,** 2434-43.

WANG, B., CHANDRASEKERA, P. C. & PIPPIN, J. J. 2014. Leptin- and leptin receptor-deficient rodent models: relevance for human type 2 diabetes. *Curr Diabetes Rev,* 10**,** 131-45.

WANG, C. C., GOALSTONE, M. L. & DRAZNIN, B. 2004. Molecular mechanisms of insulin resistance that impact cardiovascular biology. *Diabetes,* 53**,** 2735-40.

WANG, G., ZHU, X., XIE, W., HAN, P., LI, K., SUN, Z., WANG, Y., CHEN, C., SONG, R., CAO, C., ZHANG, J., WU, C., LIU, J. & CHENG, H. 2010. Rad as a novel regulator of excitation-contraction coupling and beta-adrenergic signaling in heart. *Circ Res,* 106**,** 317-27.

WASIM, M., AWAN, F. R., NAJAM, S. S., KHAN, A. R. & KHAN, H. N. 2016. Role of Leptin Deficiency, Inefficiency, and Leptin Receptors in Obesity. *Biochem Genet*.

WEISS, S., OZ, S., BENMOCHA, A. & DASCAL, N. 2013. Regulation of cardiac L-type Ca(2)(+) channel CaV1.2 via the beta-adrenergic-cAMP-protein kinase A pathway: old dogmas, advances, and new uncertainties. *Circ Res,* 113**,** 617-31.

WESTERMEIER, F., RIQUELME, J. A., PAVEZ, M., GARRIDO, V., DIAZ, A., VERDEJO, H. E., CASTRO, P. F., GARCIA, L. & LAVANDERO, S. 2016. New Molecular Insights of Insulin in Diabetic Cardiomyopathy. *Front Physiol,* 7**,** 125.

WINSLOW, R. L., WALKER, M. A. & GREENSTEIN, J. L. 2016. Modeling calcium regulation of contraction, energetics, signaling, and transcription in the cardiac myocyte. *Wiley Interdiscip Rev Syst Biol Med,* 8**,** 37-67.

WITHERS, C., SATIN, J. & ANDRES, D. 2015. Rad Phosphorylation Via β-Adrenergic Signaling Modulates Its Association with the Calcium Channel. *The FASEB Journal,* 29.

WITHERS, D. J., BURKS, D. J., TOWERY, H. H., ALTAMURO, S. L., FLINT, C. L. & WHITE, M. F. 1999. Irs-2 coordinates Igf-1 receptor-mediated beta-cell development and peripheral insulin signalling. *Nat Genet,* 23**,** 32-40.

WITHERS, D. J., GUTIERREZ, J. S., TOWERY, H., BURKS, D. J., REN, J. M., PREVIS, S., ZHANG, Y., BERNAL, D., PONS, S., SHULMAN, G. I., BONNER-WEIR, S. & WHITE, M. F. 1998. Disruption of IRS-2 causes type 2 diabetes in mice. *Nature,* 391**,** 900-4.

World Health Organization 2016. GLOBAL REPORT ON DIABETES *[Available: http://www.who.int/diabetes/global-report/en/]*; cited 02.2017.

WORTHAM, M. & SANDER, M. 2016. Mechanisms of beta-cell functional adaptation to changes in workload. *Diabetes Obes Metab,* 18 Suppl 1**,** 78-86.

XU, X., MARX, S. O. & COLECRAFT, H. M. 2010. Molecular mechanisms, and selective pharmacological rescue, of Rem-inhibited CaV1.2 channels in heart. *Circ Res,* 107**,** 620-30.

YADA, H., MURATA, M., SHIMODA, K., YUASA, S., KAWAGUCHI, H., IEDA, M., ADACHI, T., MURATA, M., OGAWA, S. & FUKUDA, K. 2007. Dominant negative suppression of Rad leads to QT prolongation and causes ventricular arrhythmias via modulation of L-type Ca2+ channels in the heart. *Circ Res,* 101**,** 69-77.

YANG, L., KATCHMAN, A., MORROW, J. P., DOSHI, D. & MARX, S. O. 2011. Cardiac L-type calcium channel (Cav1.2) associates with gamma subunits. *FASEB J,* 25**,** 928-36.

YANG, T., PUCKERIN, A. & COLECRAFT, H. M. 2012. Distinct RGK GTPases differentially use alpha1- and auxiliary beta-binding-dependent mechanisms to inhibit CaV1.2/CaV2.2 channels. *PLoS One,* 7**,** e37079.

YANG, T., SUHAIL, Y., DALTON, S., KERNAN, T. & COLECRAFT, H. M. 2007. Genetically encoded molecules for inducibly inactivating CaV channels. *Nat Chem Biol,* 3**,** 795-804.

YANG, T., XU, X., KERNAN, T., WU, V. & COLECRAFT, H. M. 2010. Rem, a member of the RGK GTPases, inhibits recombinant CaV1.2 channels using multiple mechanisms that require distinct conformations of the GTPase. *J Physiol,* 588**,** 1665-81.

YANG, X. D., XIANG, D. X. & YANG, Y. Y. 2016. Role of E3 ubiquitin ligases in insulin resistance. *Diabetes Obes Metab,* 18**,** 747-54.

YE, J. 2013. Mechanisms of insulin resistance in obesity. *Front Med,* 7**,** 14-24.

YILMAZ, S., CANPOLAT, U., AYDOGDU, S. & ABBOUD, H. E. 2015. Diabetic Cardiomyopathy; Summary of 41 Years. *Korean Circ J,* 45**,** 266-72.

YU, J., LI, W., LI, Y., ZHAO, J., WANG, L., DONG, D., PAN, Z. & YANG, B. 2011. Activation of beta(3)-adrenoceptor promotes rapid pacing-induced atrial electrical remodeling in rabbits. *Cell Physiol Biochem,* 28**,** 87-96.

ZAMPONI, G. W., STRIESSNIG, J., KOSCHAK, A. & DOLPHIN, A. C. 2015. The Physiology, Pathology, and Pharmacology of Voltage-Gated Calcium Channels and Their Future Therapeutic Potential. *Pharmacol Rev,* 67**,** 821-70.

ZHANG, Y., PROENCA, R., MAFFEI, M., BARONE, M., LEOPOLD, L. & FRIEDMAN, J. M. 1994. Positional cloning of the mouse obese gene and its human homologue. *Nature,* 372**,** 425-32.

ZHOU, Y. & RUI, L. 2013. Leptin signaling and leptin resistance. *Front Med,* 7**,** 207-22.

ZIMMER, H. G. 1998. The Isolated Perfused Heart and Its Pioneers. *News Physiol Sci,* 13**,** 203-210.

8 Appendix

8.1 Exemplary genotyping results

All mice included in this study were genotyped unambiguously. Figures 8.1-8.3 show exemplary genotyping results.

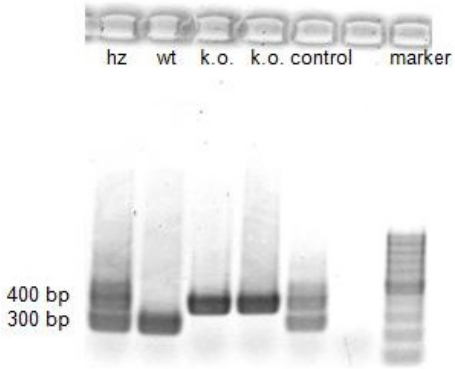

Figure 8.1 **Exemplary genotyping results for IRS 2-k.o. mice:** DNA fragments were visualized at 300 bp for the wildtype band and at 400 bp for the mutant band (hz = heterozygous, wt = wildtype, k.o. = knockout, bp = base pairs).

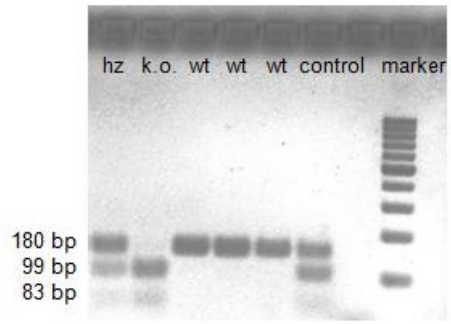

Figure 8.2 **Exemplary genotyping results for ob/ob mice:** bands were detected at 83 bp and 99 bp for mutant and at 180 bp for wildtype (hz = heterozygous, wt = wildtype, k.o. = knockout, bp = base pairs).

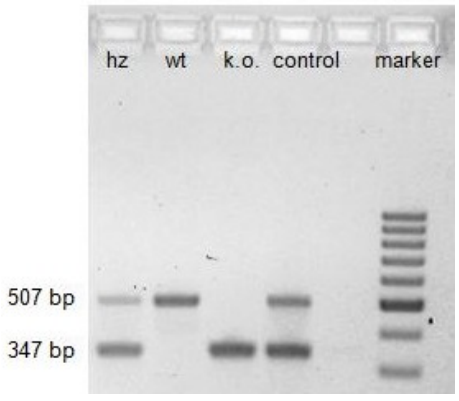

Figure 8.3 **Exemplary genotyping results for Rad-k.o. mice**: wildtype was identified via a band at 507 bp and mutant via a band at 347 bp (hz = heterozygous, wt = wildtype, k.o. = knockout, bp = base pairs).

8.2 Overview: blood glucose values, body weights, ventricle weights and ventricle-to-body weight ratios

Table 8.1 **Overview of blood glucose levels, body weights, ventricle weights and ventricle-to-body weight ratios of the investigated mouse lines** (* = $p < 0.05$ mutant vs. age-matched wt in Student's t-test; # = $p < 0.05$ vs. 28 week old mice of the same genotype in Student's t-test; values = mean ± SEM; N = number of mice).

Genotype, age	Blood glucose level [mg/dl]	Body weight [g]	Ventricle weight [mg]	Ventricle-to-body weight ratio [mg/g]
Wildtype, 16 weeks	158 ± 5 (N = 58)	**24.4 ± 0.5**$^{\#}$ (N = 62)	127.9 ± 5.3 (N = 36)	5.4 ± 0.2 (N = 36)
IRS 2-k.o., 16 weeks	**207 ± 10*** (N = 62)	**25.7 ± 0.5**$^{\#}$ (N = 63)	128.3 ± 3.4 (N = 34)	5.0 ± 0.1 (N = 34)
Ob/ob, 16 weeks	**270 ± 29**$^{*,\#}$ (N = 20)	**46.6 ± 2.0**$^{*,\#}$ (N = 20)	**124.4 ± 3.9**$^{\#}$ (N = 13)	**2.8 ± 0.2*** (N = 13)
Rad-k.o., 16 weeks	**140 ± 4*** (N = 27)	**26.9 ± 0.7*** (N = 27)	121.4 ± 4.1 (N = 21)	**4.6 ± 0.1*** (N = 21)
Ob/ob x Rad-k.o., 16 weeks	**291 ± 26*** (N = 25)	**51.1 ± 0.9**$^{*,\#}$ (N = 25)	**136.8 ± 4.7**$^{\#}$ (N = 16)	**2.7 ± 0.1*** (N = 16)
Wildtype, 28 weeks	168 ± 6 (N = 41)	27.6 ± 0.6 (N = 42)	142.7 ± 6.4 (N = 21)	5.2 ± 0.2 (N = 21)
IRS 2-k.o., 28 weeks	**239 ± 22*** (N = 30)	27.6 ± 0.9 (N = 30)	126.3 ± 5.6 (N = 23)	4.8 ± 0.2 (N = 23)
Ob/ob, 28 weeks	203 ± 18 (N = 33)	**60.3 ± 1.5*** (N = 33)	157.7 ± 4.6 (N = 16)	**2.8 ± 0.2*** (N = 16)
Rad-k.o., 28 weeks	**151 ± 5*** (N = 49)	27.9 ± 0.5 (N = 49)	**120.9 ± 8.3*** (N = 21)	**4.6 ± 0.1*** (N = 21)
Ob/ob x Rad-k.o., 28 weeks	**276 ± 43*** (N = 9)	**59.7 ± 1.6*** (N = 9)	**170.8 ± 7.9*** (N = 8)	**2.8 ± 0.1*** (N = 8)

8.3 Whole-cell patch-clamp experiments

8.3.1 Mean cell capacitances of patched cells

Patched cells had a mean cell capacitance (C_m) of 157 ± 6 pF (n = 85; number of patched cells). In one-way ANOVA (Bonferroni's Post Test) membrane capacities of patched cells did not differ significantly independent of mouse genotype and age from that cells were isolated (figure 8.4). Therefore experiments were technically comparable and there was no evidence of cellular hypertrophy.

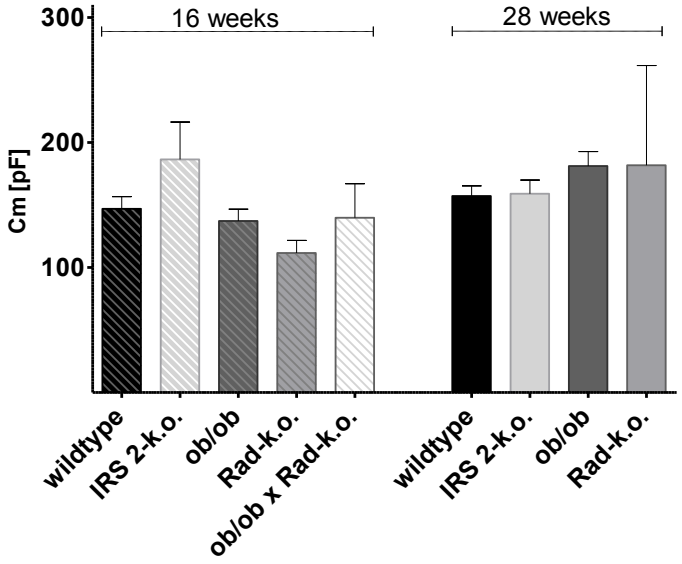

Figure 8.4 **Mean cell capacities (C_m):** in one-way ANOVA (Bonferroni's Post Test) membrane capacities of patched cells did not differ significantly independent of mouse genotype and age from that cells were isolated. Therefore experiments were technically comparable and there was no evidence of cellular hypertrophy (n = 2-17 per group).

8.3.2 Overview: whole-cell patch-clamp results

Table 8.2 **Maximum current density (mean I_{max}) and potential of mean I_{max} determined out of raw data points of the I/V curve** (* = p < 0.05 mutant vs. age-matched wildtype in Student's t-test; values = mean ± SEM; n = number of patched cells).

Genotype, age	Mean I_{max} [pA/pF]	V [mV] at mean I_{max}
Wildtype, 16 weeks (n = 17)	-10.92 ± 0.90	2.94 ± 1.43
IRS 2-k.o., 16 weeks (n = 11)	**-7.79 ± 0.79***	0.91 ± 1.63
Ob/ob, 16 weeks (n = 10)	-10.75 ± 0.65	0.00 ± 0.00
Rad-k.o., 16 weeks (n = 5)	**-20.12 ± 1.49***	**-4.00 ± 2.45***
Ob/ob x Rad-k.o., 16 weeks (n = 5)	**-21.48 ± 1.10***	**-8.00 ± 2.00***
Wildtype, 28 weeks (n = 13)	-8.91 ± 0.54	4.62 ± 1.44
IRS 2-k.o., 28 weeks (n = 11)	-11.22 ± 1.27	1.82 ± 1.22
Ob/ob, 28 weeks (n = 11)	-8.44 ± 0.43	**10.00 ± 1.91***
Rad-k.o., 28 weeks (n = 2)	**-21.58 ± 5.05***	**-5.00 ± 5.00***

Table 8.3 **Potential of half maximal activation $V_{0.5act}$, slope factor, maximum current density (mean I_{max}) and potential of mean I_{max} determined out of fitted I/V curve** (* = p < 0.05 mutant vs. age-matched wildtype in Student's t-test; values = mean ± SEM; n = number of patched cells).

Genotype, age	Potential of half maximal activation $V_{0.5act}$ [mV]	Slope factor	Mean I_{max} [pA/pF]	V [mV] at mean I_{max}
Wildtype, 16 weeks (n = 17)	-8.69 ± 1.06	5.05 ± 0.25	-11.13 ± 0.91	1.86 ± 1.12
IRS 2-k.o., 16 weeks (n = 11)	-8.71 ± 1.26	5.60 ± 0.60	**-7.89 ± 0.81***	1.69 ± 1.24
Ob/ob, 16 weeks (n = 10)	**-11.72 ± 0.59***	**4.17 ± 0.18***	-11.04 ± 0.69	**-1.67 ± 0.67***
Rad-k.o., 16 weeks (n = 5)	**-14.74 ± 1.33***	**3.97 ± 0.10***	**-20.72 ± 1.62***	**-4.49 ± 1.30***
Ob/ob x Rad-k.o., 16 weeks (n = 5)	**-17.06 ± 1.71***	**3.65 ± 0.13***	**-21.71 ± 1.53***	**-5.31 ± 1.84***
Wildtype, 28 weeks (n = 13)	-7.51 ± 0.96	5.01 ± 0.14	-9.12 ± 0.55	3.12 ± 0.88
IRS 2-k.o., 28 weeks (n = 11)	**-10.88 ± 0.89***	5.11 ± 0.21	-11.51 ± 1.30	0.53 ± 1.06
Ob/ob, 28 weeks (n = 11)	**-4.86 ± 0 .67***	5.32 ± 0.18	-8.71 ± 0.44	**5.67 ± 0.60***
Rad-k.o., 28 weeks (n = 2)	**-16.13 ± 0.08***	**3.37 ± 0.37***	**-22.24 ± 5.36***	**-6.60 ± 0.83***

Table 8.4 **Time-dependent inactivation:** Tau (determined out of fitted raw calcium current traces; * = $p < 0.05$ mutant vs. age-matched wildtype in Student's t-test; values = mean ± SEM; n = number of patched cells).

Genotype, age	**Tau (τ)**					
	-10 mV	0 mV	10 mV	20 mV	30 mV	40 mV
Wildtype, 16 weeks (n = 17)	37.44 ± 2.82	31.67 ± 1.54	40.14 ± 1.37	49.28 ± 1.45	55.08 ± 1.50	54.53 ± 1.46
IRS 2-k.o., 16 weeks (n = 11)	34.90 ± 3.31	32.22 ± 1.19	42.04 ± 1.68	51.74 ± 1.61	57.21 ± 1.48	55.45 ± 1.98
Ob/ob, 16 weeks (n = 10)	**25.10 ± 1.41***	33.09 ± 1.32	**44.78 ± 1.58***	53.92 ± 1.58	57.80 ± 1.25	56.00 ± 0.94
Rad-k.o., 16 weeks (n = 5)	**24.49 ± 2.71***	27.67 ± 1.01	36.62 ± 1.35	46.63 ± 1.22	55.87 ± 1.00	**61.76 ± 2.34***
Ob/ob x Rad-k.o., 16 weeks (n = 5)	28.12 ± 6.08	34.12 ± 4.35	43.27 ± 3.30	48.59 ± 3.10	55.23 ± 4.26	61.08 ± 4.77
Wildtype, 28 weeks (n = 13)	36.16 ± 3.27	35.58 ± 1.01	46.56 ± 1.21	57.29 ± 1.80	62.65 ± 1.82	60.57 ± 1.92
IRS 2-k.o., 28 weeks (n = 11)	32.34 ± 2.61	33.11 ± 1.12	**40.88 ± 1.14***	**49.68 ± 1.65***	**54.45 ± 1.92***	**53.75 ± 2.03***
Ob/ob, 28 weeks (n = 11)	**54.48 ± 5.48***	34.09 ± 1.28	**40.12 ± 1.09***	**47.27 ± 1.17***	**51.87 ± 1.20***	**51.97 ± 1.32***
Rad-k.o., 28 weeks (n = 2)	22.27 ± 5.84	**28.66 ± 1.64***	40.13 ± 3.46	52.47 ± 3.90	61.33 ± 2.70	67.50 ± 0.95

Table 8.5 **Potential of half maximal inactivation $V_{0.5inact}$ and slope factor determined out of fitted SSI curve** (* = $p < 0.05$ mutant vs. age-matched wildtype in Student's t-test; values = mean ± SEM; n = number of patched cells).

Genotype, age	Potential of half maximal inactivation $V_{0.5inact}$ [mV]	Slope factor
Wildtype, 16 weeks (n= 7)	-25.20 ± 1.01	4.65 ± 0.38
IRS 2-k.o., 16 weeks (n = 4)	-24.94 ± 1.33	4.05 ± 0.53
Ob/ob, 16 weeks (n = 4)	-26.27 ± 0.67	5.05 ± 0.38
Rad-k.o., 16 weeks (n = 4)	-28.17 ± 2.18	3.85 ± 0.21
Ob/ob x Rad-k.o., 16 weeks (n = 4)	-28.73 ± 1.21	4.20 ± 0.47
Wildtype, 28 weeks (n = 9)	-25.31 ± 0.84	4.70 ± 0.20
IRS 2-k.o., 28 weeks (n = 4)	**-29.23 ± 1.06***	5.52 ± 0.38
Ob/ob, 28 weeks (n = 12)	-24.77 ± 0.71	4.53 ± 0.28
Rad-k.o., 28 weeks (n = 3)	-23.95 ± 1.56	**3.76 ± 0.28***

Table 8.6 **Plateau, tau, half-time (determined out of fitted recovery curve) and the relative current after 375 ms of recovery time** (I2/I1) (* = $p < 0.05$ mutant vs. age-matched wildtype in Student's t-test; values = mean ± SEM; n = number of patched cells).

Genotype, age	Plateau	tau	Half-time	I2/I1 after 375 ms
Wildtype, 16 weeks (n = 22)	0.87 ± 0.02	150.28 ± 8.87	104.17 ± 6.15	0.81 ± 0.02
IRS 2-k.o., 16 weeks (n = 7)	0.87 ± 0.03	155.17 ± 10.89	107.58 ± 7.55	0.81 ± 0.03
Ob/ob, 16 weeks (n = 10)	0.82 ± 0.02	151.22 ± 8.28	104.82 ± 5.74	0.78 ± 0.02
Rad-k.o., 16 weeks (n = 4)	0.82 ± 0.04	**206.20 ± 27.75***	**142.89 ± 19.24***	**0.70 ± 0.06***
Ob/ob x Rad-k.o., 16 weeks (n = 4)	0.85 ± 0.03	**224.45 ± 13.70***	**155.58 ± 9.48***	**0.70 ± 0.03***
Wildtype, 28 weeks (n = 12)	0.81 ± 0.03	159.91 ± 6.31	110.84 ± 4.37	0.76 ± 0.02
IRS 2-k.o., 28 weeks (n = 9)	0.81 ± 0.04	155.74 ± 9.01	107.95 ± 6.24	0.75 ± 0.04
Ob/ob, 28 weeks (n = 12)	0.84 ± 0.02	173.26 ± 7.70	120.08 ± 5.34	0.76 ± 0.02
Rad-k.o., 28 weeks (n = 2)	0.87 ± 0.00	156.70 ± 27.30	108.61 ± 18.89	0.79 ± 0.04

8.4 Cardiac myocytes purification assay

Equilibrium density gradient centrifugation with Percoll medium is generally used in order to purify cell fractions. In this study it was planned to purify the enzymatically isolated adult murine ventricular myocytes.

After Percoll density gravity centrifugation, four fractions of cells were obtained, as described in chapter 2.5. All layers were analyzed visually under a microscope. Dead cells were apparent in the interface between fraction 1 and fraction 2, but concentrated at the bottom of the tube. Despite several variations of centrifugation time and/or Percoll density experiments failed: cardiac myocytes, which should concentrate in fraction 3, were also visible in equal parts in fraction 2. Besides, other living cell types were also observable in the middle fractions, though representing a minor part (figure 8.5). Any change of the protocol worsened the outcome of the assay, i.e. resulted in diffuse cell distributions or no more living cardiomyocytes. Due to failure of purification of adult murine ventricular myocytes, for further expression analyses whole-ventricle homogenates were used.

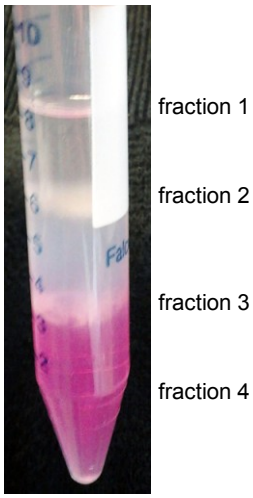

Figure 8.5 **Fractions obtained after Percoll density gravity centrifugation:** cardiac myocytes, which should concentrate in fraction 3, were also visible in equal parts in fraction 2. Other cell types were visible in these fractions as well.

8.5 qRT-PCR experiments

The ventricular mRNA expression of the RGK proteins, $Ca_v1.2$ and the $Ca_vß$-subunits was detected via qRT-PCR. As expected Rem 2, which has been described to be highly expressed in brain and kidney (Liput et al., 2016, Finlin et al., 2000), was not detectable in ventricular tissue and thus was only measured the first experiments to detect a putative unexpected expression under diseased conditions. As control mRNA a murine brain cDNA sample was used.
Data were obtained from N = 5–6 animals per group, 2-3 mice per sex assumed. To improve validity of the results maximal one mice per litter was used.

8.5.1 Primer efficiency tests

For primer efficiency tests three different cDNA dilution series were used (consisting of four or five dilutions, respectively). For each dilution series cDNA was reverse transcribed from a different adult murine ventricle sample. Per dilution series and primer pair one or two efficiency tests were conducted.
Efficiencies of two genes were compared by blotting the Ct values obtained via qRT-PCR against the log template amount of the cDNA dilution series used. The obtained standard curves almost went in parallel (figure 8.6). Therefore efficiencies were considered as comparable (Bustin et al., 2009). Calculated mean primer efficiencies were within a range of 86% and 99% (figure 8.7).

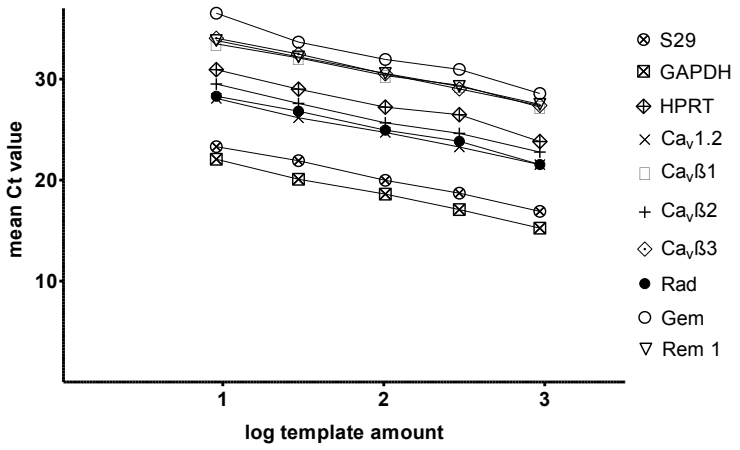

Figure 8.6 **Primer efficiency I:** the tested primers showed comparable efficiencies with almost parallel standard curves.

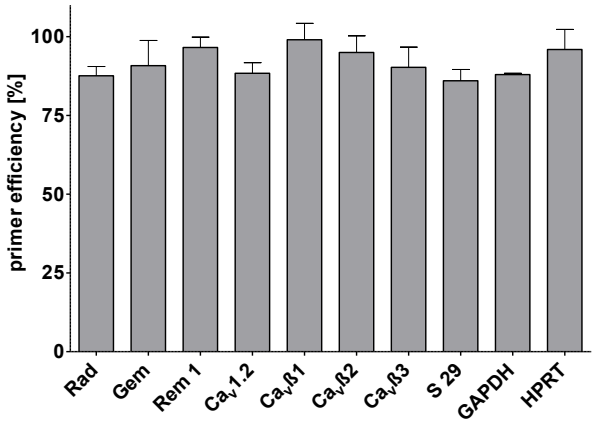

Figure 8.7 **Primer efficiency II:** calculated primer efficiencies were within a range of 86% and 99%.

8.5.2 Quality of isolated mRNA

The quality of isolated mRNA is essential for obtainment of reliable qRT-PCR data. Each mRNA sample was checked via UV-Vis spectrophotometer. Only mRNA with a 260 nm/280 nm ratio between 1.8 and 2.0 was used for further experiments. A ratio of 2.1–2.2 was also accepted if separation into 18 S rRNA (~ 1.9 kbp) and 28 S rRNA (~ 4.7 kbp) in agarose gel electrophoresis proved to be of good quality. Solely RNA, which showed two sharp bands with 28 S rRNA band intensity doubled compared to 18 S rRNA, was taken for reverse transcription into cDNA. This additional check was not applied to all samples, only randoms were picked out. The results demonstrate that the method used to isolate mRNA was suitable to obtain intact mRNA without contaminations (figure 8.8).

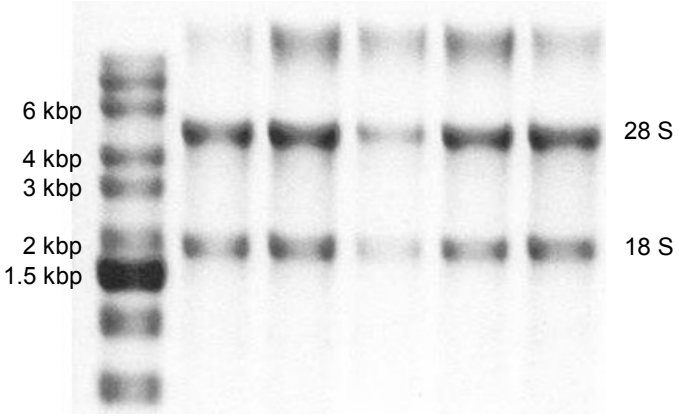

Figure 8.8 **Qualitative RNA analysis** of murine ventricle samples: in intact total RNA 18 S and 28 S RNA bands are clearly visible in a ratio of 1:2 (kbp = kilo base pairs).

8.5.3 Quality of cDNA / qRT-PCR results

After completion of a qRT-PCR cycling protocol a melting curve analysis of all samples was attached to check for product purity and to exclude primer dimers (chapter 2.6.5). Each qRT-PCR conducted showed clear melting curves specific for the particular target (figure 8.9). A random sample of cDNA probes was picked out and applied on an agarose gel to check for correct product size. cDNA products detected were within the expected range of 60–160 bp band size (figure 8.10).

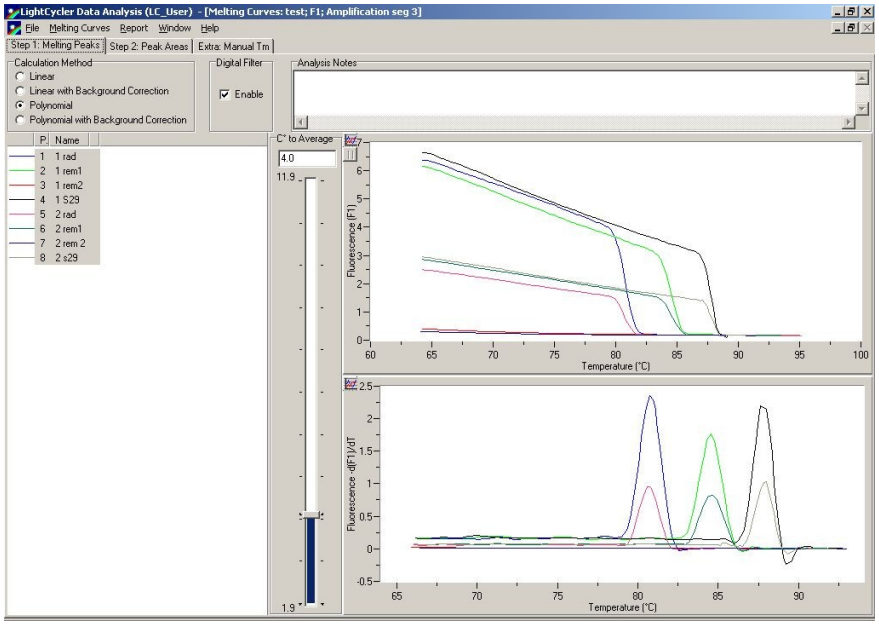

Figure 8.9 **Detection of melting curve analysis, exemplary for Rad, Rem 1 und S 29:** melting curves were specific for the particular target, e. g. the curves for Rad always appeared at 82°C, for Rem 1 at 84°C and for S 29 at 88°C.

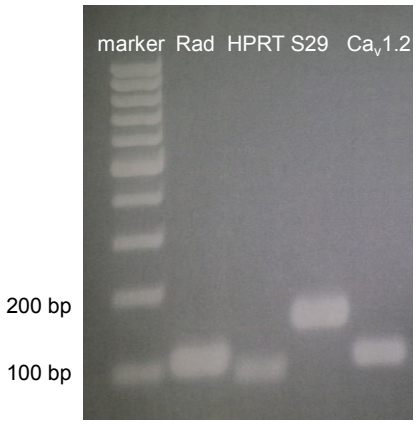

Figure 8.10 **Detection of cDNA bands:** cDNA was detected via agarose gel electrophoresis in order to check for correct product size. E. g. the addition of Rad primer pairs to the reaction setup resulted in cDNA with 105 bp amplicon length (bp = base pairs).

8.5.4 Stability of housekeeping gene expression

At the beginning of data analysis the expression of S 29, HPRT and GAPDH was compared in order to find an appropriate housekeeping gene. Although GAPDH is one of the most commonly used housekeeping genes, its stable expression in diabetic heart tissue is questionable. GAPDH is an enzyme that is necessary in the glycolytic pathway (Barber et al., 2005). In diabetic tissues the expression can be altered, e.g. GAPDH was downregulated in the heart of type 1 diabetic dogs. (Barroso et al., 1999, Alexander et al., 1988). However, in the investigated samples GAPDH expression was stable. As illustrated in figure 8.11, S 29, HPRT and GAPDH were expressed stably throughout all genotypes and ages. Therefore data of the present study were normalized to S29, GAPDH and HPRT simultaneously (REST-2009© analysis). The mean Ct value of S 29 (mixed genotypes and ages, n = 59) showed the smallest coefficient of variation, thus demonstrating S 29 as the most stable expressed reference gene (S29: 2.57%, HPRT: 3.08%, GAPDH : 3.34%, n = 57-59). Hence S 29 was used as normalization gene for $2^{-\Delta\Delta Ct}$ analysis.

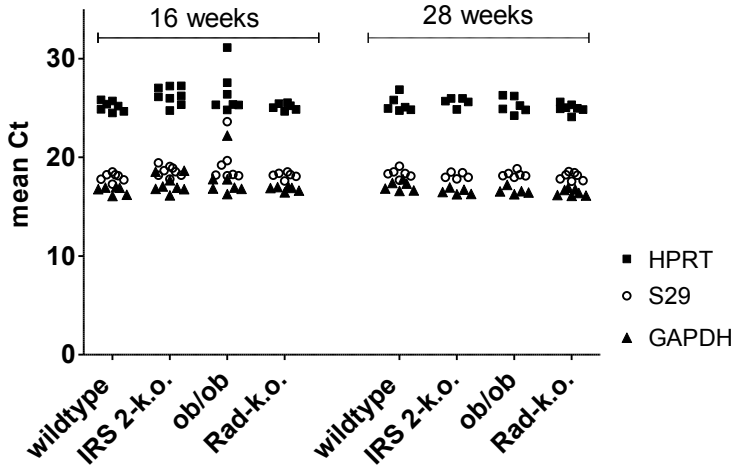

Figure 8.11 **Stability of housekeeping gene expression**: S 29, HPRT and GAPDH were expressed stably throughout all genotypes and ages (HPRT/S29/GAPDH: n = 5-8 per genotype and age group).

8.5.5 Overview: qRT-PCR results

Table 8.7 **Overview of relative mRNA expression levels of Rad, Gem and Rem 1 compared to age-matched wildtype** (* = $p < 0.05$ in hypothesis test of REST-2009© software tool [S29, HPRT and GAPDH as reference genes]; # = $p < 0.05$ in Student's t-test of delta Ct values [S29 as reference gene]; values = mean ± SEM; N = 5-6 ventricles per genotype and age group; nd = not detectable).

Genotype, age	Rad mRNA expression		Gem mRNA expression		Rem 1 mRNA expression	
	REST-2009©	$2^{-\Delta\Delta Ct}$	REST-2009©	$2^{-\Delta\Delta Ct}$	REST-2009©	$2^{-\Delta\Delta Ct}$
IRS 2-k.o., 16 weeks	**2.01*** ± 1.24 – 3.37	**2.06#** ± 0.17	1.46 ± 1.02– 2.20	1.44 ± 0.09	1.46 ± 0.95 – 2.45	1.45 ± 0.13
Ob/ob, 16 weeks	1.42 ± 0.89 – 2.41	1.55 ± 0.27	1.22 ± 0.78–1.91	1.36 ± 0.26	0.87 ± 0.59–1.48	0.96 ± 0.17
Rad-k.o., 16 weeks	nd	nd	**1.92*** ± 1.29–2.82	**2.07#** ± 0.23	1.17 ± 0.74–1.77	1.19 ± 0.08
IRS 2-k.o., 28 weeks	1.22 ± 1.02–1.58	1.24 ± 0.11	1.15 ± 0.96–1.46	1.15 ± 0.11	1.24 ± 0.97–1.65	1.24 ± 0.13
Ob/ob, 28 weeks	1.24 ± 0.95–1.77	1.50 ± 0.23	0.91 ± 0.63–1.20	1.04 ± 0.12	0.96 ± 0.77–1.19	1.08 ± 0.08
Rad-k.o., 28 weeks	nd	nd	**2.13*** ± 1.74–2.67	**2.58#** ± 0.28	**1.28*** ± 1.05–1.67	1.46 ± 0.16

Table 8.8 **Overview of relative mRNA expression levels of $Ca_v1.2$ compared to age-matched wildtype** (* = $p < 0.05$ in hypothesis test of REST-2009© software tool [S29, HPRT and GAPDH as reference genes]; # = $p < 0.05$ in Student's t-test of delta Ct values [S29 as reference gene]; values = mean ± SEM; N = 5-6 ventricles per genotype and age group).

Genotype, age	$Ca_v1.2$ mRNA expression	
	REST-2009©	$2^{-\Delta\Delta Ct}$
IRS 2-k.o., 16 weeks	1.23 ± 0.86-1.88	1.20 ± 0.09
Ob/ob, 16 weeks	0.84 ± 0.52-1.45	0.97 ± 0.19
Rad-k.o., 16 weeks	1.01 ± 0.70-1.55	1.03 ± 0.07
IRS 2-k.o., 28 weeks	1.03 ± 0.76-1.46	1.05 ± 0.14
Ob/ob, 28 weeks	**0.76*** ± 0.65 – 0.93	0.86 ± 0.12
Rad-k.o., 28 weeks	**0.50*** ± 0.35-0.68	**0.57#** ± 0.10

Table 8.9 **Overview of relative mRNA expression levels of the Ca_vß-subunits compared to age-matched wildtype** (* = $p < 0.05$ in hypothesis test of REST-2009© software tool [S29, HPRT and GAPDH as reference genes]; # = $p < 0.05$ in Student's t-test of delta Ct values [S29 as reference gene]; values = mean ± SEM; N = 5-6 ventricles per genotype and age group).

Genotype, age	Ca_vß1 subunit mRNA expression		Ca_vß2 subunit mRNA expression		Ca_vß3 subunit mRNA expression	
	REST-2009©	$2^{-\Delta\Delta Ct}$	REST-2009©	$2^{-\Delta\Delta Ct}$	REST-2009©	$2^{-\Delta\Delta Ct}$
IRS 2-k.o., 16 weeks	1.21 ± 0.75–1.77	1.23 ± 0.17	0.74 ± 0.45–1.33	0.77 ± 0.14	1.12 ± 0.60–2.31	1.11 ± 0.16
Ob/ob, 16 weeks	**0.57*** ± 0.30–0.82	0.64 ± 0.12	**0.47*** ± 0.32–0.74	**0.50#** ± 0.10	0.84 ± 0.47–1.63	0.87 ±0.13
Rad-k.o., 16 weeks	1.22 ± 0.76–1.90	1.26 ± 0.14	**0.69*** ± 0.49–1.03	**0.70#** ± 0.05	1.38 ± 0.82–2.52	1.43 ± 0.11
IRS 2-k.o., 28 weeks	0.88 ± 0.66–1.20	0.86 ±0.08	0.63 ± 0.20–1.20	0.72 ± 0.16	0.98 ± 0.68–1.38	0.99 ± 0.12
Ob/ob, 28 weeks	**0.54*** ± 0.35–0.90	**0.66#** ± 0.15	**0.68*** ± 0.52–0.86	0.77 ± 0.08	**0.63*** ± 0.38–0.90	0.75 ± 0.16
Rad-k.o., 28 weeks	0.94 ± 0.49–1.69	1.19 ± 0.27	**0.40*** ± 0.29–0.56	**0.45#** ± 0.07	1.01 ± 0,62–1.51	1.25 ± 0.25

Table 8.10 **mRNA expression levels of 40 week old IRS 2-k.o. mice** (* = $p < 0.05$ in hypothesis test of REST-2009© software tool [S29, HPRT and GAPDH as reference genes]; # = $p < 0.05$ in Student's t-test of delta Ct values [S29 as reference gene]; values = mean ± SEM; N = 5-6 ventricles per genotype and age group).

Gene	mRNA expression	
	REST-2009©	$2^{-\Delta\Delta Ct}$
Rad	0.56 ± 0.35–0.88	0.71 ± 0.16
Gem	0.72 ± 0.62–0.82	0.92 ± 0.10
Rem 1	**0.53*** ± 0.38–0.74	0.69 ± 0.08
Ca_v1.2	0.70 ± 0.45–1.10	0.88 ± 0.18
Ca_vß1	**0.65*** ± 0.43–0.86	0.80 ± 0.15
Ca_vß2	0.59 ± 0.42–0.96	0.62 ± 0.16
Ca_vß3	**0.53*** ± 0.33–0.88	0.68 ± 0.16

8.6 Western Blot experiments

8.6.1 Positive / negative controls for Rad and $Ca_v1.2$ protein

For reliable Western Blot experiments appropriate positive and negative controls are necessary. Via a calcium phosphate based transfection method in tsa201 cells and subsequent cell lysis, it was possible to obtain clear controls for Rad and $Ca_v1.2$ antibodies. As depicted in figure 8.12, antibodies specific for Rad protein yielded in a band at approx. 38 kDa. In murine ventricle samples unspecific bands at approx. 34 kDa and 49 kDa could be detected in some samples (figure 8.12, lane 2 and 3).

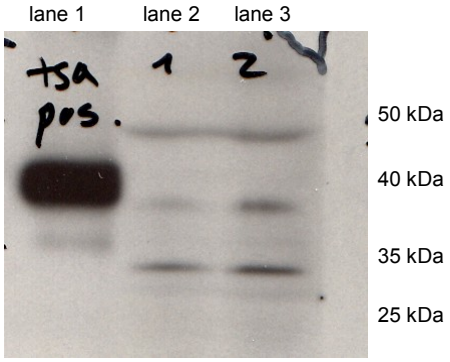

Figure 8.12 **Rad protein positive control:** Rad protein positive control yielded in a band at approx. 38 kDa (lane 1). Lane 2 and 3 show bands of murine samples: the Rad protein band appeared at approx. 38 kDa, too.

As expected, a band for Rad protein could not be detected in Rad-k.o. mice (figure 8.13, lane 3).

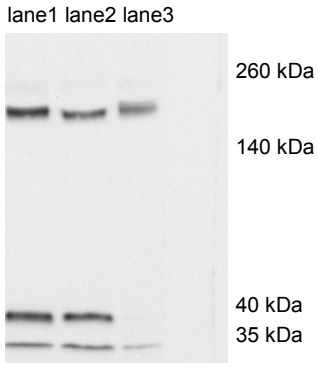

Figure 8.13 **Detection of Rad in murine ventricle samples**: in Rad-k.o. mice the antibody against Rad protein was not able to bind. No band at approx. 38 kDa could be observed (lane 3). In contrast, different wt mice samples showed a band at approx. 38 kDa (lane 1, 2). In each lane equal amounts of template were loaded. The upper bands illustrate the $Ca_v1.2$ protein expression.

A specific positive control for $Ca_v1.2$ protein could also be produced and showed a band at approx. 260 kDa, as outlined in figure 8.14.

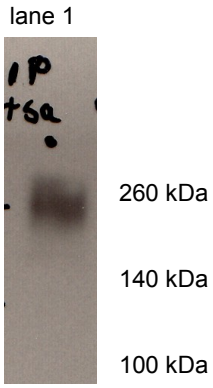

Figure 8.14 **$Ca_v1.2$ protein positive control:** $Ca_v1.2$ protein positive control yielded in a band at approx. 260 kDa (lane 1).

8.6.2 Quality of Bradford analysis

Bradford analysis was conducted to ensure that equal protein amounts could be loaded into the pockets of SDS-PAGE gel. Therefore it was important to have a reliable Bradford assay. To exclude any influence of the product buffer (0.25 mM sucrose solution) measurements of a dilution series of the standard protein BSA in the same buffer were compared to measurements in which BSA was solved in H_2O. Analysis of results revealed that sucrose had no influence on protein determination (figure 8.15).

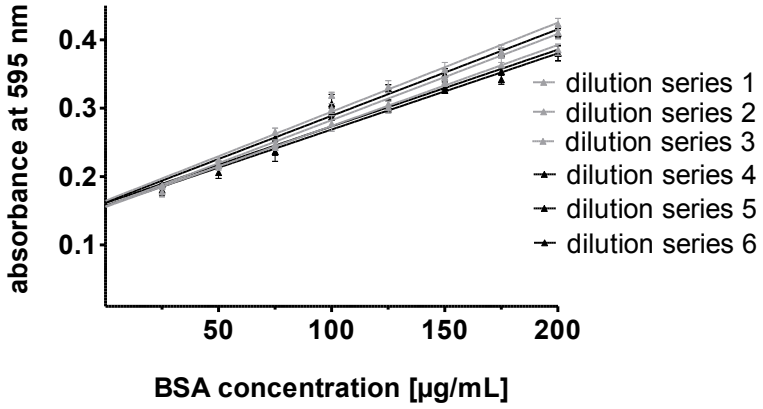

Figure 8.15 **Quality of Bradford analysis:** for Bradford analysis a dilution series of the standard protein BSA in H_2O was measured (dilution series 4, 5, 6). To ensure a correct measurement of the samples, that were solved in 0.25 mM sucrose solution, several dilution series (1-3) of BSA in 0.25 mM sucrose solution were measured, too. The measurements revealed that sucrose had no influence on protein measurement.

8.6.3 Linearity of the detection system

For relative quantification of Western Blots a linearity within the detection system has to be assumed for each gene analyzed. As outlined in figure 8.16, linearity was given for both proteins of interest, $Ca_v1.2$ and Rad. Lane 2 in figure 8.16 (A) shows optimal protein amounts, where bands are clearly visible without being saturated. Moreover, both proteins could be determined within one blot. Optimal protein concentrations proved to be between 40 and 60 µg, which corresponds to lane 1 to 3.

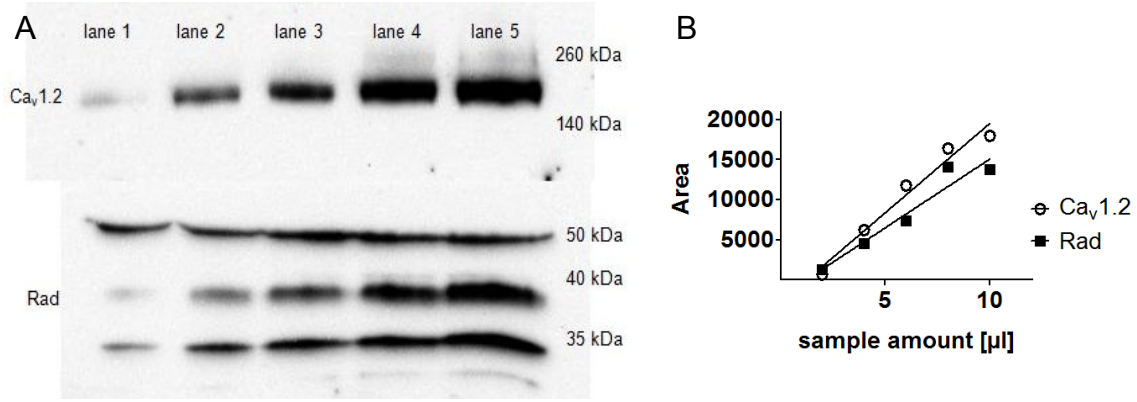

Figure 8.16 **Linearity of the detection system**. (A) Both proteins of interest, $Ca_v1.2$ and Rad, could be detected within the linearity of the detection system. Lane 2 shows optimal protein concentrations where bands are clearly visible without being saturated. Sample amount per lane (from left to right): 2, 4, 6, 8, 10 µl. (B) Band densities of the image (A) were determined via ImageJ software tool and blotted against the template amount. Linear regression revealed that linearity was given for the protein amounts used.

9 Erklärung

Hiermit versichere ich, dass die vorgelegte Arbeit persönlich, selbständig und ohne Benutzung anderer als der angegebenen Hilfsmittel und Quellen angefertigt wurde. Ferner erkläre ich, dass die vorgelegte Arbeit oder ähnliche Arbeiten nicht bereits anderweitig als Dissertation eingereicht worden sind und dass die vorgelegte Dissertation an den nachstehend aufgeführten Stellen auszugsweise veröffentlicht worden ist.

Düsseldorf, den 01.03.2017

Jessica Köth

10 Eigene Veröffentlichungen

10.1 Kongressbeiträge (Posterpräsentationen)

Die vorgelegte Dissertation ist an den nachstehend aufgeführten Stellen auszugsweise veröffentlicht worden:

KÖTH, J., FABISCH, C., HERZIG, S. & MATTHES, J.

Ventricular L-type Ca2+-channels and expression of RGK proteins in mouse models associated with diabetes.

38th Meeting of the European Working Group on Cardiac Cellular Electrophysiology (2014), Maastricht, Niederlande

KÖTH, J., FABISCH, C., HERZIG, S. & MATTHES, J.

Ventricular L-type Ca2+channels and expression of RGK proteins in mouse models associated with diabetes. *Naunyn-Schmiedeberg´s Arch Pharmacol, Springer (2015) , 388 (Suppl 1)**;** S18: 069*

81. Jahrestagung der Deutschen Gesellschaft für Experimentelle und Klinische Pharmakologie und Toxikologie e. V. (2015), Kiel

KÖTH, J., FABISCH, C., HERZIG, S. & MATTHES, J.

Ventricular L-type Ca2+-channels and expression of RGK proteins in mouse models associated with diabetes.

European Calcium Channel Conference (2015), Alpbach, Österreich

KÖTH, J., FABISCH, C., HERZIG, S. & MATTHES, J.

Ventricular L-type Ca2+-channels and expression of RGK proteins in mouse models associated with diabetes. *Biophys. J. (2015), 108 (2); 578a*

Biophysical Society 59th Annual Meeting (2015), Baltimore, Maryland, USA

10.2 Publikationen (ohne Bezug zu der vorgelegten Dissertation)

KADARI, A., MEKALA, S., WAGNER, N., MALAN, D., **KÖTH, J.**, DOLL, K., STAPPERT, L., ECKERT, D., PEITZ, M., MATTHES, J., SASSE, P., HERZIG, S., BRUSTLE, O., ERGUN, S. & EDENHOFER, F.
Robust Generation of Cardiomyocytes from Human iPS Cells Requires Precise Modulation of BMP and WNT Signaling. *Stem Cell Rev (2015), 11, 560-9*

KELLER, K., MAASS, M., DIZAYEE, S., LEISS, V., ANNALA, S., **KÖTH, J.**, SEEMANN, W. K., MULLER-EHMSEN, J., MOHR, K., NURNBERG, B., ENGELHARDT, S., HERZIG, S., BIRNBAUMER, L. & MATTHES, J.
Lack of Galphai2 leads to dilative cardiomyopathy and increased mortality in beta1-adrenoceptor overexpressing mice. *Cardiovasc Res. (2015), 108(3):348-56*

11 Danksagung

Meine Dissertation hätte nicht ohne die Hilfe, den motivierenden Zuspruch und Anregungen zahlreicher Freunde, Kollegen und meiner Betreuer entstehen können. Ich bin mir der Unterstützung sehr bewusst und möchte an dieser Stelle meinen tiefen Dank zum Ausdruck bringen.

An erster Stelle bedanke ich mich bei Herrn Priv.-Doz. Dr. Jan Matthes für die Bereitstellung des Promotionsthemas und die intensive Betreuung. Sein breites Wissen und die vielen fachlichen Diskussionen habe ich stets als persönliche Bereicherung empfunden. Insbesondere seine allzeit freundschaftliche Unterstützung und motivierenden Worte haben maßgeblich zum Gelingen dieser Arbeit beigetragen. Vielen Dank dafür!

Mein besonderer Dank gilt auch Herrn Prof. Dr. Klaus Mohr am Pharmazeutischen Institut der Abteilung Pharmakologie und Toxikologie der Universität Bonn für die Annahme der externen Betreuung meiner Doktorarbeit.

Ganz herzlich möchte ich darüber hinaus Herrn Prof. Dr. Stefan Herzig für die Anstellung am Zentrum für Pharmakologie und die wissenschaftliche Unterstützung über die letzten Jahre danken.

Ebenfalls möchte ich mich bei allen ehemaligen Kollegen des Zentrums für Pharmakologie, vor allem aber bei der AG Matthes, für die gute Zusammenarbeit und die schöne Arbeitsatmosphäre bedanken. Besonders mit Dr. Wiebke Seemann, Katarina Hauser, Sigrid Kirchmann-Hecht, Suvi Eymann und Marion Brill verbindet mich eine tolle Zeit mit vielen lustigen Stunden, auch im Privaten. Ohne ihre Unterstützung, Aufmunterung und Freundschaft wäre diese Arbeit nicht möglich gewesen. Vor allem möchte ich Wiebke und Sigrid für ihre Hilfe im Labor danken. Ebenfalls gilt den Mitarbeitern der Tierhaltung des Zentrums für Pharmakologie mein Dank für die stets professionelle Betreuung unserer Zucht- und Haltungstiere und die gute Zusammenarbeit.

Ich danke dem gesamten Team des PJ-STArT-Blocks dafür, dass mir die Lehre als sehr angenehme, unvergessliche und vor allem wertvolle Erfahrung in Erinnerung bleiben wird.

Darüber hinaus gilt mein Dank meinen Freunden - Sabrina Heinz, Hanna Alef, Samam Moradi, Bettina Gräwe, Anja Zaiss - für den starken emotionalen Rückhalt und den privaten Ausgleich. Danke, dass Ihr während dieser Zeit für mich da gewesen seid.

Abschließend möchte ich mich bei meinen Eltern und bei meinem Freund Alexander Krauskopf bedanken, die mich immer bedingungslos unterstützt und motiviert haben. Meinen Eltern danke ich darüber hinaus, dass ich durch ihre Erziehung und Liebe zu der Person werden konnte, die mich heute ausmacht. Alex danke ich vor allem für die Geduld, die mir oft gefehlt hat. Danke, dass du immer für mich da gewesen bist und an mich geglaubt hast.